

Stefan Weßling

**THE INVESTIGATION OF UNDERGROUND
COAL FIRES**

-

**TOWARDS A NUMERICAL APPROACH FOR
THERMALLY, HYDRAULICALLY, AND
CHEMICALLY COUPLED PROCESSES**

2007

Geophysik

**THE INVESTIGATION OF UNDERGROUND
COAL FIRES**

-

**TOWARDS A NUMERICAL APPROACH FOR
THERMALLY, HYDRAULICALLY, AND
CHEMICALLY COUPLED PROCESSES**

Inaugural Dissertation

zur Erlangung des Doktorgrades

der Naturwissenschaften im Fachbereich Physik

der Mathematisch-Naturwissenschaftlichen Fakultät

der Westfälischen Wilhelms-Universität

vorgelegt von

Stefan Weßling

aus Thuine

-2007-

Dekan:	Prof. Dr. J. Wessels
Erster Gutachter:	Prof. Dr. U. Hansen
Zweiter Gutachter:	Prof. Dr. H.-J. Kümpel

Tag der mündlichen Prüfung:	13. Juni 2007
Tag der Promotion:	13. Juli 2007

To my wife and my children: Anna, Jonas and Julia

Kurzfassung

DIE UNTERSUCHUNG VON UNTERTAGE-KOHLEBRÄNDEN

-

DURCH EINEN NUMERISCHEN ANSATZ FÜR THERMISCH, HYDRAULISCH UND CHEMISCH GEGEDELTE PROZESSE

von

Stefan Weßling

Die Erhaltung natürlicher Rohstoffvorkommen sowie der Schutz der Umwelt gewinnen zunehmend an Bedeutung. Unter anderem verursachen unkontrollierte Brände von Kohleflözen eine Zerstörung von Rohstoffen und eine Verschmutzung der Umwelt durch den Ausstoß treibhaus-relevanter Gase. Derartige Kohlebrände existieren weltweit. Ihre Bekämpfung ist von internationalem Interesse, um Energiereserven und die Umwelt zu schützen.

Ziel dieser Studie ist es, ein besseres Verständnis über die Brandausbreitung von untertage befindlichen Kohleflözen zu erhalten. Von besonderem Interesse ist dabei deren dynamisches Verhalten unter Berücksichtigung gekoppelter physiko-chemischer Prozesse im Flöz und im Umgebungsgestein. Ein derartiges Verständnis fördert die Entwicklung von verbesserten Lös- und Vorbeugemaßnahmen.

Zur Untersuchung des dynamischen Verhaltens von Untertage-Kohlebränden wurde ein numerischer Ansatz verwendet. Das numerische Modell berücksichtigt thermische, chemische und hydraulische Prozesse, die sowohl im Flöz als auch im diskontinuierlichen Umgebungsgestein ablaufen. Von besonderer Bedeutung ist dabei die Kopplung zwischen dem Transport brand-relevanter chemischer Stoffe wie Sauerstoff und dem Verbrennungsprozess im Flöz. Die mathematische Formulierung der beteiligten Prozesse beruht auf einem Ein-Kontinuums-Ansatz.

Zur Simulation der Kohlebrände wurde der Finite-Elemente basierte Simulator 'Rock-flow' durch ein Operator-Splitting Verfahren erweitert. Das Operator-Splitting Verfahren wurde verwendet, um den Transport und den Verbrauch von Sauerstoff getrennt voneinander zu berechnen, da beide auf unterschiedlichen Zeitskalen stattfinden. Die Trennung ermöglicht, die Brandausbreitung in Abhängigkeit von der Rate des Sauerstofftransportes zu berechnen. Die Rate des Sauerstoffverbrauches hingegen, die bei hohen Temperaturen extrem hoch wird, bleibt unberücksichtigt. Diese Prozedur ermöglicht die Simulation von Kohlebränden in akzeptablen Rechenzeiten.

Unter Verwendung eines vereinfachten zwei-dimensionalen Modells wurde eine Sensitivitätsstudie durchgeführt, um den Einfluss von Permeabilität und effektiver Wärmeleitfähigkeit auf die Brandentwicklung zu untersuchen. Für Permeabilitäten zwischen $5 \times 10^{-10} m^2$ und $1 \times 10^{-8} m^2$ ergab die Studie eine Brandausbreitungsrate zwischen drei und 340 Metern pro Jahr. In Abhängigkeit von der temperaturabhängigen effektiven Wärmeleitfähigkeit variiert die maximale Brandtemperatur zwischen 900 K und 1300 K.

Weiterhin wurde das numerische Verfahren zur Untersuchung des Einflusses von atmosphärischen Druckschwankungen und Windeinflüssen auf das Zirkulationssystem in Kohlebrandsystemen verwendet. Die Simulation von Druckschwankungen wurde durch zeitlich variierende Druck-Randbedingungen realisiert. Windeinflüsse wurden durch die Eingabe erhöhter Druckwerte an einem im Modell enthaltenen Ausbiss berücksichtigt. Anhand der Modellrechnungen lässt sich sagen, dass die Sauerstoff-Konzentration selbst unter Verwendung eines homogenen Ein-Kontinuum Modells auf externe Druckschwankungen reagiert. Eine eindeutige Antwortfunktion konnte nicht gefunden werden, da sich die Reaktion an unterschiedlichen Lokationen verschieden verhält. Die Simulation von Wind zeigt einen Einfluss auf die Sauerstoffverteilung im System.

Ein Vergleich zwischen *in-situ* Messungen und Simulationsergebnissen wurde zwecks Modellvalidierung und -kalibrierung verwendet. Der Vergleich hat ergeben, dass das verwendete Modell als validiert angesehen werden kann, da es die Größenordnung von *in-situ* beobachteten Größen reproduziert. Eine Modellkalibrierung konnte nicht durchgeführt werden, was auf den Unterschied zwischen dem Ein-Kontinuums-Modell und dem hochgradig diskontinuierlichen Umgebungsgestein realer Untertage-Kohlebrände beruht. In der Realität treten im Hangenden über Kohlebränden insbesondere großskalige Klüfte auf. Diese Klüfte wurden im Modell nicht berücksichtigt, obwohl sie einen effektiven Migrationsweg für die Sauerstoffzufuhr darstellen.

Eine praktische Anwendung des numerischen Verfahrens wurde anhand der Simulation zweier Löschszenarien demonstriert. Die Löschszenarien beinhalten die Abdeckung der Erdoberfläche mit wenig durchlässigem Material sowie die Injektion von Wasser in die Brandzentren. Bei Abdeckung zeigt sich eine Verlangsamung der Brandausbreitung sowie eine Verringerung der Brandtemperatur. Die durch die Abdeckung erzielten Effekte hängen dabei von der Größe der abgedeckten Fläche ab. Eine zu geringe Abdeckung ist nicht ausreichend für eine Brandminderung. Die Simulation der Wasserinjektion verdeutlicht die Effizienz der Energieextraktion des Brandes. Es konnte gezeigt werden, dass die Injektion in gebirgsmechanisch gestörte Bereiche nicht ausreicht, um die Wärme auch weniger gestörten und daher undurchlässigeren Bereichen zu entziehen. Daher wird die Injektion von Wasser in ungestörte Bereiche empfohlen, um dem gesamten System die thermische Energie effizient zu entziehen.

Zusammenfassend kann festgestellt werden, dass der vorgestellte numerische Ansatz eine nützliche Methode ist, um prinzipielle Untersuchungen des dynamischen Verhaltens von Untertage-Kohlebränden durchzuführen. Zudem belegt die Simulation von Löschszenarien die Verwendbarkeit des numerischen Modells zur Planung von Lösch- und Präventionsmaßnahmen.

Abstract

THE INVESTIGATION OF UNDERGROUND COAL FIRES

-

TOWARDS A NUMERICAL APPROACH FOR THERMALLY, HYDRAULICALLY, AND CHEMICALLY COUPLED PROCESSES

by

Stefan Wessling

The protection of natural resources and of the environment is becoming increasingly important. Among others, the uncontrolled burning of natural coal seams is one phenomenon which destroys enormous amounts of fuel and pollutes the air with green house gases. Such coal fires are recognized all over the world. Fighting coal fires is of international concern to protect today's natural energy resources and the environment.

This thesis aims to improve the understanding of fires propagating through a coal seam in the subsurface, termed underground coal fires. Especially, their dynamic behavior with respect to coupled physico-chemical processes in the seam and in the surrounding rocks is approached. The understanding will help to develop improved extinction and prevention strategies.

A numerical approach has been used to investigate the dynamic behavior of underground coal fires. The adopted numerical model involves thermal, chemical and hydraulic processes which take place in the coal seam and in the discontinuous rocks surrounding the coal fire. Particularly, the transport of combustion-relevant chemical species like oxygen coupled to the combustion process in the seam is an important attribute that is considered by the model. The mathematical formulation of involved processes is based on a single-continuum approach.

For the simulation of underground coal fires, the finite-element simulator 'Rockflow' has been extended by an operator-splitting approach. The approach is used to separate the calculation of oxygen transport and oxygen consumption, respectively, because transport and consumption take place at different time scales. This separation allows the propagation of the fire to be controlled by the oxygen transport rate, thereby leaving the oxygen consumption rate unconsidered. This disregard of the oxygen consumption rate, which becomes inherently high at high temperatures, allows a coal fire simulation in acceptable calculation times.

Using a simplified two-dimensional model setup, a sensitivity study has been performed

to investigate the influence of the permeability and the effective thermal conductivity on the fire development. The study yields a fire propagation rate between three and 340 meters per year for a permeability range between $5 \times 10^{-10} m^2$ and $1 \times 10^{-8} m^2$. The maximum combustion temperature varies between $900 K$ and $1300 K$, depending on the temperature dependent effective thermal conductivity.

The numerical approach has also been used to investigate the influence of atmospheric pressure variations and of winds on the circulation system around an underground coal fire. The simulation of pressure variations has been realized by temporally varying the pressure at the boundary of the model. Winds were introduced as increased pressure values at an outcrop that is part of the model. It has been found that the oxygen concentration responds to the external pressure variations, even for the homogeneous, single-continuum model. A response function could not be defined, because the response was different at different locations within the system. Winds proved to influence the oxygen distribution.

A comparison between *in-situ* measurements and simulation results has been used to perform model validation and calibration. Based on the comparison, the model could be said validated, because it reproduced the order of magnitude of *in-situ* observed values. Model calibration could not be performed, which is explained by the difference between the applied single-continuum approach and the highly discontinuous nature of rocks around real underground coal fire sites. In real fire sites, especially large-scale fractures develop due to rock-mechanical failure. These fractures have not been considered by the model, although they represent effective migration path ways for oxygen penetration.

The practical application of the numerical approach has been demonstrated by the simulation of two extinction scenarios. The scenarios consider the coverage of the surface with nearly impermeable material and the injection of water into the combustion centers. Surface coverage proved to reduce the fire propagation and to decrease the combustion temperature. Thereby, the mitigation effects depend on the size of the covered surface area. A coverage of too small areas proved to be insufficient for an efficient fire mitigation. The simulation of water injection gave insight into the efficiency of energy extraction from the coal fire. It has been shown that the injection into mechanically disturbed regions does not remove thermal energy from heated, but less disturbed and therefore less permeable locations. Because of this, the injection of water into undisturbed regions in front of combustion centers is proposed, in order to efficiently remove the thermal energy from the whole system.

Summarizing, the presented numerical approach is shown to be a useful method to perform principle investigations on the dynamic behavior of underground coal fires. In addition, the simulation of extinction scenarios confirms that a numerical approach is useful to support the planning of extinction and prevention activities.

Contents

Kurzfassung	i
Abstract	iii
Contents	v
1 Introduction	1
1.1 Coal Fires - a Global Problem	1
1.2 Investigations of Coal Fires: Research Status	2
1.3 Research Objectives	5
1.4 Thesis Outline	8
2 Mathematical Formulation of the Underground Coal Fire Model	9
2.1 Approaches to Describe Processes in Discontinuous Media	10
2.1.1 Single- and Multi-Continua Approaches	11
2.1.2 Hybrid Approach	13
2.1.3 Lattice Boltzmann Simulation	13
2.1.4 Particle-Tracking Approaches	15
2.2 Physico-Chemical Process Formulation	15
2.2.1 Formulation of the Chemical Reaction Describing Coal Combustion	17
2.2.2 Formulation of Conservation Equations	20
2.2.3 Formulation for the Macroscopic Drop of Oxygen Concentration in the Combustion Front	29
2.2.4 Initial and Boundary Conditions	31
2.3 Estimation of Time Scales	32
2.3.1 Time Scales for Reaction Kinetics	32
2.3.2 Time Scales for Oxygen Transport	33
2.3.3 Conclusion from Scale Estimates	33
3 Numerical Realization of the Simulation	35
3.1 The Finite-Element Simulator Rockflow	35
3.2 Algorithms for Reactive Transport Simulation	37
3.2.1 Application of Operator-Splitting	37
3.2.2 Extrapolation to Large Time Steps	41
3.2.3 Remarks to the Numerical Approach	44
3.3 Numerical Solution of the Forchheimer Equation	44
3.4 Code Verification	45
3.4.1 Verification of the Forchheimer Equation	46

3.4.2	Consumption/Production of Chemical Species an Heat	47
3.4.3	Solution of the Hydraulic Equation	48
3.5	Simulation Example	51
3.5.1	Setup	51
3.5.2	Simulation Results	54
3.5.3	Definition of the Propagation Rate	59
4	Sensitivity Studies	63
4.1	Permeability Variations	63
4.2	Thermal Conductivity Variations	64
4.2.1	Influence on the Ignition of Coal Seams	65
4.2.2	Influence on Burning Coal Seams	66
4.3	Variations of the Representative Length	68
4.4	Summary	69
4.5	Orders of Magnitude of Simulation Results	70
5	System Response Investigations	73
5.1	The Influence of Atmospheric Pressure Variations	74
5.1.1	Extensions of the Model	76
5.1.2	Boundary Conditions	77
5.1.3	Simulation	78
5.2	Influence of Winds	84
5.3	Conclusions Drawn from System Response Investigations	85
6	Validation and Calibration Through <i>In-situ</i> Measurements	87
6.1	Description of the Test Site	87
6.2	<i>In-situ</i> Measurements	92
6.2.1	Ventilation Measurements	92
6.2.2	Pressure Measurements	93
6.2.3	Temperature Measurements	95
6.2.4	Gas Compositional Measurements	98
6.3	Validation and Calibration	101
6.3.1	Simulation Results Compared to <i>In-situ</i> Observations	101
6.3.2	Discussion on Calibration Possibilities and Limitations	106
6.3.3	Possible Innovative Approaches for Coal Fire Exploration	107
7	Simulation of Extinction Scenarios	109
7.1	Simulations of Surface Coverage	109
7.2	Injection Simulation	110
7.2.1	<i>In-Situ</i> Injection Activities	111
7.2.2	Model and Setup	112
7.2.3	Simulation Results	114
7.2.4	Evolution of Temperature After Injection	115
7.2.5	Improvements of the Setup	116

7.3 Lessons Learned for Efficient and Sustainable Extinction Strategies	117
8 Summary, Conclusions and Outlook	119
Bibliography	123
Contents Appendix	137
A Estimations of Flow Magnitudes and the Relevance of Nonlinear Effects	138
B Experimental Determination of Reaction Kinetic Parameters from Self-Heating Experiments	143
C Pressure Considerations for Thermally Driven Systems	145
Symbols	147
List of Figures	151
List of Tables	154

1 Introduction

1.1 Coal Fires - a Global Problem

Uncontrolled burning or smoldering of coal seams, coal waste or storage piles are recognized to cause environmental and economical problems of global extent. In addition, such kind of coal fires represent one of the most challenging hazards for worldwide coal industries.

Minor problems with coal fires are reported from the Czech Republic (Klika et al., 2004) or from Germany, where the burning or smoldering of storage or waste piles has been observed (Mrasek, 2005). Problems with large-scale coal fires are reported from countries all over the world (Glover, 1998; Stracher and Taylor, 2004), the largest ones occurring in China (Cassells and van Genderen, 1995; Bethge, 1999; Rosema et al., 2001; Bökemeier and Elleringmann, 2002; Sauer, 2002), the USA (Geissinger, 1990; Nolter and Vice, 2004), India (Michalski, 2004), Indonesia (Whitehouse and Mulyana, 2004), and South Africa (Bell et al., 2001).

Fires in natural coal seams can develop where accumulations of small coal particles have been produced at the mining front and thereafter have been left unprotected in abandoned mines. Whenever such accumulations are in contact with the atmosphere, the organic coal components chemically react with the oxygen in the air. The reaction takes place at temperatures as low as the ambient temperature and produces heat due to its exothermic nature. If the heat cannot escape, the reaction undergoes a self-accelerating process, termed self-ignition, until coal combustion starts. Besides coal accumulations in abandoned mines, coal waste or storage piles are also composed of small coal grains, which may self-ignite after a sufficiently long storage time (see e.g. Schmal, 1987).

Coal seam fires destroy enormous amounts of fuel resources. For instance, the annual loss of coal due to uncontrolled coal fires is estimated to be 10 to 200 million tons in China (Zhang et al., 2004). For the Rujigou Coal Basin (Ninxia Hui Autonomous Region, PR China), Rosema et al. (2001) report an annual loss in the order of 300 000 tons, equivalent to an estimated value of 15 million US dollars. Coal is the most important energy resource in China, which is the second largest coal producer and consumer of the world (Milch, 2001). The extinction and circumvention of coal fires is therefore of essential interest for China.

The combustion of coal produces green house relevant gases like CO_2 and CO . The CO_2 emission due to Chinese coal fires has been estimated to be high as 2% of the world's CO_2 emission (Sauer, 2002; Zhang et al., 2004). Thus, coal fires contribute significantly to the global warming and certainly present a global problem. In addition, large amounts of potentially toxic trace elements are released by coal fires such as arsenic, selenium, mercury, lead and fluorine (Finkelmann, 2004).

Moreover, mining activities and humans are endangered by underground coal fires when the uncontrolled extraction of coal due to the combustion within the seams causes collapse and subsidence (Buhrow et al., 2004a; Nolter and Vice, 2004). This can cost the lives of mine workers and civil population in residential areas (Prakash et al., 2001; Stracher and Taylor, 2004). In Centralia (Pennsylvania, U.S.), an underground coal fire burning since 1962 attracted strong public attention (Glover, 1998). A whole city was evacuated and removed between 1980 and 1998, because the slowly progressing coal fire underneath the city endangered houses and infrastructure. Even today, the fire still leads to the collapse of formerly inhabited ground.

Fighting coal fires is an international concern to protect today's natural energy resources and save the environment and mining activities. This involves a better understanding of dynamic processes taking place in underground coal fires through direct observations and numerical simulation. The obtained results will help to develop efficient and sustainable extinction strategies.

1.2 Investigations of Coal Fires: Research Status

Besides of the uncontrolled burning of coal seams, the combustion of coal is applied for power generation worldwide. Many efforts have been undertaken to understand dynamic processes involved in coal combustion, which are of physical and chemical nature. In particular, the coupling between these processes is a matter of scientific concern. An overview over mechanisms and physico-chemical processes involved is given by Zelkowski (1986), Annamalai and Ryan (1993) and Annamalai and Ryan (1994).

Among others, physical processes are the convective and diffusive transportation of chemical species contained in compressible gas and the convective, radiative and conductive transportation of heat, which is produced due to the exothermal reactions. One relevant mechanism for convection by gas flow is thermal buoyancy, which results from temperature-dependent density variations of the gaseous phases.

Chemical reactions can be described as being a conversion of reactive educts to solid and gaseous products, with oxygen and coal as indispensable educt species (Hobbs et al., 1993). The chemical reactions result from complex mechanisms, hence formulations of chemical reactions have been proposed with different complexity (see e.g. Blasi, 1993, for a classification). Shadman and Cavendish (1980) experimentally investigated the applicability of different formulations for chemical reactions between oxygen and coal particles of different size. In their study, considered reactions include 1) the conversion of coal and gaseous species to gaseous fuel, 2) the conversion of gaseous fuel and oxygen to final products, and 3) the conversion of coal and oxygen to final products. Shadman and Cavendish (1980) came to the conclusion that the combustion of large particles is dominated by gasification and gas-phase reactions 1) and 2), whereas small particles are dominated by a surface reaction mechanism represented by reaction 3).

A further issue for coal combustion research is the rate at which the chemical reactions, known as reaction kinetics, take place. At temperatures between 973K and 1173K , Bews et al. (2001) experimentally determined the reaction rates between oxygen and non-porous

graphite particles in a bed of silica sand fluidized by different mixtures of oxygen and nitrogen.

At lower temperatures, the interplay between the reaction rates and energy and oxygen transport becomes relevant for the onset of self-ignition of coal. Experimental (Schmidt and Elder, 1940; Nordon et al., 1979; Ghosh, 1986; Krishnaswamy et al., 1996b; Jones et al., 1998) and theoretical (Brooks and Glasser, 1986; Brooks et al., 1988a,b; Bradshaw et al., 1991; Krishnaswamy et al., 1996a; Hull and Agarwal, 1998) studies have been performed on the self-ignition procedure, especially to protect intact coal seams and coal storage and waste piles.

Numerically, the phenomenon of self-ignition has been studied by various scientists, including Schmal et al. (1985), Schmal (1987), and Fierro et al. (2001) for the investigation of parameters like porosity affecting the self-ignition tendency of coal stockpiles. Krishnaswamy et al. (1996c) and Rosema et al. (2001) considered external influences like wind-driven forces and cyclic solar irradiation onto the self-ignition tendency of coal. Gong et al. (1999), Krause and Schmidt (2001) and Lohrer et al. (2005) performed numerical studies about the effect of humidity, liquid water and water vapor onto the self-ignition behavior. Numerically and experimentally, the influence of different oxygen volume fractions onto the self-ignition behavior was investigated by Schmidt et al. (2003), who showed that even small oxygen volume fractions suffice for self-ignition to occur.

Numerical modeling has also been improved by the energy production industry, aiming to enhance the energy extraction from coal combustion (Blasi, 1993). Challenges of simulating reactive transport phenomena with emphasis on combustion modeling are described by Oran and Boris (2001). They give a comprehensive overview over successfully applied numerical methods. According to Oran and Boris (2001), the coupling between various physical and chemical processes makes the simulation a demanding challenge, because the processes involved in combustion usually take place on different scales in space and time. One promising numerical approach is timestep-splitting, where the changes of physical variables are independently evaluated due to the different processes. The obtained solutions are then combined to obtain the composite change within one global time step. The ability of using specific numerical solvers for calculating each single process makes timestep-splitting an attractive approach, although coupling representations over different scales remains a generic but practical problem.

More specific simulation examples on coal combustion are given by Westbrook and Dryer (1981), Hjertager (1986) and Krause and Schmidt (2001). Westbrook and Dryer (1981) numerically solved one-dimensional finite difference equations for chemical kinetic mechanisms, conservation of mass, momentum, energy and chemical species. Their model, including 21 elementary chemical reactions, was used to investigate laminar flame speed. Hjertager (1986) performed numerical simulations to investigate laminar and turbulent reactive flow considering one homogeneous single phase fluid. Krause and Schmidt (2001) simulated smouldering fires based on a mathematical model including combined phenomena of heat, mass and chemical species transfer by diffusion.

Whereas formulations for all of these studies are sufficient for single phase simulations, underground coal fires need a formulation for transport processes in discontinuous porous and/or fractured rocks. Hence, a macroscopic process description is preferential, where in-

investigated variables are regarded as averages over representative elementary volumes. Such kind of macroscopization is particularly required if an extended region is considered, since the resolution of porous or fractured structures is too extensive for practicable numerical simulations.

Such a macroscopic formulation has been used by Brenner et al. (2000) to optimize the combustion in porous burners for industrial applications. Brenner et al. (2000) performed two-dimensional numerical simulations and experiments to evaluate the performance of a numerical model including macroscopic formulations of involved processes. The model considers conservation equations for 20 chemical species, which contribute to 164 chemical reactions. Additionally, two momentum equations and one energy equation are numerically solved.

A micro-scale example for combustion is given by Filippova and Hänel (1998), who present a numerical model for low Mach number combustion in a porous burner. For the simulation, a Lattice Boltzmann approach in combination with conventional convective-diffusion solvers for equations of temperature and chemical species have been applied.

In comparison to underground coal fires, studies from above were either performed to investigate small domains, like porous burners, or based on the assumption of one single fluid phase without consideration of transport processes in discontinuous fractured and/or porous media. The simulation of underground coal fires received little attention. Particularly, a complex physico-chemical model assumption has not been considered. First studies aiming to understand physical and chemical processes involved in underground coal fires are reported by Huang et al. (2001), Buhrow et al. (2004a) and Klika et al. (2004).

Numerically, gas flow and temperature fields as a consequence of underground coal fires have been investigated by Huang et al. (2001). For that purpose, a schematic geometric model has been used containing zones of different permeability to represent mechanically disturbed overlying beds. These beds have additionally been intersected with thin zones of even higher permeability, representing large-scale fractures. The simulations were performed under the assumption of steady-state Darcy flow in two dimensions, ignorable radiant heat transport, and thermal buoyancy as a consequence of temperature-dependent density variations. For the high permeability zones, values up to $10^{-9} m^2$ have been used, which is an equivalent value for coarse grained sandstone (Nield and Bejan, 1999). Huang et al. (2001) concluded that permeabilities as high as $10^{-9} m^2$ are necessary to sustain a natural convection flow which can circulate air to the coal fire. Furthermore, the temperature fields of deeper fires are controlled by heat conduction while the effect of convection becomes dominant when the fire occurs at shallow depth.

Simulations from Buhrow et al. (2004a) were performed to describe and predict rock mechanical processes as a result of coal-fire induced volume reduction in the underground seam. Simulations with the rock mechanical simulator FLAC¹ showed the development of collapse structures, which are intersected with large-scale fractures.

Klika et al. (2004) used numerical simulations to investigate the temporal temperature distribution around three burning coal seams. The simulation results explained the formation of geological variegated beds. The numerical model includes a conductive transient

¹Itasca, <http://www.itasca.de>

heat equation and a heat source, which becomes active for temperatures exceeding 350°C. The source was introduced according to the findings from laboratory and numerical experiments. A comparison between simulation results and variegated beds in the Czech Republic showed that the burn out of three coal seams likely took place over about 2000 years, with temperatures between 350 °C and 800 °C within the seams.

Studies closely related to the underground coal fire problematic have been performed on underground coal gasification, where similar physical and chemical processes are involved. Gasification aims to produce fuel-rich reaction products (see e.g. Hobbs et al., 1993), which can be further used for energy production. Recently, Perkins et al. (2001) and Perkins and Sahajwalla (2005) presented a comprehensive one-dimensional mathematical model for the chemical conversion of a semi-infinite block of coal. The model includes conservation equations for mass, linear momentum, energy, gas species, and solid species, as well as reaction kinetics and structural and material changes of the coal. For simplicity, chemical reactions have been assumed for pure carbon conversion. A similar numerical study complemented by experiments on underground coal gasification is presented by Yang (2004), who used a physical model including energy, species and conservation of momentum. The model proved to be sufficient for the reproduction of the experimentally obtained temperature, concentration and pressure fields.

Summarizing, much effort has been made in recent years to simulate coal fire combustion processes. Most activities are carried out by the energy producing industry focusing on the improvement of the combustion process.

1.3 Research Objectives

Previous studies approve the combustion of coal as a complex procedure. Underground coal fires moreover depend on hydraulic, chemical, thermal and mechanical processes within the embedding geological formations. Due to this complexity, challenges still persist for the investigation of underground coal fires, both from the numerical and from the experimental perspective. In the following, some challenges will be summarized and aims will be formulated for the thesis.

For coal fires below the surface, the coupling between chemical reactions in the seam and transport processes in the surrounding bedrock is of particular importance. According to Blasi (1993), the coupling is essential to prevent coal seams against unwanted fire events. However, the complexity of the involved physico-chemical processes still hampers recent efforts to numerically investigate underground coal fires.

So far, an appropriate physico-chemical model to simulate the dynamic behavior of underground coal fires has not been found. To the author's knowledge, Huang et al. (2001) are the only ones considering gas and temperature flow in the beds around underground coal fires, but transport of chemical species and chemical reactions between coal and oxygen have not been included.

Concerning the transportation of heat and chemical species, a large range of spatial scales needs to be considered. Typically, underground coal fires are embedded in natural porous sandstone or limestone formations of low permeability (Gielisch and Kahlen, 2003), which

are however intersected with large-scale fractures resulting from subsidence (Buhrow et al., 2004a). Large-scale fractures are effective migration path ways for massive gas flow. Hence, transport processes have to be considered over different length scales within the discontinuous formations.

Another challenge is given by the large range of time scales. According to Hjertager (1986), the range of time scales in the problem of combustion modeling is a demanding task from both, computational and conceptual points of view. However, adequate modeling of the coupling between fluid dynamics and reaction kinetics is the key to successfully predict various combustion processes. During combustion, oxygen is consumed in time scales of seconds, whereas typical coal consumption in industrial power generation burners takes place within some hours (Hobbs et al., 1993). Coal fires may even last over 2000 years (Klika et al., 2004), which largely exceeds the range of time scales in industrial applications.

Numerically, one problematic issue is to resolve the time scales from reaction kinetics and oxygen transport. At high temperatures, the reaction rate is becoming very high, whereas the transportation of oxygen takes place in times from seconds to minutes. Because oxygen transport is the slower process, this process controls the overall burning rate. However, numerical models considering both, reaction kinetics and oxygen transport, need to resolve the smallest time scales (from reaction kinetics) to obtain stable solutions. This requires inherently small time steps.

Ten years ago, limited computer capabilities might have been one reason for the simulation of only simplified combustion models (Guntermann, 1988; Hobbs et al., 1993). However, also recent simulations have been performed under the steady-state assumption (Brenner et al., 2000; Huang et al., 2001), or over time scales that are short in comparison to realistic duration times of underground coal fires (Westbrook and Dryer, 1981; Hjertager, 1986; Krause and Schmidt, 2001; Perkins and Sahajwalla, 2005). Krause and Schmidt (2001) simulated combustion phenomena over a simulation time of 3600 seconds. Calculations of laminar flow by Hjertager (1986) reached a steady-state solution after 40 to 80 transient time steps. For underground coal fires, a steady-state assumption is inappropriate, because the fires permanently propagate along the seam until the fuel has been completely consumed or extinction activities show an effect.

Accordingly, an application of numerical simulations to investigate underground coal fires requires improved numerical approaches. Once obtained, simulations are a useful method for a detailed investigation of coupled processes related to underground coal fires. To obtain a better understanding of the dynamic behavior of underground coal fires by means of numerical simulation, the following aims are addressed in this thesis:

- A first aim is to find a physico-chemical model including relevant processes, which influence the dynamic development of underground coal fires. The model needs to a) consider transport processes on macroscopic scales in discontinuous media, and b) represent the coupling between the embedding rocks and the fire in the underground coal seam. For that purpose hydraulic, chemical and thermal processes will be included into the model applying a single-continuum description for porous media. Chemical mechanisms in the seam are realized by a reaction model from Schmidt

et al. (2003).

- The next aim addresses the large discrepancy between time scales for consumption and transport of oxygen. Numerical algorithms will be developed to simulate the dynamic development of underground coal fires in acceptable calculation times. This aspect is realized by extending the finite-elements simulator Rockflow (see e.g. Kolditz et al., 1998). The well-established operator-splitting approach will be used to separate between very fast reaction kinetics and rather slow oxygen transport. Doing so, the decisive time step is chosen according to criteria from transport estimations, so that the overall coal fire burning rate can be controlled by oxygen transport only. An additional extrapolation algorithm is implemented for the coal consumption rate to increase the time step. Based on the model presented, two-dimensional scenario simulations are performed. The maximum temperature and the fire propagation rate are evaluated as characteristic quantities for an underground coal fire.
- Further aim is to obtain insight into the sensitivity of the dynamic coal fire development depending on parameters of the adjacent rocks. For the sensitivity analysis, two parameters with major influence onto the dynamic behavior of underground coal fires are varied: the permeability and the effective thermal conductivity, which includes a simplified formulation for radiant heat transport. An additionally introduced macroscopic parameter, the representative length for oxygen transport into the combustion center, is also investigated.
- *In-situ* measurements will be compared with simulation results to postulate the applicability of *in-situ* data for the prediction of the dynamic fire development and for model validation and calibration. The comparison between *in-situ* observations and scenario calculations is based on experimental measurements in Fire Zone 3.2 of the Shenhua Group Coal Mining Area of Wuda (Inner Mongolia, PR China) and a simplified numerical setup of that fire zone.
- Finally, effects of fire fighting operations and natural processes like changing weather conditions onto the coal fire system are investigated. The intention of the simulations is to provide support for human activities, both for exploration and extinction of underground coal fires. Consideration of changing weather conditions is realized by time dependent pressure and temperature boundary conditions representing atmospheric variations. In addition, the presented physico-chemical model is used to simulate extinction scenarios. Two scenarios will be discussed: one surface sealing scenario and one water injection scenario.

The purpose of this thesis is to present a concept for modeling large-scale coal seam fires. In addition, perspectives will be given how to apply numerical simulations for the *in-situ* investigation of the coal fire behavior and to support extinction activities. Trying to find a detailed model for a specific test site is beyond the scope of this work.

1.4 Thesis Outline

The thesis is organized as follows: In chapter two, the mathematical formulation of physico-chemical processes taking place in underground coal fires is presented. Likewise, time scales are estimated as a motivation to implement improved numerical algorithms. Chapter three presents these algorithms to solve the physico-chemical system in reasonable calculation time. A simulation example is given for the propagation of underground coal seam fires coupled to hydraulic and thermal processes in the surrounding rock formations. A sensitivity study on the influence of hydraulic and thermal parameters to the coal fire propagation is presented in chapter four. In chapter five, the influence of external natural processes is discussed, with emphasis put on the flow behavior around the coal fire. The processes are inserted as boundary conditions into the model. They represent barometric pressure variations and winds. Chapter six presents experimental data obtained from *in-situ* measurements. Based on a comparison between these data and simulation results, possibilities and limitations for model validation and calibration are discussed. In addition, innovative *in-situ* methods to explore underground coal fires are proposed. Chapter seven presents two scenario simulations to improve fire extinction strategies. Chapter eight ends with a conclusion and an outlook.

2 Mathematical Formulation of the Underground Coal Fire Model

In an underground coal fire, phenomena as graphically represented in Fig. 2.1 do appear. The phenomena are caused by mechanical, hydraulic, thermal and chemical processes. The interaction between these processes affects the dynamic behavior of the fire.

An investigation of underground coal fires presumes to include an exchange between the combustion center and the atmosphere. Such an exchange is caused by transport processes in the bedrocks around the coal fire. Its dynamic behavior is thus controlled by processes in the seam and in adjacent rocks. The mathematical formulation of such processes should be performed for macroscopic spatial scales, to make simulation practicable.

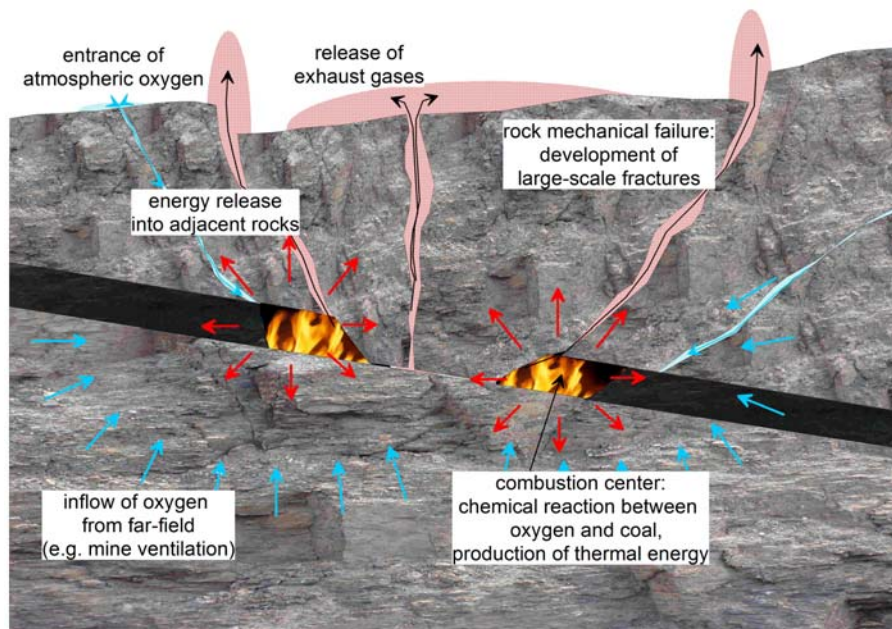


Figure 2.1 Simplified schematic illustration of phenomena appearing in underground coal fires. In the coal seam, combustion centers exist, in which a chemical reaction between oxygen and coal takes place. The reaction of exothermic nature produces thermal energy, which is released into the adjacent rocks. Likewise, produced exhaust gas is transported to the surface. The burn out of the seam leaves cavities, so that overlying beds collapse due to rock-mechanical failure. Thereby, large-scale fractures develop. These large-scale fractures may give new path ways for oxygen transport into the combustion center. In addition, supply with oxygen takes place by transport processes through adjacent rock formations.

In the following, a brief introduction into concepts for the description of processes in discontinuous porous and/or fractured media is given. Then, the assumed physico-chemical model is presented and mathematically formulated. Finally, an estimation of the times scales is performed as a motivation to develop improved numerical algorithms.

2.1 Approaches to Describe Processes in Discontinuous Media

Underground coal fires are embedded in geologic bedrocks like sandstones or limestones, which are of porous or fractured nature. Common to all these porous or fractured media is that part of the domain is occupied by a persistent solid matrix, whereas the remaining void space is occupied by a single or multiple phase fluid. The simulation of underground coal fires presumes an appropriate conceptual model to consider processes within the geologic bedrocks.

Thereby, the solid and fluid phases frequently exhibit different thermal and hydraulic properties, hence different processes may dominate in each phase. For example, convective transport processes are driven by fluid motions and thus take place in the fluid phase. In contrast, the solid matrix is the preferential medium for e.g. conductive energy transport.

Yeh (2000) proposes three levels of observation for processes in subsurface systems: the molecular level, the microscopic level, and the macroscopic level. At the molecular level, mechanical interactions between single molecules are considered. At the microscopic level, the principles of fluid or statistical mechanics are used to describe processes within the pore space (see also Blasi, 1993). At the macroscopic level an average behavior of the system is considered over a representative elementary volume (REV) of the geologic medium.

The physical structure in the microscopic level is such that the molecular structure is ignored and the materials (fluids, solids, etc.) are regarded as a continuum with smoothly varying properties. They need to be smooth to use classical mathematics for description. Similarly, the physical structure in the macroscopic approach can be considered as such that the (microscopic) pore-level behavior is ignored, yet the discontinuous medium is taken as a continuum with smoothly varying properties.

A description of transport processes at the microscopic level becomes difficult due to the lack of information on the microscopic configuration of the interphase boundaries. Moreover, it is often even difficult to adequately define the boundary conditions (Bear, 1972). Different approaches are currently used to describe processes in discontinuous fractured and/or porous media in a variety of disciplines such as oil and gas recovery, geothermal energy and groundwater modeling.

In continuum-based approaches the discontinuous domain is replaced by a macroscopic model, in which the (solid and fluid) phases are assumed to behave as a continuum that fills up the entire domain. The continuum model describes processes in terms of differential quantities, thus enabling the solution of problems by employing methods of classical mathematics.

Particle-tracking-based approaches belong to a combination of Eulerian and Lagrangian methods and are frequently used to simulate convection-dominated transport phenomena (Yeh, 2000). Recently, Lattice Boltzmann methods became attractive due to its good calcu-

lation performance. These methods are based on the Boltzmann equation, which expresses a system of interacting particles. In contrast to the above, Lattice Boltzmann methods consider transport processes in the void (pore) space at the microscopic level. In the following, these most frequently used approaches are briefly introduced.

2.1.1 Single- and Multi-Continua Approaches

Continuum-based approaches for discontinuous geologic media result from pioneering work of Muskat (1937), Bear (1972) and Dagan (1989). Macroscopic continuum approaches assume any microscopically disjoint subdomain to be replaceable by a model in which each of the (solid and fluid) phases is assumed to behave as a continuum. Within this continuum one can assign to any point kinematic and dynamic variables and parameters that are continuous functions of the spatial coordinates and of time. The variables and the parameters of the fictitious continuum, averaged over an REV, enable us to describe flow and other phenomena within a porous and/or fractured medium by means of partial differential equations.

The procedure to pass from the microscopic level to the macroscopic one takes place by averaging the microscopic balance equations for each participating phase over REV's. Thereby, the volume for averaging should be much smaller than the size of the entire domain, as otherwise the resulting average cannot represent what happens around a point P within the volume. On the other hand, it must be sufficiently larger than the size of a single pore to permit the meaningful statistical average required in the continuum concept.

Applying the continuum approach to the dynamics of fluids in porous media, macroscopic parameters like permeability and porosity are introduced to accommodate the observed phenomena. The parameters need to be quantified by laboratory and/or *in-situ* experiments.

Sometimes, spatial scales of different size may be present in heterogeneous geologic media. Hence, the physical behavior of a phase may be different at different spatial scales. One example is a fractured porous medium in which fluid flow through the fractures behaves differently than through the porous blocks surrounding the fractures.

If the range of spatial scales remains small within a discontinuous medium, the concept of a single continuum suffices for the process formulation, which can be found in various textbooks, for example in Bear and Bachmat (1990), Whitaker (1996), and Yeh (2000).

If the range of spatial scales becomes large, so that e.g. a fluid phase behaves different on different scales, the concept of interacting multi-continua is used. Here, the range of scales is divided into a number of groups. Each group is then considered as a separate continuum for which processes are described. The number of assumed continua depends on the number of groups which contain a certain range of scales. The exchange among the continua is expressed through sink or source terms in the appropriate balance equations.

Practical applications involving multi-continua models include contaminant migration, oil recovery from fractured reservoirs, geothermal energy, and groundwater modeling in karst aquifers (Bai et al., 1993; Lichtner, 2000; Sauter et al., 2006). Thereby, a distinction is frequently made for media where only the porosity (multi-porosity media), only the permeability (multi-permeability media), or where both parameters are varying (multi-porosity/multi-permeability media). E.g., Bai et al. (1993) propose a triple-porosity/triple-permeability formulation for a system containing cracks, fissures and pores.

One requirement for a proper application of such single- or multi-continua approaches is the existence of overlapping REV's. Then, the properties of each of the phases, as well as those of the apparent phases at every point are obtained as averages over the REV centered at that point (Bear and Bachmat, 1990).

A definition of REV is illustrated in Fig. 2.2, where the porosity is taken as an example for a macroscopic parameter. The graph shows the variation of matrix or fracture porosity with respect to the size V of a volume element contained in a geologic formation. For small V , the porosity may vary due to the small amount of pores contained. Within the domains of continuum, the volume element is said to be representative because the macroscopic parameter does not change with varying V . Of, course, a REV for fractured media only exists when the volume elements contains a sufficiently high amount of fractures (or fissures).

A proper reproduction of real coal fires by numerical simulations presumes to take large-scale fractures into consideration, which emerge from rock mechanical failure of the overlying bedrocks. Whenever such large-scale discontinuities exist, a REV can hardly be found, because the fractures are usually sparsely distributed. However, further research is required to statistically quantify the distribution of fractures above underground coal fires.

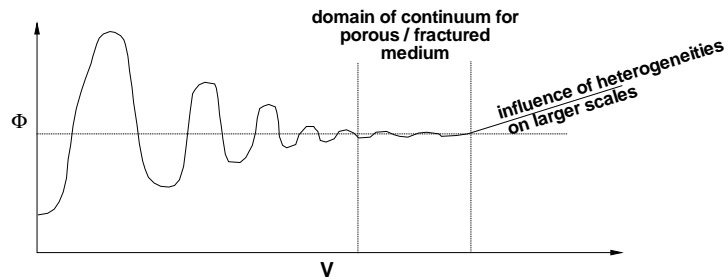


Figure 2.2 Illustration of the definition of a representative elementary volume, modified after Yeh (2000). The graphs shows the matrix porosity Φ versus the size V of a volume element contained in a geologic system. The volume element is said to be representative when the macroscopic parameter, like the porosity, does not change with the size of V . At larger scales (increasing V) heterogeneities larger than the pore space may be present, so that Φ becomes scale dependent again.

2.1.2 Hybrid Approach

As mentioned above, one prerequisite for continua-based models is the existence of REV's to obtain statistically meaningful averages of macroscopic parameters. When structures like faults or large-scale fractures are sparsely distributed in a system, such an averaging cannot be performed and macroscopic parameters become scale-dependent, as illustrated by Fig. 2.2. In such situations, the fractures or faults can be treated by a discrete fracture approach which is coupled to a continuum-based approach representing the porous medium separately (Yeh, 2000).

The discrete fracture approach treats fractures as geometrically planar structures, due to their small apertures in comparison to the fracture lengths. Because of that property models can be simplified by integrating microscopic balance equations over the aperture in order to reduce the spatial dimension by one. The consideration of discrete fractures by $(n-1)$ -dimensional elements is of essential advantage for numerical simulations. E.g., two-dimensional fractures or faults can be coupled to three-dimensional porous domains, without explicitly resolving the three-dimensional structure of fractures.

Although only fluid may be contained within large-scale structures like fractures or faults, processes are usually not described at the microscopic level (where the Navier-Stokes equations are needed to consider momentum conservation). Instead, a macroscopic process description is used for processes in fractures, in analogy to the continuum-based concept for porous media.

The coupling between the discrete fracture model and the continuum model can be realized by phase exchange relations, which can be considered as macroscopic interface constraints from the physical perspective (Kolditz, 1996). Such kind of modeling method is frequently termed hybrid modeling approach. A detailed derivation of process descriptions for the continua and discrete fractures at the macroscopic level is given by Kolditz (1996).

2.1.3 Lattice Boltzmann Simulation

Recently, Lattice Boltzmann methods have frequently been applied to simulate complex geometries (like porous or fractured media). Whereas all the above mentioned approaches include a process description at the macroscopic level the Lattice Boltzmann approach focuses on the consideration of processes somewhere between the molecular and the microscopic levels. According to Chen and Doolen (1998) the fundamental idea of Lattice Boltzmann methods is to construct simplified kinetic models that incorporate the essential physics of microscopic processes, so that the macroscopic averaged properties obey the desired macroscopic equations.

Lattice Boltzmann models are based on Boltzmann's idea of considering gas as a composition of interacting particles. A system of interacting particles is described by the Boltzmann equation which is derived from the kinetic theory of gases and statistical mechanics.

Lattice Boltzmann models simplify Boltzmann's concept by reducing the number of possible particle spatial positions and microscopic momenta from a continuum to just a handful. Similarly time is discretized into distinct steps. Particle positions are confined to the nodes

of a lattice. Variations and momenta that could have been due to a continuum of velocity directions and magnitudes and varying particle mass are reduced (in a simple 2-D model) to eight directions, three magnitudes and a single particle mass (a scheme that was proposed by Qian et al., 1992). Though strongly simplifying the description of interacting gas particles, Lattice Boltzmann models are able to reproduce the behavior of real fluids (Sukop and Thorne Jr., 2006).

Because the idea of Lattice Boltzmann methods differs from classical continuum-based considerations one common Lattice Boltzmann formulation is briefly introduced. According to Zhou (2004) the Lattice Boltzmann method consists of two steps: a streaming step (convection) and a collision step (viscous diffusion). In the streaming step, the particles move to the neighboring lattice points in their direction of the velocities, which is governed by

$$f_{\alpha}(\mathbf{x} + \mathbf{e}_{\alpha}\Delta t, t + \Delta t) = f'_{\alpha}(\mathbf{x}, t) + \frac{\Delta t}{N_{\alpha}e^2} e_{\alpha i} F_i(\mathbf{x}, t). \quad (2.1)$$

Herein $e = \frac{\Delta x}{\Delta t}$,

f_{α} is the distribution function of a particle α ,

f'_{α} is the value of f_{α} before the streaming,

Δx is the lattice size,

Δt is the time step,

F_i is the component of the force in i direction,

\mathbf{e}_{α} is the velocity vector of a particle, and

N_{α} is a constant, which is specified by the lattice pattern as

$$N_{\alpha} = \frac{1}{e^2} \sum_{\alpha} e_{\alpha i} e_{\alpha i}. \quad (2.2)$$

In the collision step, the arriving particles at the points interact one another and change their velocity directions according to scattering rules, which is expressed as

$$f'_{\alpha}(\mathbf{x}, t) = f_{\alpha}(\mathbf{x}, t) + \Omega_{\alpha}[f(\mathbf{x}, t)]. \quad (2.3)$$

Here, Ω_{α} is the collision operator, which controls the speed of change in f_{α} during collision. For Ω_{α} , the lattice BGK collision operator

$$\Omega_{\alpha} = -\frac{1}{\tau}(f_{\alpha} - f_{\alpha}^{eq}) \quad (2.4)$$

is frequently used, where

f_{α}^{eq} is a local equilibrium distribution function and

τ is the single relaxation time.

Streaming and collision are usually combined into the equation

$$f_{\alpha}(\mathbf{x} + \mathbf{e}_{\alpha}\Delta t, t + \Delta t) - f_{\alpha}(\mathbf{x}, t) = -\frac{1}{\tau}(f_{\alpha} - f_{\alpha}^{eq}) + \frac{\Delta t}{N_{\alpha}e^2}e_{\alpha i}F_i(\mathbf{x}, t), \quad (2.5)$$

which is a popular form of the Lattice Boltzmann equation (Zhou, 2004).

Since 1992 the number of papers published on the development and application of Lattice Boltzmann models exponentially grew, with a majority of papers contained in Physics and Computer Sciences (Sukop and Thorne Jr., 2006). The Lattice Boltzmann method has been used for the simulation of flow or transport phenomena on the microscopic scale in fractured and/or porous media to determine macroscopic parameters (Stockman et al., 1997; Bernsdorf et al., 2000; Zhang et al., 2000; Kang et al., 2002, 2003; Keehm et al., 2004). Besides, ongoing theoretical (He and Luo, 1997) and numerical (Zou and He, 1997; Ihle and Kroll, 2000; Kandhai et al., 2000; Guo and Zhao, 2003) improvements have been published. Sukop and Thorne Jr. (2006) present various applications of Lattice Boltzmann models for typical geoscientist's and the engineer's purposes.

2.1.4 Particle-Tracking Approaches

Particle-tracking approaches belong to Lagrangian-Eulerian methods and are especially used to simulate chemical transport phenomena. These approaches avoid numerical oscillations when advective transport phenomena dominate (Yeh, 2000).

In particle-tracking approaches, particles first are introduced in the domain, which is discretized with a fixed grid system. This is, in contrast to purely Lagrangian approaches, where physical quantities are computed at a set of points moving with the fluid (Yeh, 2000). Each particle is associated with a spatial coordinate and a discrete quantity of mass. Second, these particles are moved forward with the flow (which should represent both convection and diffusion). Third, whenever convenient, the number and location of the particles are processed back to concentrations at the fixed grid nodes as to give the instantaneous concentration field. Fourth, concentration changes at each node during the time interval resulting from chemical reactions, if involved, are computed. Finally, the mass associated with each particle is recomputed according to the new concentration field. An application example for the particle-tracking approach is given by Tsang and Doughty (2003).

An extension to the particle-tracking method is a random-walk approach, which has been introduced for a statistical consideration of diffusion phenomena (Kinzelbach, 1992). In the random-walk approach convective motions of particles are superimposed by a random motion, whose statistical properties rely on dispersive or diffusive processes. Through the simulation of many randomly orientated tracks (random walks) a dispersing cloud of tracers develops.

2.2 Physico-Chemical Process Formulation

The phenomena from Fig. 2.1 are caused by thermal, hydraulic, chemical and mechanical processes. Their interaction determines the dynamic behavior of the coal fire. Particularly

relevant processes are the transport of heat and oxygen through adjacent rocks, the consumption of oxygen and coal in the seam, as well as the resulting production of heat due to the combustion. Obviously, the coupling between chemical reactions in the seam (i.e. the consumption of oxygen and coal) and transport processes in the adjacent bedrocks is essential for underground coal fires. The transport processes are characterized by macroscopic parameters for phenomena appearing at naturally discontinuous porous and/or fractured media. Mechanical processes cause large-scale fractures resulting in migration pathways for oxygen and heat. They have thus indirect influence on the dynamic development of underground coal fires.

As a first step towards a better understanding, numerical simulation is a promising approach to investigate the dynamic development of underground coal fires. For this work a deterministic model is assumed, wherein hydraulic, chemical and thermal processes are involved. These processes and the coupling mechanisms between them are graphically represented in Fig. 2.3. The physico-chemical model assumes gas as the only involved fluid.

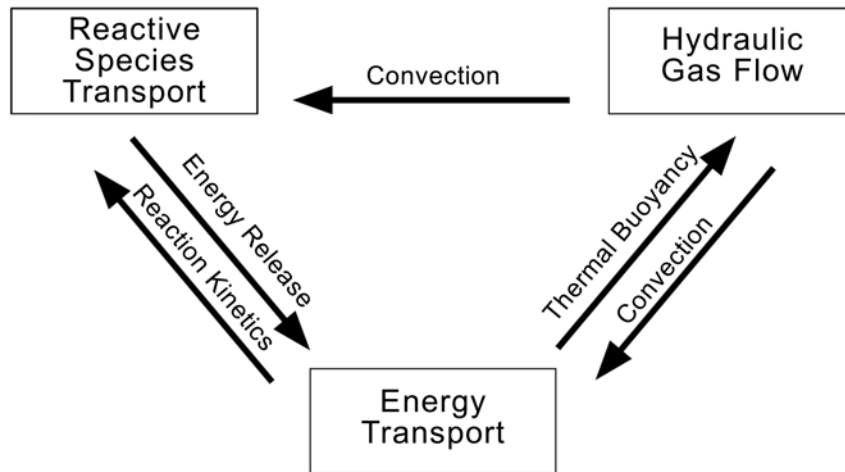


Figure 2.3 Representation of assumed physico-chemical processes and the coupling mechanisms between them

While ignition and propagation of smouldering fires through dense accumulations of dust or bulk material might be controlled by diffusive transport phenomena (Krause and Schmidt, 2001), large-scale considerations presume the incorporation of convective transport processes. E.g., free convection effects onto the combustion become significant for systems containing large coal particles (Annamalai and Ryan, 1993), which likely exist in underground coal fires. Also, Huang et al. (2001) report evidence that air convection is essential for such fires.

Hydraulic gas flow may be driven either by externally imposed pressure differences or by thermal buoyancy. Pressure differences might (but not necessarily) occur due to mine ventilation or strong winds. Thermal buoyancy is definitively involved in underground coal fires, because it results from temperature dependent density differences between gas in the

combustion center and in the environment, respectively (see e.g. Tritton, 1970, for thermal buoyancy). In this work, thermal buoyancy is the only considered driving force for hydraulic gas flow.

Reactive species transport summarizes the flow of oxygen and gaseous products and their consumption or production due to the chemical reactions within the coal seam. Energy transport includes convection, conduction and radiation of the heat produced by the chemical reactions.

For the present work, mechanical processes are not considered, although rock mechanical failure of the overlying rock may cause an abrupt change in the permeability. However, predicting the influence of mechanical mechanisms onto transport phenomena is a large uncertainty. Even though failure of the adjacent rocks might be predictive through rock-mechanical simulations (as proposed by Buhrow et al., 2004a), precise locations and structures of developing large-scale fractures can only be roughly estimated (Jing and Hudson, 2002). Accordingly, predicting the permeability of developing large-scale fractures by numerical simulations is extremely difficult if not impossible (Berkowitz, 2002).

Coupling mechanisms between hydraulic gas flow and energy transport are thermal buoyancy and convection. Reactive species transport and energy transport are coupled through energy release and reaction kinetics. The former results from the chemical reactions, which are in turn affected by oxygen transport into the combustion center. The more oxygen arrives the more energy is released, which is then removed by energy transport. The back coupling through reaction kinetics considers the temperature dependent rate of the chemical reactions. Convective oxygen and exhaust gas transport are the coupling mechanisms between reactive species transport and hydraulic gas flow.

Finally, balance equations for considered primary variables like pressure and temperature need to account for the heterogeneous nature of the system considered. Although large-scale fractures develop due to rock mechanical failure, the mathematical formulation is based on a porous-medium, single-continuum approach, as introduced in Sec. 2.1.1. *In-situ* measurements prove the large difference between flow in the matrix and in fractures, hence the additional treatment of problems arising from varying spatial scales is beyond the scope of this thesis. In the following, the applied equations and the assumed chemical mechanism within the coal seam are presented.

2.2.1 Formulation of the Chemical Reaction Describing Coal Combustion

The overall combustion mechanism between oxygen and of coal is a composition of complex heterogeneous and homogeneous chemical reactions. Homogeneous reactions are referred to as reactions between material within the same state of aggregation, like the gas phase. Those reactions take place between oxygen and degrading gas which contains combustible volatiles (Heek and Mühlen, 1984). Heterogeneous reactions take place between chemical species from different (e.g. solid and gaseous) phases.

For a proper consideration of combustion phenomena, the open nature of the reactive system needs to be taken into account. The term 'open' refers to a system in which fluidal species are transported into or out of the reactive system, besides of their participation in

the chemical reactions.

Finally, the combustion represents an irreversible mechanism, i.e. the production of solid and gaseous products from the reaction between coal and oxygen exclusively takes place in this direction. A back conversion from solid and gaseous products into the former educts does not exist. Hence, the reaction will never reach any chemical equilibrium where the mass conversion from forward and backward reactions is in balance. A system in chemical equilibrium would simplify the numerical calculation because the chemical reaction becomes time-independent in that case.

The behavior of burning or smoldering coal obtained much attention, especially for industrial purposes. Thus, efforts were made to understand this complex combustion mechanism. For industrial use, coal is frequently prepared by crushing or pulverizing the compact material, as smaller coal particles exhibit a high reactivity. Hence, reported investigations are mainly about the combustion process of small-scale particles (e.g. Bews et al., 2001).

A comprehensive overview over different mechanisms which control the gasification and carbon reaction processes of isolated coal or char particles is given in Annamalai and Ryan (1993). Mechanisms include the kinetics and diffusion controlled combustion of char, as well as the change of the inner surface resulting from, but also affecting, the combustion process. According to the authors, the interaction between single particles and the ambience is essential for understanding combustion phenomena of cumulated fuels. Those phenomena are addressed in Annamalai and Ryan (1994). They suggest to develop more exact models for the transient combustion of coal including the unsteady gas and solid phases in quiescent environment, so that the interactions between fluid dynamics and combustion chemistry can be better understood.

A classification of frequently used formulations of reaction mechanisms into three groups is proposed by Blasi (1993):

1. One-step global models, which express the degradation of the solid fuel by means of the experimentally measured rates of weight loss;
2. One-stage, multi-reaction models, used to correlate reaction product distributions. These are one-stage simplified kinetic models, made of several reactions, describing the degradation of the solid to char and several gaseous species;
3. Two-stage, semi-global models, when kinetic mechanisms of solid degradation include both primary and secondary reactions.

The first model describes the molar or mass fraction conversion of solid and gaseous educts into combustion products with one single overall chemical reaction. One-stage, multi-step reaction models are regarded as simplified kinetic models, made of several reactions. This model is appropriate to describe the degradation of solid fuel to char and several gaseous species. Models of the third type include kinetic mechanics of solid degradation, whereas the reaction products might further react with the reactants (oxygen). Thus, this model assumes primary and secondary chemical reactions, whereas the secondary reaction takes place after reactive products have been produced from the primary reactions. Numerical investigations of the combustion process have been performed with several of the above

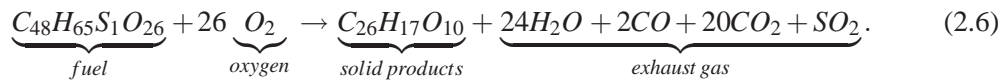
models.

Of special importance for the combustion rates is the description of reaction kinetics, i.e. the rate at which the chemical reactions take place (Zelkowsky, 1986). For that, an Arrhenius formulation is frequently used, which is derived from molecular collision theory (Näser, 1968; Lichtner, 1996). Molecular collision theory considers the fact that the kinetic energy of reactive gas molecules exponentially increases with increasing temperature. The resulting decrease in the mean free path of the molecules raises the probability of the collision between two reactive gas molecules. Thus, the amount of chemical reactions increases with time. An Arrhenius formulation expresses this effect of exponentially increasing reaction rates with increasing temperature.

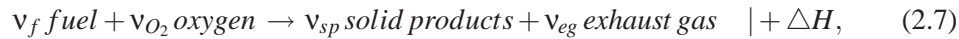
Whenever the chemical reactions take place in an open system, the overall combustion rate results from the rates of transport processes and chemical reactions, respectively (Hobbs et al., 1993). Heek and Mühlen (1984) propose different states of combustion, depending on the system temperature. At low temperatures, the reaction kinetics is the process controlling the combustion rate. At higher temperatures, transport processes decide about the speed of combustion.

Due to the complexity and partly still unknown nature of the chemical reactions during coal combustion, simplified one-step global reaction models (cf. Blasi, 1993) were used by various investigators (e.g. Schmal, 1987; Krause and Schmidt, 2001; Schmidt et al., 2003). According to Blasi (1993) such models are sufficient at least for fire safety issues. Malow and Krause (2004) experimentally investigated the oxidation reaction of lignite coal dust in order to obtain the overall kinetic constants for such simplified chemical model. Problems with one-step models might appear whenever water loss is considered beneath the chemical reaction between oxygen and coal (Ghetti et al., 1985).

For the present work, a one-step reaction formulation is used. The elemental compositions of the solid fuel and the solid products were determined experimentally (Vario Macro CHN Analyzer). Based on these data, fictitious molecules for fuel and solid products were established. Gaseous products were analyzed by Fourier Transform Infrared Spectroscopy (FTIR) (see Krause and Schmidt, 2001; Schmidt et al., 2003, for information on experiments). From the experiments the following reaction was obtained:



Instead of containing elementary molecules as known from common chemical analysis, the reaction is composed of the fictitious molecules *fuel*, *oxygen*, *solid products*, and *exhaust gas*. Thus, the fictitious molecules represent mixtures of elementary reactants or products, and stoichiometric coefficients and molecular weights of these molecules were chosen to match the mass balance. The one-step chemical mechanism which is used here thus becomes



where ΔH in Jkg^{-1} is the heat released by the reaction and v_j are stoichiometric coefficients. Experimentally obtained values of stoichiometric coefficients, heat release and

molar weights are given in Tab. 2.1. The values are based on the analysis of coal samples collected in the Shenhua Group Coal Mining Area of Wuda (Inner Mongolia, PR China); for details on Wuda coal, see Dai et al. (2002). With these values, formula 2.7 describes the chemical conversion of one mole of solid fuel and 26 moles of gaseous oxygen to one mole of solid and 47 moles of gaseous reaction products.

Subscript j	ν_j [-]	M_j [$gmol^{-1}$]
f (<i>fuel</i>)	-1	1089
O_2 (<i>oxygen</i>)	-26	32
sp (<i>solid product</i>)	1	489
eg (<i>exhaust gas</i>)	47	30.5

Parameter	Value	Units
ΔH	2.19×10^7	Jkg^{-1}

Table 2.1 Stoichiometric coefficients ν_j and calorific value ΔH for Eq. 2.7 after Lohrer et al. (2004). Molecular weights M_j are used for the conversion from molecular to weight units (cf. Eq. 2.27).

2.2.2 Formulation of Conservation Equations

To properly describe the underground coal fire as an open reactive system, transport processes have to be included into the mathematical model. For the present work transport processes for energy and chemical species are considered, whereas convective motions are realized by hydraulic gas flow (cf. Fig. 2.3). These processes, as well as the consumption of fuel and the production of solid products are mathematically formulated in the following.

The formulation of balance equations is based on the single-continua approach, as described before. The general balance equation of any quantity Ψ is expressed by

$$\int_F \mathbf{j}_\Psi dF + \int_V \frac{\partial \Psi}{\partial t} dV - \int_V Q_\Psi = 0. \quad (2.8)$$

Further, assuming the existence of a REV, so that inhomogeneities of Ψ can be averaged, the application of Gauss theorem results in the differential formulation

$$\nabla \cdot \mathbf{j}_\Psi + \frac{\partial \Psi}{\partial t} - Q_\Psi = 0. \quad (2.9)$$

In the equations, V is a volume element, F is the area enclosing the volume element, \mathbf{j}_Ψ is the flux of the considered quantity, t is time and Q_Ψ is a source. The balance equation states that the rates of change of Ψ within a certain volume element equals the net flux through the surface of that volume element plus an external or internal consumption or production

of the quantity. The following balance equations can be derived from Eq. 2.9 by inserting the considered quantity, like fluid mass, thermal energy.

Hydraulic and Momentum Equations

For the present study, convective motions are assumed to take place by one single gas phase. Hence, one hydraulic and one momentum equation are formulated for the consideration of hydraulic gas flow. This assumption implies that microscopic partial pressure differences between dissolved chemical species are not considered. Thus, chemical components dissolved in the gas are assumed to be mixed and to be transported as an average cloud by motions of the gas phase.

Hydraulic Equation The description of gas motions is based on the macroscopic continuity or mass balance equation for a non deformable porous medium (constant porosity), which has been published in a variety of books, including those by Muskat (1937), Bear (1972), Dagan (1989), and Barenblatt et al. (1990). The balance equation reads

$$\Phi \frac{\partial \rho^f}{\partial t} + \nabla \cdot \mathbf{j}_m + Q_m = 0. \quad (2.10)$$

Here, ρ^f in kgm^{-3} is the fluid density, Φ is the non-dimensional porosity, Q_m in $kgm^{-3}s^{-1}$ is a mass source term, t in s is time and

$$\mathbf{j}_m = \rho^f \Phi \mathbf{v} \quad (2.11)$$

in $kgm^{-2}s^{-1}$ is the advective mass flux of gas, when dispersive and diffusive fluxes are neglected. \mathbf{v} in ms^{-1} is the microscopic or interstitial flow velocity, which is related to the macroscopic specific flow rate, \mathbf{q} in ms^{-1} , by the Dupuit-Forchheimer relation (see e.g. Dagan, 1989; Nield and Bejan, 1999). This relation is unequivocally correct for the case of uniform pores (Guin et al., 1971) and reads

$$\mathbf{q} = \Phi \mathbf{v}. \quad (2.12)$$

The fluid density needs to be formulated for gas. Here, an equation of state for an ideal gas can be assumed, because underground coal fires are exposed to the low-pressure, high-temperature regime. In that regime, the main free path between gas molecules is large, hence inter-molecular forces can be neglected. The equation of state for an ideal gas reads (Nickel, 1995)

$$PV = nRT. \quad (2.13)$$

T in K and P in Pa are temperature and pressure, n in moles is the mole number and $R = 8.31 Jmol^{-1}K^{-1}$ is the unified gas constant. Extension of Eq. 2.13 with the molar mass of air and re-arrangement yields the equation of state for the temperature and pressure dependent fluid density:

$$\frac{M_{air}}{R} \frac{P}{T} = \frac{nM_{air}}{V} = \rho^f. \quad (2.14)$$

$M_{air} = 29 \text{ g mol}^{-1}$ is the molar mass of air. The density model is graphically represented in Fig. 2.4 for a temperature and pressure range of $\Delta T = 900 \text{ K}$ and $\Delta P = 2000 \text{ Pa} = 20 \text{ mbar}$, respectively. The pressure range is typical for barometric pressure variations which have been monitored in the Shenhua Group Coal Mining Area of Wuda (Inner Mongolia, PR China). Furthermore, pressure differences appearing due to thermal buoyancy are in the order of 10^2 Pa (Schmal, 1987), so that the pressure range in Fig. 2.4 can be regarded as an upper bound. Concluding from the figure, density dependent pressure variations are small in comparison to the dependency on temperature.

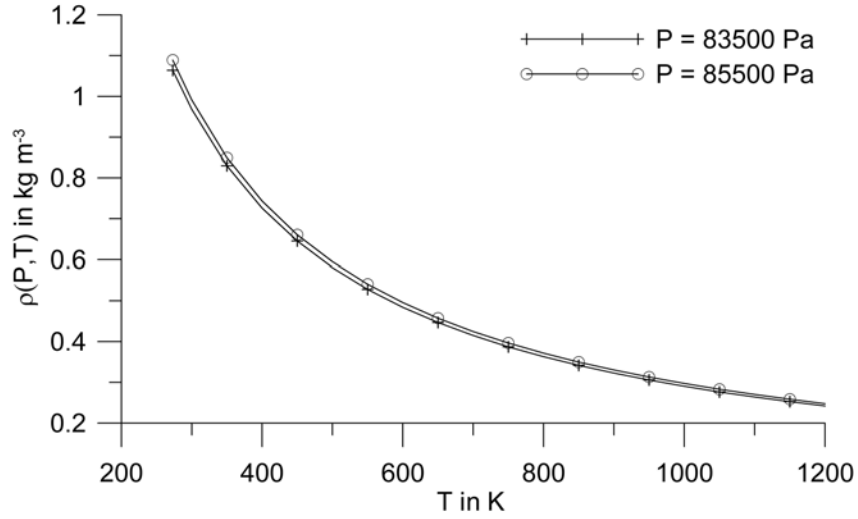


Figure 2.4 Density variations with respect to temperature and pressure changes within a range $\Delta T = 900 \text{ K}$ and $\Delta P = 2000 \text{ Pa} = 20 \text{ mbar}$

Continuing with the mass balance, Eq. 2.10 equates the rate of increase or decrease of the fluid mass within an elementary volume (the first term) to the net mass flux into that volume (the second term) plus gas mass production or consumption (the third term). For underground coal fires, the third term describes the production of gas mass due to the chemical conversion of solid coal into gaseous reaction products (exhaust gas). An estimation by Lohrer (2006) shows that mass production is negligibly small, so that the third term in Eq. 2.10 is omitted.

The second term in Eq. 2.10 (wherein Eqs. 2.11 and 2.12 are inserted) can be rewritten as

$$\nabla \cdot \rho^f \mathbf{q} = \rho^f \nabla \cdot \mathbf{q} + \mathbf{q} \cdot \nabla \rho^f. \quad (2.15)$$

The first term on the right hand side describes conservation of volume, whereas the second term describes gas compressibility whenever the gas density cannot be assumed to be constant. The second term can be neglected, when a characteristic length L_c^p over which significant changes in ρ^f take place is much larger than a characteristic length L_c^q over which significant changes in \mathbf{q} take place (Bear and Bachmat, 1990, p. 280). However, in the case of underground coal fires with thermal buoyancy as driving force, L_c^q and L_c^p are both directly depending on the temperature field. Thus, $L_c^q \ll L_c^p$ cannot be assumed and the

second term needs to be included in the model.

For the first term of Eq. 2.10, the concept of slight fluid compressibility is used to describe nonsteady gas flow in porous media (Barenblatt et al., 1990). The concept is based on differentiation of the time derivative term:

$$\Phi \frac{\partial \rho^f}{\partial t} = \Phi \left(\frac{\partial \rho^f}{\partial P} \frac{\partial P}{\partial t} + \frac{\partial \rho^f}{\partial T} \frac{\partial T}{\partial t} \right). \quad (2.16)$$

Hence, the time derivations of the pressure and the temperature appear. The time derivative of temperature is small in comparison to the time derivative of pressure, because pressure variations propagate much faster than any temperature disturbances. Thus, the time derivative term for temperature is omitted in Eq. 2.16. Furthermore, under the assumption of slight compressibility relative increments of ρ^f are small quantities, so that $\frac{\partial \rho^f}{\partial P}$ can be assumed constant.

Combining Eqs. 2.10, 2.11, 2.15 and 2.16 the used mass balance equation reads

$$S \frac{\partial P}{\partial t} + \nabla \cdot \mathbf{q} + \frac{1}{\rho^f} \mathbf{q} \cdot \nabla \rho^f = 0, \quad (2.17)$$

which is also known as the hydraulic equation. Here,

$$S = \Phi \frac{1}{\rho^f} \frac{\partial \rho^f}{\partial P} \quad (2.18)$$

is the constant storativity in Pa^{-1} and the fluid density is considered as temperature dependent only, because pressure variations are small and have therefore insignificant influence on density variations. With this assumption, a reference density $\rho_0^f(T_0)$ at the reference temperature T_0 can be introduced and the temperature dependent density can be expressed as

$$\rho^f = \rho_0^f(T_0) \frac{T_0}{T}. \quad (2.19)$$

This density model will be used throughout the thesis if not explicitly stated.

Momentum Equation For a closed system of equations, the specific flow rate \mathbf{q} needs to be defined. This is obtained from averaging the momentum conservation equation over macroscopic REV's. The simplest form of macroscopic momentum conservation is given by Darcy's law, describing a linear relation between pressure gradients and the specific flow rate:

$$\mathbf{q} = -\frac{k_{ij}}{\mu(T)} (\nabla P - \rho^f \mathbf{g}). \quad (2.20)$$

\mathbf{g} in $m s^{-2}$ is the gravitational acceleration, $\mu(T)$ in $Pa s$ is the temperature dependent dynamic fluid viscosity and k_{ij} in m^2 is the permeability tensor. Darcy's law is valid for laminar (creeping) flow, where inertia forces can be neglected. It has been used by some authors for the investigation of self-heating effects of coal (Krishnaswamy et al., 1996a; Gong et al., 1999).

For high flow rates, inertia effects become relevant. In the case of underground coal fires, high flow rates have to be expected due to high permeability of surrounding rocks (see Huang et al., 2001, for previous investigations). Additionally, theoretical investigations by De Ville (1996) confirm that the application of Darcy's law is inappropriate for compressible gas flow.

Therefore, the Forchheimer equation is used, which is a nonlinear extension of Darcy's law. The Forchheimer equation was theoretically derived by Whitaker (1996) and has frequently been applied to consider inertia flow through porous or fractured media (see e.g. Ruth and Ma, 1992; Kohl et al., 1997; Nield and Bejan, 1999; Skjetne et al., 1999). The Forchheimer equation was first proposed by Forchheimer (1901) and reads

$$\nabla P - \rho^f \mathbf{g} = -\frac{\mu(T)}{k_{ij}} \mathbf{q} - \frac{c_F}{\sqrt{k_{ij}}} \rho^f |\mathbf{q}| \mathbf{q}. \quad (2.21)$$

For simplicity, μ is assumed constant here, and the permeability becomes a scalar under the assumption of isotropy. $|\cdot|$ is the euclidian norm and c_F is a dimensionless form-drag constant, which may vary between 0.1 and 0.55 with the nature of the porous medium (Nield and Bejan, 1999). The second term on the left hand side of Eq. 2.21 describes thermal buoyancy which is of particular importance for underground coal fires.

An estimation of the relevance of nonlinear flow behavior formulated by the Forchheimer equation is presented in Appendix A. Eqs. 2.17 and 2.21 are a coupled set of equations which need to be solved to obtain the absolute pressure and the flow rate for convective species and heat transport.

Mass Balance Equations for Chemical Species

Chemical species need to be distinguished between solid and fluidal ones, because only the fluids are moving. Consumption and production processes for the solid components are formulated as

$$\frac{\partial c_j}{\partial t} = Q_j, \quad (j = f, sp), \quad (2.22)$$

where c_j in kgm^{-3} and Q_j in $kgm^{-3}s^{-1}$ are the macroscopically averaged bulk concentration and the source terms for fuel (f) and solid products (sp), which are involved in the chemical reaction, Eq. 2.7. The equations describe temporal changes in the concentrations due to the production or consumption rates of solid species. Consumption and production rates are formulated by the source terms, which are introduced below (Eqs. 2.26, 2.27).

For oxygen and exhaust gas transport, the conservation equations are expressed as (Kröhn, 1991; Yeh, 2000)

$$\frac{\partial \Phi c_j}{\partial t} + \mathbf{q} \nabla \bullet c_j - \nabla \bullet (\mathbf{D} \nabla \Phi c_j) + Q_j = 0. \quad (j = O_2, eg). \quad (2.23)$$

Here, c_j is the microscopic concentration of oxygen (O_2) or exhaust gas (eg) dissolved in the fluid. In the Eqs. 2.22 and 2.23, a distinction is made between the macroscopic bulk concentration for solid compartments (c_f, c_{sp}) and the microscopic species concentrations contained in the fluid (c_{O_2}, c_{eg}). This distinction is made to use comparable values obtained

from laboratory or *in-situ* measurements. In such measurements, the concentration of a solid material (like coal) is commonly determined according to a volume-averaged concentration of pure minerals plus the fluid contained in the porous solid material. Hence, if Φ is the porosity of the solid material, the bulk concentration, c_{bulk} , becomes

$$c_{bulk} = (1 - \Phi)c_m + \Phi c_{fl}, \quad (2.24)$$

where c_m is the pure mineral concentration (without pores), and c_{fl} is the concentration of the fluid contained in the pores. In contrast, the concentration of species contained in the pores is determined according to its amount contained in the pure fluid phase. E.g., if the oxygen concentration in the air contained in a porous block is determined, one obtains values only for the pure oxygen concentration, without knowing the porosity of that solid material. Hence, the definition of an average oxygen concentration as described by Eq. 2.24 makes no sense.

In Eq. 2.23, Q_j is the source term for oxygen and exhaust gas and \mathbf{D} represents the macroscopic dispersion tensor (Scheidegger, 1961), which in turn depends on the longitudinal and transverse dispersion lengths, α_L and α_T in m , and the molecular diffusion coefficient D_{mol} in $m^2 s^{-1}$ (for definition, see Bear, 1972).

The first term of Eq. 2.23 describes temporal changes in concentration. Changes result from convective and dispersive transport as described by terms two and three, and from consumption or production of fluidal species as considered by the source term. Convection (the second term) is coupled to the hydraulic and momentum equations (Eqs. 2.17, 2.21) by the specific flow rate \mathbf{q} . Usage of the specific flow rate for convective transport is based on the simplifying assumption that chemical species dissolved in the gas are of equal molar weight. Hence, mixing between dissolved chemical species within the gas phase cannot be considered under the assumed simplifications. According to Banerjee et al. (1986) mixing is important for combustion as it cares for increased availability of oxygen. However, the purpose of the present study is the simulation of underground coal fires on large scales, so that small-scale effects like mixing are out of consideration here.

Finally, Eq. 2.23 contains the consumption/production (source term) as well as the transport of oxygen and exhaust gas. Coupling between chemical reactions in the seam and the transport of fluidal species through adjacent beds is thus realized by the reactive transport equations.

Reaction Kinetics Formulation

The source terms Q_j for Eqs. 2.22 and 2.23 will be given next. Due to the heterogeneous nature of the chemical reaction, i.e. the reaction between solids and fluids, the source term formulations become complicated. As the Arrhenius formulation results from molecular collision theory between reactive gas molecules, such formulation is suitable to a limited extend for heterogeneous systems. In such systems collision between reacting molecules takes place between gaseous and solid species, the latter ones being located at the inner surface of the solid material (Zelkowsky, 1986). Additionally complicating, the inner surface is not necessarily reactive, so that only a fractional amount, the inner reactive surface,

contributes to the combustion.

Different authors theoretically describe the relation between the inner reactive surface and the reaction rate (Annamalai and Ryan, 1993; Lichtner, 1996). Also, a formulation of the inner reactive surface was used for the simulation or theoretical investigation of combustion phenomena. E.g., Brooks and Glasser (1986) assumed a first-order surface reaction for their theoretical considerations, with the constants in the reaction rate expressions being proportional to the particle size. In order to take changes in the inner reactive surface into account, Perkins and Sahajwalla (2005) use a random pore model according to Bhati and Perlmutter (1980) and Gavalas (1980):

$$A = A_0(1 - X)\sqrt{1 - \psi \ln(1 - X)}. \quad (2.25)$$

In Eq. 2.25, A is the reactive surface area per unit volume, ψ is the pore structure parameter (Liu, 1999; Liu et al., 2000) and X is the char conversion.

Obviously, petrophysical properties of coal plays an important role to derive formulations of the reactivity. However, Arenillas et al. (2003) found that the relationship between reactivity and texture (inner surface) cannot be taken as a general rule, and surface area values cannot be used directly as an indicator for reactive properties of coal. Thus, a proper and experimentally verified formulation between the inner reactive surface and the reaction rates for chemical reactions with coal are still one topic for research activities. Despite a hardly known relation between reactivity and inner reactive surface, an exponential dependency of the reaction rates with temperature remains a promising expression (cf. Lichtner, 1996, p. 14ff), because the mean free path of gas molecules still exponentially decreases with increasing temperature. Note that these kinetic parameters have to be considered as empiric formulations (Zelkowski, 1986).

The combustion process depends on the availability of both, fuel and oxygen (McPherson, 1993). Whenever the concentrations of one of these species becomes zero, the combustion does not proceed. Thus, the reaction rates as described by Q_j should be formulated in a way that the concentrations of oxygen and fuel are incorporated. This requirement is fulfilled by a second-order Arrhenius formulation (see e.g. Lichtner, 1996). For the present work a second-order formulation is used similar to the one proposed by Schmidt et al. (2003). In their work fuel (subscript f) is taken as the leading component, for which the source term is formulated as

$$Q_f = -c_f c_{O_2} k_0 e^{-\frac{E}{RT}}. \quad (2.26)$$

Here, k_0 in $m^3 s^{-1} kg^{-1}$ is the pre-exponential factor and E in $J mol^{-1}$ is the activation energy. Source terms for the other components (O_2, sp, eg) are related to Eq. 2.26 through their stoichiometries and molar masses:

$$Q_j = \frac{v_j M_j}{v_f M_f} Q_f. \quad (2.27)$$

Eq. 2.26 depends on the oxygen and fuel concentrations, and on the temperature. This kind of Arrhenius formulation poses the main challenge for the numerical simulation, but its usage is physically reasonable because it takes increasing reaction kinetics due to increasing collision between molecules with increasing temperatures into account. For the present

work, E and k_0 were determined from laboratory experiments for coal samples from the Wuda coal. These parameters were obtained from an analysis of self-heating experiments, which are described in App. B. Values for E and k_0 are given in Tab. 2.2.

Parameter	Value	Units
$E R^{-1}$	1.27×10^4	K
k_0	4.7×10^6	$m^3 kg^{-1} s^{-1}$

Table 2.2 Reaction kinetic parameters after Schmidt et al. (2005) as obtained from the F-K Analysis method for samples from the Wuda coal

Energy Conservation Equation

The transport of heat through the seam and the over- and underlying beds affects the combustion temperature. Due to high combustion temperatures, three heat transport mechanisms need to be considered: conduction, convection and radiation. Under the assumption of thermal equilibrium between solid matrix and gas, the balance for thermal energy is formulated by the heat transport equation (Whitaker, 1999):

$$c^b \frac{\partial T}{\partial t} + \nabla \cdot \mathbf{j}_h - Q_H = 0. \quad (2.28)$$

c^b in $J m^{-3} K^{-1}$ is the bulk heat capacity. Q_H in $J m^{-3} s^{-1}$ is a source term, which is related to the fuel consumption source according to

$$Q_H = -\Delta H Q_f \quad (2.29)$$

and considers the heat generated from the chemical reaction, Eq. 2.7. In the second term, \mathbf{j}_h in $J m^{-2} s^{-1}$ is the heat flux, which is expressed as

$$\mathbf{j}_h = \mathbf{j}_c + \mathbf{j}_F + \mathbf{j}_r. \quad (2.30)$$

The heat flux is a result of three mechanisms, which are convection, conduction and radiation. The convective heat flux is formulated as

$$\mathbf{j}_c = \rho^f c_p^f \mathbf{q} T, \quad (2.31)$$

where c_p^f in $J kg^{-1} K^{-1}$ is the specific heat of gas. Fourier's law of heat conduction is given by

$$\mathbf{j}_F = -\lambda_0 \nabla T, \quad (2.32)$$

and a linearized form of Stefan-Boltzmann's law for heat radiation reads (see Kappelmeyer and Haenel, 1974)

$$\mathbf{j}_r = -\lambda_r \nabla T. \quad (2.33)$$

The linearization is reasonable if the mean free path of radiation is small compared to the distance to material discontinuities and for moderate temperature gradients. λ_0 in $W m^{-1} K^{-1}$ is the constant thermal conductivity at room temperature T_0 and λ_r is the radiative thermal conductivity (Clauser, 2006), which is assumed to be

$$\lambda_r = \beta(T - T_0)^3. \quad (2.34)$$

β in $W m^{-1} K^{-4}$ is a constant. Thus, the heat flux in Eq. 2.28 becomes

$$\begin{aligned} \mathbf{j}_h &= \rho^f c_p^f \mathbf{q} T - (\lambda_0 + \lambda_r) \nabla T \\ &= \rho^f c_p^f \mathbf{q} T - (\lambda_0 + \beta(T - T_0)^3) \nabla T \\ &= \rho^f c_p^f \mathbf{q} T - \lambda_{eff} \nabla T, \end{aligned} \quad (2.35)$$

and describes convective, conductive and radiative energy transport, whereby the latter is strongly increasing with increasing temperature. Stefan-Boltzmann's law has been linearized by a series expansion around T_0 (compare Eq. 2.34) in order to consider laboratory values for λ_0 at room temperature. For $\beta = 7 \times 10^{-9} W m^{-1} K^{-4}$ and $\lambda_0 = 0.1 W m^{-1} K^{-1}$ for coal and $\lambda_0 = 2.0 W m^{-1} K^{-1}$ for rock, the temperature dependent thermal conductivity formulation is graphically presented in Fig. 2.5.

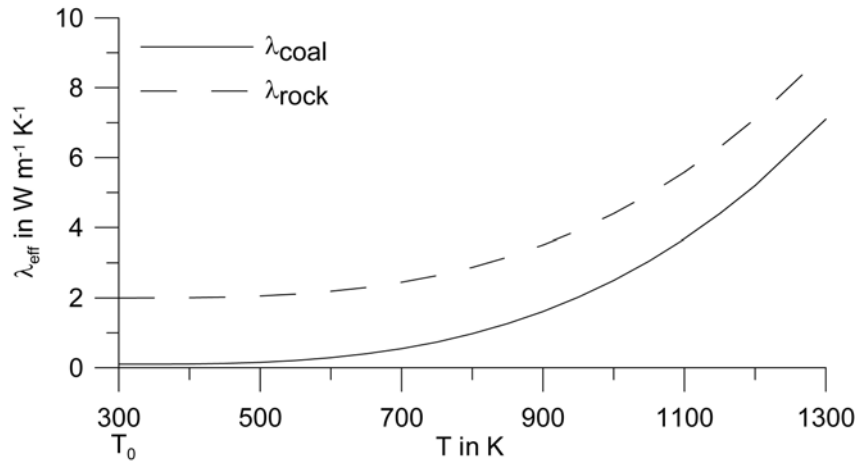


Figure 2.5 Temperature dependent thermal conductivity $\lambda_{eff}(T) = \lambda_0 + \beta(T - T_0)^3$ according to Eq. 2.35 for $\beta = 7 \times 10^{-9} W m^{-1} K^{-4}$.

As presented in Fig. 2.5, Eq. 2.35 considers strongly increasing thermal conductivities at high temperatures. Slightly weaker increasing values with increasing temperature were observed by Saegusa et al. (1974) from experiments in porous media. Additionally, various combustion modelers like Hjertager (1986) and Brenner et al. (2000) use complex formulations for radiation, which are validated by experiments.

However, laboratory experiments are performed on probes containing small-scale discontinuities (see Fujitsu et al., 1977; Vortmeyer, 1980). In contrast, combustion centers of

underground coal fires are likely composed of large-scale solid blocks which are packed in a way that large-scale voids exist. These blocks occur due to mechanical failure of the surrounding rock and fill the burnt coal seam. Thus, proper description of radiative heat transport within and around the combustion center for theoretical predictions requires large-scale experiments or a precise image of the discontinuities. As neither of these is known, the introduced simple formulation of temperature dependent thermal conductivity is used to include radiation.

2.2.3 Formulation for the Macroscopic Drop of Oxygen Concentration in the Combustion Front

Finally, the combustion front is discussed with respect to the drop of oxygen concentration for later discussion about the numerical approach. Based on a hypothetical model, a minimum Representative Length is introduced over which the average drop of oxygen concentration takes place. It thus describes the macroscopic oxygen drop in the combustion front, thereby leaving some uncertainty for processes taking place at scales smaller than the Representative Length. Those processes remain out of consideration by the model.

Similar models for the drop of oxygen concentration were previously described for single coal particles or small clouds of coal particles (see Annamalai and Ryan, 1994, for a comprehensive overview). However, these investigations were performed for small-scale particles as contained in pulverized coal. In such medium the drop is termed 'penetration depth', and depends on the interplay between reaction kinetics and diffusion in the immediate surrounding of the coal particles. Estimates were also discussed in Kessels et al. (2006a), where the penetration depth of oxygen was determined from a first-order reaction kinetics formulation. Kessels et al. (2006a) show that, at high temperatures, the penetration depth becomes inherently small, hence grid refinements would be necessary for an accurate resolution. Thus, a different definition seems to be necessary for the description of macroscopic reactive transport phenomena involved in underground coal fires.

The discussion is based on the schematic illustration in Fig. 2.6, presenting the top view of a combustion front. The combustion front is also termed 'reactive region' because chemical reactions take place in this part of the coal seam. The front as well as the gas are assumed to propagate in positive y -direction. Thus, oxygen is transported into the combustion zone from below.

The combustion zone is divided into two regions (a) and (b), as represented by the dashed line (Fig. 2.6). Both regions are highly disturbed due to combustion-induced cavities, thermal cracking and large-scale damages through mechanical failure. Additionally, natural inhomogeneities likely exist in and around the coal seam. The difference between the regions is that (a) contains reactive coal, which might additionally be mixed with rock compartments, whereas (b) is composed of inert material like ash and rock accumulations from the surrounding. The second region (b) results from coal burnout as well as subsidence or mechanical damage of the overlying beds. Reactive material does not exist in that region.

Somewhere in region (a), isoline 1 separates the untouched coal with initial coal concentration $c_{f,0}$ from the currently reacting coal, where $c_f < c_{f,0}$. Above isoline 1, coal is not

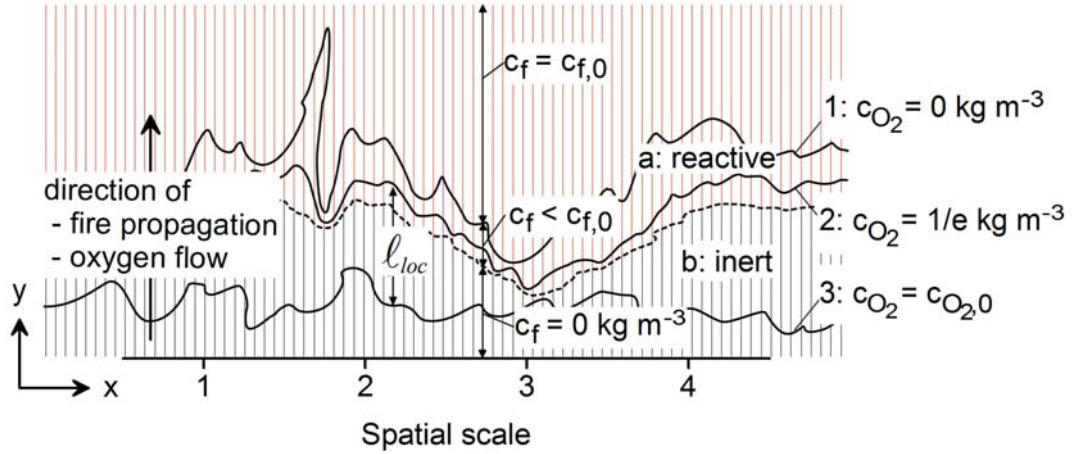


Figure 2.6 Schematic illustration of a macroscopic combustion front. Oxygen flow and fire propagation are in positive y -direction. The combustion front is divided into two regions, a and b , which are separated by the dashed line and marked in different color. Region a contains reactive crushed coal, region b contains inert crushed material. c_f and c_{O_2} are the coal and oxygen concentrations. The lines represent isolines, where $c_{O_2} = 0 \text{ kg m}^{-3}$ (isoline 1), $c_{O_2} = 1/e \text{ kg m}^{-3}$ (isoline 2), and $c_{O_2} = c_{O_2,0}$ (isoline 3). $c_{f,0}$ is the initial concentration of original coal in place. l_{loc} is the local representative length, which likewise defines the depth of the reactive region.

reacting with oxygen, because oxygen (which is transported from below) has completely been consumed in the reactive region (a) between the dashed line and isoline 1. Thus, oxygen concentration is zero at isoline 1. In region (b) isoline 3 exists at which the oxygen concentration begins to decrease (in the y -direction) from the initial oxygen concentration of air, $c_{O_2,0}$, to zero (isoline 1) because of the oxygen consumption in the reactive region (a). These two isolines represent in fact some transition zones of finite thickness. We introduce a local Representative Length l_{loc} in m as the length over which the oxygen concentration decreases from the initial value $c_{O_2,0}$ to some characteristic lower value, say $1/e$, the latter is given by isoline 2 (Fig. 2.6). This length likewise defines the depth of the reactive region.

There is reasonable evidence that the Representative Length varies because of the heterogeneous nature of the combustion zone. E.g., if large voids exist in the inert region (b), turbulent mixing yields high oxygen concentrations close to the reactive front, so that l_{loc} becomes small. In contrast, the local drop might become large, whenever the reactive front is covered by solid but fine-grained inert material, so that the transport of oxygen to the reactive front occurs smoothly. Summarizing, both, magnitude and location of l_{loc} are likely varying on macroscopic spatial scales.

For macroscopic scales we define the macroscopic Representative Length as

$$\ell = \int \ell_{loc}(x) dx. \quad (2.36)$$

Herein ℓ is the average over local representative lengths.

So far, the model is an assumption and needs to be verified through experiments or *in-situ* observations. There is reasonable evidence that combustion zones below surface are composed of large-scale discontinuities due to mechanical failure. It is unlikely that mechanical failure produces exclusively fine-grained material (coal and rock).

2.2.4 Initial and Boundary Conditions

To uniquely solve the above introduced set of differential equations, boundary and initial conditions need to be given for the pressure, the temperature, and the chemical species.

Initial condition for the absolute pressure P_i is a hydrostatic distribution, with an initial reference value P_0 at a reference location z_0 :

$$P_i(z) = P_0(z_0) + \rho_0^f(T_0)(z_0 - z)\mathbf{g}. \quad (2.37)$$

The initial temperature is assumed to be one single value T_0 for the whole system. Hence, any geothermal gradient is not considered. Initial conditions for the solid components are set in the coal seam, with some initial concentration $c_{f,0}$ for the coal and zero solid product concentration, $c_{sp,0} = 0 \text{ kg m}^{-3}$. For the gas components an initial concentration $c_{O_2,0}$ for oxygen and a zero exhaust gas concentration $c_{g,0} = 0 \text{ kg m}^{-3}$ are presumed.

Due to the connection between underground coal fires and the atmosphere by the air circulation through surrounding beds, boundary conditions need to be explained in more detail. At the surface above an underground coal fire, an exchange takes place between the coal seam and the atmosphere. At some locations hot exhaust gas leaves the surface, thereby producing a slightly increased pressure in comparison to the barometric pressure. At other locations fresh air may flow into the subsurface, thereby exhibiting atmospheric conditions. Obviously, a distinction needs to be made between boundary locations where gas enters or leaves the surface. For the simulation, the exchange between the atmosphere and the circulation system must be considered, which, in reality takes place within a small atmospheric layer immediately above the surface.

For the pressure, Dirichlét boundary conditions are assumed, without making a distinction between in- and outflowing gas. Hence, a distinction between the slight pressure increase or decrease at locations with out- or inflowing gas cannot be made. From simulation results, those locations can be distinguished by the flow directions observed at the boundaries. The value for boundary conditions is assumed to be the reference barometric pressure.

For temperature and fluid concentrations a distinction is made between the locations where gas leaves or enters the surface. Whenever gas enters the surface, Dirichlét boundary conditions are assumed, with presumed reference temperature and fluid concentrations prevailing in the atmosphere. At locations where gas leaves the surface, Neumann boundary conditions are assumed. Such boundary conditions prescribe a zero conductive or diffusive flux of thermal energy or chemical components. However, convective transport can take place here. The usage of Neumann conditions is an assumption, because they are only appropriate when convection is the dominant transport mechanism of heat and chemical components.

2.3 Estimation of Time Scales

After introducing of the assumed physico-chemical model, an estimation of time scales for oxygen transport and oxygen consumption is now presented. These scales pose the main challenge for simulations and are thus the motivation for further developments of numerical algorithms.

Numerical simulations become critical whenever the time scales vary over large magnitudes. The smallest time scale needs to be resolved to obtain a stable transient solution. The largest time scale controls the overall dynamic process, which is the fire propagation rate in this case. At the end of this section, a discussion of time scales estimation is presented based on parameters obtained from laboratory experiments.

2.3.1 Time Scales for Reaction Kinetics

For a first-order reaction the time scales for reaction kinetics are obtained by equating the reaction-only term of Eq. 2.23 (Young and Boris, 1977; Kessels et al., 2006a):

$$\frac{\partial c_j}{\partial t} = Q_j = -L_j c_j. \quad (2.38)$$

L_j in s^{-1} is the inverse loss time for component j and is related to the characteristic loss rate τ_j^{-1} according to

$$L_j = \tau_j^{-1}. \quad (2.39)$$

Eq. 2.39 describes how quickly the concentration of the species j is consumed. If τ_j is constant, Eq. 2.38 can be solved analytically to yield

$$c_j(t) = c_j(0)e^{-t/\tau_j}. \quad (2.40)$$

In the present case a second-order formulation for reaction kinetics is used, so that the time scales τ_j^r in s (superscript r denotes reaction) resulting from reaction kinetics for species j are defined as (Zysset et al., 1994)

$$\tau_j^r = c_j Q_j^{-1}. \quad (2.41)$$

For oxygen consumption ($j = O_2$) the time scales become

$$\tau_{O_2}^r = c_{O_2} Q_{O_2}^{-1} = \frac{v_f M_f}{v_{O_2} M_{O_2}} (c_f k_0 e^{-\frac{E}{RT}})^{-1}, \quad (2.42)$$

with the definitions of the source terms, Eqs. 2.26 and 2.27. $\tau_{O_2}^r$ exponentially depends on the temperature due to the Arrhenius formulation. Thus, increasing temperatures result in an exponential decrease of the relevant time scales, so that oxygen consumption takes place inherently fast at sufficiently high temperatures.

2.3.2 Time Scales for Oxygen Transport

In case of convection dominance the specific flow rate $|\mathbf{q}| = q$ of gas defines the time scales for oxygen transport. q is given by Darcy's law (Eq. 2.20), which can be considered as an upper bound of the flow rate obtained from the non-linear Forchheimer equation (Eq. 2.21). In the absence of externally imposed pressure gradients, the order of magnitude of q scales with thermal buoyancy and is estimated as

$$q \sim \frac{k}{\mu} \Delta \rho^f |\mathbf{g}|. \quad (2.43)$$

The density model for an ideal gas (Eq. 2.19) applies:

$$\Delta \rho^f = \rho_0^f \frac{T - T_0}{T} = \rho_0^f \frac{\Delta T}{T}. \quad (2.44)$$

The time scales for oxygen transport are obtained from relating the convective transport term to the transient term (Eq. 2.23), i.e.

$$\frac{\Delta c_{O_2}}{\Delta t_{O_2}^t} \sim v \frac{\Delta c_{O_2}}{L_c^{O_2}} = \frac{q}{\Phi} \frac{\Delta c_{O_2}}{L_c^{O_2}}. \quad (2.45)$$

$L_c^{O_2}$ in m is a characteristic length over which significant changes in oxygen concentration, Δc_{O_2} , occur. Finally, the combination of Eqs. 2.43 and 2.45 defines the temperature dependent time scales $\tau_{O_2}^t$ in s at which oxygen transport takes place:

$$\tau_{O_2}^t := \Delta t_{O_2}^t \sim \frac{\Phi L_c^{O_2}}{\frac{k}{\mu} \rho_0^f \frac{\Delta T}{T} |\mathbf{g}|}. \quad (2.46)$$

These time scales basically depend on two unknown parameters: the permeability k and the characteristic length $L_c^{O_2}$. The latter is the macroscopic Representative Length ℓ as introduced in Sec. 2.2.3. The permeability depends on the microscopic structure of porous and/or fractured rocks. It ranges between some orders of magnitude (Nield and Bejan, 1999), so that $\tau_{O_2}^t$ depends on the properties of the considered rocks. However, the permeability is nearly independent on temperature variations, as long as thermal cracking or thermal expansion are negligibly small. Thus, time scales vary with $T/\Delta T$ once the permeability of any rock formation has been determined.

2.3.3 Conclusion from Scale Estimates

The time scales according to Eqs. 2.42 and 2.46 are graphically represented in Fig. 2.7 with respect to temperature variations. Parameters for $\tau_{O_2}^t$ (Eq. 2.42) are taken from laboratory measurements and have been specified in Tabs. 2.1 and 2.2. For $\tau_{O_2}^t$, ℓ is assumed to be in the order of 10^{-1} meters, and a high permeability of $k = 10^{-7} m^2$ has been taken as an upper bound.

The diagram shows that the time scales $\tau_{O_2}^t$ vary over one order of magnitude with respect to temperature variations. Of course, different permeabilities result in different magnitudes,

but the temperature dependency remains small. The time scales for oxygen consumption are large at low temperatures, i.e. the reaction kinetics are very slow. In contrast, time scales $\tau_{O_2}^r$ in the order of 10^{-5} seconds are obtained for the oxygen consumption at combustion temperatures around 1200K.

From the estimation of time scales, the process controlling the overall combustion rate and therefore being the dominating process for the fire propagation can be determined. At low temperatures, oxygen consumption is the slower processes. The combustion rate is therefore controlled by reaction kinetics. At high temperatures, reaction kinetics are very fast, due to the exponential dependency of the source term in Eq. 2.26. Thus, immediate consumption of all the oxygen takes place that is available within the combustion center. Combustion will only proceed when transport processes provide further oxygen. In that case, oxygen transport controls the overall combustion rate.

The next section provides a numerical approach aiming to cope with the problem of very small time scales.

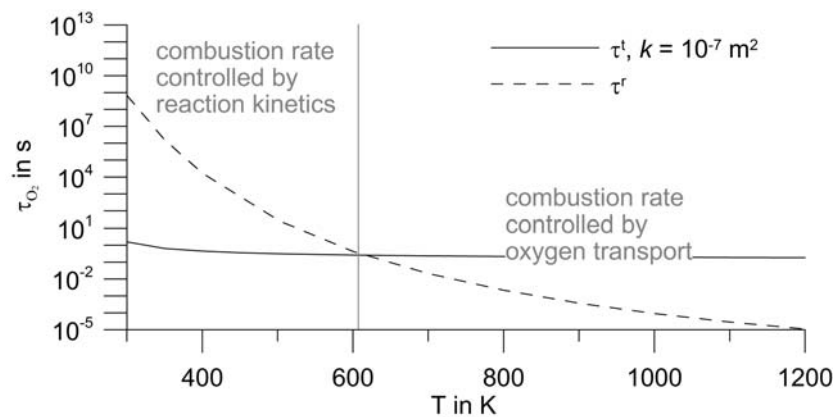


Figure 2.7 Illustration of the temperature dependent time scales, τ^r for oxygen consumption and τ^t for oxygen transport. The calculation of τ^r is performed according to Eq. 2.42, with parameters taken from Tabs. 2.1 and 2.2. The calculation of τ^t is performed according to Eq. 2.46, with $L_c^{O_2} = \ell = 0.1 \text{ m}$.

3 Numerical Realization of the Simulation

In the previous chapter, an estimation showed the wide range of time scales, posing the main challenge for any simulation. In particular, very fast reaction kinetics at high temperatures would require very small time steps to resolve τ_{O_2} . Numerical calculations to solve the reactive transport equations (Eqs. 2.23) with common approaches would be impractical because calculation times would become inherently long. Numerical investigation into the dynamic evolution of underground coal fires would thus be impossible.

Two approaches are commonly used to solve differential equations: the direct approach and the operator-splitting approach. The former solves the whole system within a single time step, in the latter one the system to be solved is split into a transport-only and a chemistry-only part. Operator-splitting methods received much attention in the last decades, where investigations on numerical errors (Barry et al., 1996, 1997; Carrayrou et al., 2004) and the convergence behavior of different operator-splitting schemes (Kanney et al., 2003) had been addressed. Additionally, operator-splitting techniques have been applied for the simulation of reactive transport phenomena (see Walter et al., 1994; Zysset et al., 1994; Barry et al., 1996, 1997; Xu et al., 1999; Kanney et al., 2003; Carrayrou et al., 2004, and references therein).

This chapter presents the use of an operator-splitting approach. Attention is paid on the high temperature regime, where the combustion process is controlled by oxygen transport instead of reaction kinetics. The aim of applying the operator-splitting approach is to separate between oxygen transport and reaction kinetics, and to consider only that process which controls the combustion rate. Common numerical programs use the operator-splitting approach to solve stiff sets of equations (Oran and Boris, 2001), i.e. equations whose time scales vary over some orders of magnitude. However, operator-splitting has not yet been applied to differentiate between reaction kinetics and oxygen transport at high temperatures in order to control the propagation rate of underground coal fires by oxygen transport.

After presenting some basics about the finite-element simulator Rockflow¹ the application of the operator-splitting approach is explained. Newly implemented program parts are then verified. A simulation example is given at the end of this chapter.

3.1 The Finite-Element Simulator Rockflow

The simulation of underground coal fires is performed by solving Eqs. 2.17, 2.21, 2.22, 2.23, and 2.28, together with the source term definitions, Eqs. 2.26, 2.27 and 2.29. We here use the simulator Rockflow, which has been developed during various Ph.d. studies (see Kröhn, 1991; Habbar, 2001; Kaiser, 2001; Thorenz, 2001, for recent theses). Rockflow solves common differential equations for water and gas hydraulics, as well as energy

¹ISEB, University of Hannover, <http://www.hydromech.uni-hannover.de>

and species transport through porous and/or fractured media (expressed by Eqs. 2.17, 2.21, 2.22, and 2.23, 2.28 without source terms). The simulator is based on the finite-element discretization method and is therefore especially useful for the representation of complex geological formations.

Transport equations for thermal energy and species without chemical reaction, as well as the hydraulic equation are solved with the numerical algorithms implemented by Thorenz (2001). A Petrov-Galerkin upwinding scheme is used to avoid numerical oscillations. The algebraic set of equations resulting from discretization is solved with a Conjugate-Gradients method.

The above said equations, together with the source term definitions (Eqs. 2.26, 2.27, 2.29) are non-linearly coupled. To take these couplings into account a non-linear solver is necessary. Frequently applied solvers for non-linear sets of equations are the Picard-Iteration or a Newton-Rhapson method.

For this study the non-linear coupling is avoided by the linearization of the equations, i.e. values of coupling primary variables which appear in a balance equation are taken from the previous time step. Doing so, solving is performed by a successive calculation as summarized in Tab. 3.1.

The linearization introduces insignificant errors because the coupling between the primary variables pressure and temperature is very weak as long as the time step remains small compared to the time scales at which the propagations of pressure and temperature take place.

For the previously described numerical solvers, Thorenz (2001) performed comprehensive tests, hence another verification of the existing algorithms has not been done.

P, T, c_i from previous time step			
	↓		
	hydraulic equations	Eqs. 2.17, 2.21	coupled to T
	↓		
/	species transport	Eqs. 2.23	coupled to \mathbf{q}
operator-splitting	↓		
\	species reactions	Eqs. 2.26, 2.27	coupled to T
	↓		
	update energy source	Eq. 2.29	coupled to c_i
	↓		
	energy transport	Eq. 2.28	coupled to \mathbf{q}, c_i

Table 3.1 Sequence of solving the non-linear set of equations. Eqs. 2.23 are solved by the operator-splitting approach.

3.2 Algorithms for Reactive Transport Simulation

Subsequently introduced numerical procedures are based on the idea of timestep splitting. The idea is to evaluate independently the changes in the physical variables due to the different processes (Oran and Boris, 2001). Then, these processes are combined in some way to obtain the composite change. An advantage of this approach is that it avoids many costly matrix operations and allows the best numerical method to be used for each type of term or process. A potential disadvantage is that the separate algorithms can be more complex and usually differ from term to term.

Applying of an operator-splitting approach aims to control the fuel consumption rate by the transport of oxygen into the reactive region of the underground coal fire. The fuel consumption rate determines the fire propagation rate, i.e. the rate at which the combustion is penetrating through the coal seam.

3.2.1 Application of Operator-Splitting

In Sec. 2.2.2, a set of partial differential equations (cf. Eqs. 2.22 and 2.23) has been formulated that describes reactive transport phenomena. The equations contain source terms expressing the reactive conversion of chemical components. The source terms for a specific chemical component might depend on other chemical components, so that the differential equations are coupled with each other. In the present model, Eqs. 2.22 for fuel and 2.23 for oxygen are coupled through the source terms defined by Eqs. 2.26 and 2.27.

The operator-splitting approach is applied to the reactive transport equations for chemical species (cf. Eqs. 2.23):

$$\frac{\partial \Phi c_j}{\partial t} + T(c_j) + Q_j(c_{O_2}, c_f) = 0, \quad (j = O_2, eg). \quad (3.1)$$

Here,

$$T(c_j) = \mathbf{v} \nabla \bullet \Phi c_j - \nabla \bullet (\mathbf{D} \nabla \Phi c_j) \quad (3.2)$$

is a transport operator, and $Q_j(c_{O_2}, c_f)$ is the source term from Eq. 2.27, i.e. the operator describing the chemical conversion of species. Taking an explicit Euler time integration as example, the operator-splitting procedure is performed by first solving the transport-only part of Eq. 3.1,

$$c_j^* = c_j^t - \frac{\Delta t_{tr}}{\Phi} T(c_j^t), \quad (3.3)$$

giving the intermediate solution c_j^* . Δt_{tr} is the time step over which oxygen transport takes place. The second step is performed by nodewise solving the chemical conversion of species for a second time step Δt_{ch} i.e.,

$$c_j^{t+\Delta t_{ch}} = c_j^* - \frac{\Delta t_{ch}}{\Phi} Q_j(c_{O_2}^t, c_f^t) \quad (j = O_2, eg) \quad (3.4)$$

$$c_j^{t+\Delta t_{ch}} = c_j^t - \Delta t_{ch} Q_j(c_{O_2}^t, c_f^t) \quad (j = f, sp), \quad (3.5)$$

where either c_j^* for fluid components or c_j^t for solid components is used as initial value. The size of Δt_{ch} depends on the temperature regime of the system. At low temperatures, oxygen

consumption takes place over time scales being large in comparison to Δt_r . In that case, $\Delta t_{ch} = \Delta t_r$ applies. At high temperatures oxygen consumption takes place at very small time scales, as estimated before. To obtain a numerically stable solution, Eqs. 3.4, 3.5 are solved over a number n of successive time steps Δt_{ch} , whereas each time step is determined according to

$$\Delta t_{ch} = \alpha \tau_{O_2}^r. \quad (3.6)$$

The calculation is performed until the sum of time steps for consumption is as large as Δt_r :

$$\sum_n \Delta t_{ch} = \Delta t_r. \quad (3.7)$$

If the sum becomes larger than Δt_r , the last time step is determined as the difference between Δt_r and $\sum_{n-1} \Delta t_{ch}$. In Eq. 3.6, α is a constant and $\tau_{O_2}^r$ is the time scale of oxygen consumption defined in Eq. 2.42.

The procedure of subsequent oxygen transport and consumption is graphically illustrated in Fig. 3.1, showing the oxygen consumption during one time step for oxygen transport (Δt_r). After consumption, oxygen transport refills the reactive zone at the end of Δt_r . Thus, the oxygen concentration increases in dependence on the transport properties of oxygen. At temperatures $T = 410K$ oxygen consumption does not completely reduce the oxygen concentration within Δt_r to zero. At $T = 450K$ oxygen is reduced to a very low value, so that continuous calculations give insignificant changes in the concentrations. Therefore, a cutoff concentration is set at values smaller than $c_j = 10^{-6} kg m^{-3}$ for fuel and oxygen ($j = f, O_2$). Once the concentration gets smaller than that value, the calculations of the chemical consumption stops.

From the phenomenological perspective the operator-splitting approach can be regarded as follows: Within Δt_r oxygen transport fills the reactive region of the combustion center with oxygen. Subsequently, but within the same time step, oxygen and fuel are consumed and exhaust gas and solid products are produced due to the chemical reaction. After the chemical reaction, calculations are performed for the next time step, beginning with the oxygen refill of the reactive region. The operator-splitting approach differentiates between the different time scales for transport and consumption of oxygen, hence the combustion rate can be calculated as the amount of oxygen being consumed during the time required for oxygen transport.

Eqs. 3.4, 3.5 represent a set of ordinary differential equations, which are coupled through the source terms $Q_j(c_{O_2}, c_f)$. Each equation is numerically solved with a predictor-corrector integration, which has been proposed by Young and Boris (1977) and later been used e.g. by Zysset et al. (1994). The coupling between the equations is solved with a standard Picard-Iteration, until the relative error $\epsilon_r < 10^{-6}$ is reached.

For the presented approach the refill of the reactive region through oxygen transport needs further explanations. The depth of the reactive region has been illustrated in Fig. 2.6 as l_{oc} . In reality, the depth depends on the interplay between oxygen transport into and oxygen consumption within the reactive region. In the numerical model, the interplay is omitted due to the operator-splitting approach. Hence, only the oxygen transport controls the penetration depth into the reactive region, whereas the consumption is subsequently calculated.

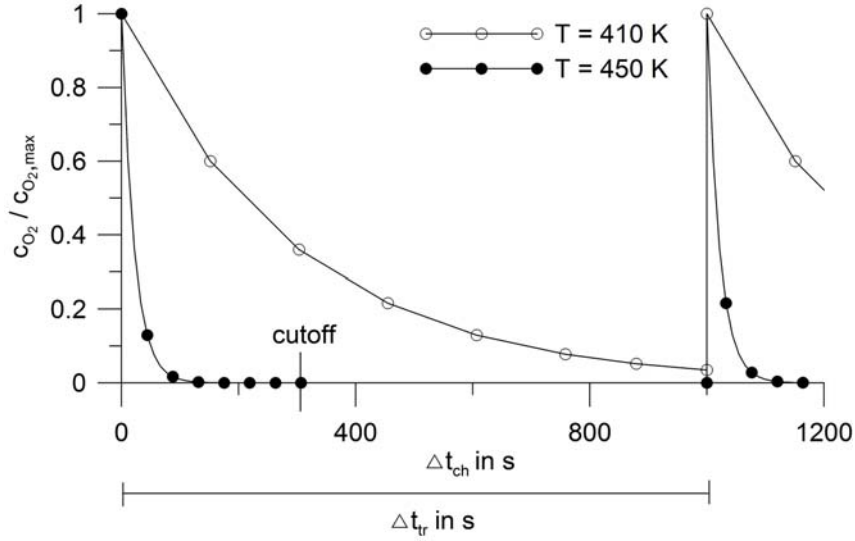


Figure 3.1 Illustration of the operator-splitting approach for two temperature values. $c_{O_2}/c_{O_2,max}$ is the normalized oxygen concentration, Δt_{tr} and Δt_{ch} are the time steps for which oxygen transport and oxygen consumption, respectively, are calculated. For $T = 450K$, the oxygen concentration becomes nearly zero after 300 seconds (the cutoff). From here on, the calculation of oxygen consumption stops.

The penetration depth depends on the time over which oxygen transport takes place, which is given by the transport time step, Δt_{tr} . The larger Δt_{tr} , the deeper will oxygen penetrate into the reactive region.

This fact poses an obstacle for the numerical simulation. Simulations performed with different constant time steps may result in different solutions due to the variable extent of the reactive region. Therefore, the extent is assumed to be predisposed. This is realized by keeping the macroscopic Representative Length ℓ (Sec. 2.2.3) constant, so that also a constant penetration depth of oxygen persists. Assuming the dominance of convective oxygen transport an estimation of ℓ is given by

$$\ell = |\mathbf{v}| \Delta t_{tr}. \quad (3.8)$$

To keep ℓ constant, an automatic time step determination is used according to

$$\Delta t_{tr} = \frac{\ell}{|\mathbf{v}_{max}|}, \quad (3.9)$$

where $|\mathbf{v}_{max}|$ is the maximum flow velocity within the combustion center. The influence of the penetration depth onto the dynamic fire propagation will be discussed by means of results from a sensitivity analysis (Sec. 4.3 below).

A typical time step development for a two-dimensional simulation as later explained in Sec. 3.5 is presented in Fig. 3.2. Initially, Δt_{tr} decreases due to the increase of the maximum flow velocity (cf. Eq. 3.9), which in turn is a result of the increasing combustion

temperature. In the long-term behavior the time step converges to a constant value, because the combustion temperature becomes more or less constant. The increasing time step at the beginning is due to the development of the combustion center, which initially shows a dynamic evolution in form of a small circle and thereafter reshapes into an elongated distribution at the bottom of the seam.

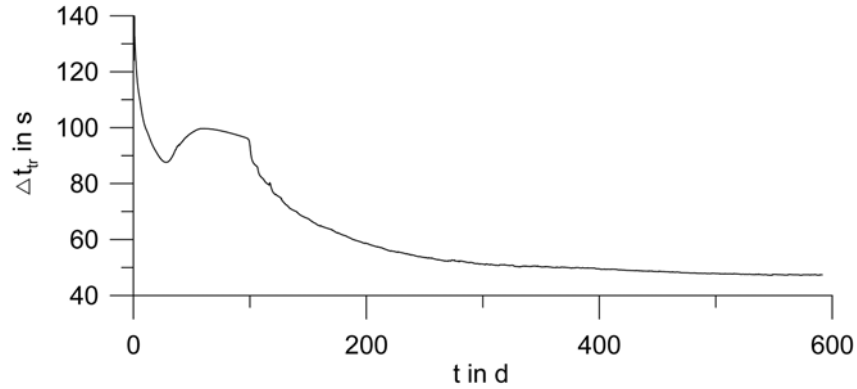


Figure 3.2 Temporal development of the time step size, Δt_{tr} , resulting from a simulation example in Sec. 3.5

Due to the need of using pre-defined time steps for the simulation of oxygen transport, numerical stability problems might arise when explicit time discretization is used for Eqs. 3.1 (Ferziger and Peric, 1999). Therefore, a fully implicit scheme has been used for the time discretization to avoid instable solutions.

Application of the above-presented approach has the advantage that the fire propagation rate can be controlled by the amount of oxygen being transported into the reactive region. This is realized by relating the amount of consumed fuel to the time over which oxygen is transported and not consumed. Hence, the fuel consumption rate, which is the measure for the fire propagation rate, is considered concerning Δt_{tr} :

$$Q_f = \frac{\Delta c_f^{\Delta t_{tr}}}{\Delta t_{tr}}. \quad (3.10)$$

Within Δt_{tr} , the consumption of oxygen takes place very fast, but has no influence on the fuel consumption rate.

Common direct approaches without using operator-splitting would be forced to relate the fuel consumption source according to the time step Δt_{ch} :

$$Q_f^* = \frac{\Delta c_f^{\Delta t_{ch}}}{\Delta t_{ch}}. \quad (3.11)$$

Finally, the energy source for the heat balance equation, Eq. 2.28, is calculated according to the fuel consumption occurring during Δt_{tr} :

$$Q_H = \Delta H Q_f = \Delta H \frac{\Delta c_f^{\Delta t_{tr}}}{\Delta t_{tr}}. \quad (3.12)$$

Herein $\Delta c_f^{\Delta t_{tr}}$ is the amount of fuel consumed during Δt_{tr} .

3.2.2 Extrapolation to Large Time Steps

Even smaller calculation times are obtainable through an extrapolation algorithm. The application of the algorithm is based on the assumption that the procedure of oxygen refill and subsequent oxygen consumption repeats over large simulation times without significantly changing the oxygen distribution. In that case, the rate of oxygen consumption in the combustion center can be assumed constant, which in turn denotes a constant rate of coal consumption. The assumption of constant oxygen distribution is valid as long as temporal temperature variations remain small and as long as the reactive region does not move significantly during a considered time interval.

Temperature variations have influence on the flow velocity and therefore also on the convective oxygen transport. Hence, if temperature variations take place fast, the amount of oxygen transport into the reactive region rapidly changes. This leads to a rapid change in the fuel consumption rate. However, the temperature of an underground coal fire remains rather constant over long times.

The reactive region moves whenever fuel is completely consumed within parts of that region. In that case, the combustion center moves further through the seam and consequently changes the oxygen distribution. Due to the large amount of fuel stored in a coal seam, the movement of the combustion center through the seam can be assumed to take place slowly. Temperature changes and changes in the fuel distribution are both slowly varying. Thus, the assumption of constant oxygen distribution is appropriate over relatively long time intervals.

For the extrapolation algorithm, a third time step, Δt_f , is introduced over which the rate of coal consumption remains constant (due to the constant oxygen distribution). The solution procedure including the extrapolation algorithm is given in Tab. 3.2. The fuel consumption rate, Q_f , is calculated according to the fuel consumption Δc_f during the time step Δt_{tr} (cf. Eq. 3.10):

$$Q_f = \frac{\Delta c_f^{\Delta t_{tr}}}{\Delta t_{tr}}. \quad (3.13)$$

With this consumption rate, the coal concentration is then calculated a time step Δt_f later:

$$\Delta c_f^{\Delta t_f} = Q_f \Delta t_f. \quad (3.14)$$

Likewise, the production of solid products is computed and the transport and release of heat are calculate over Δt_f . The energy source is determined by inserting the fuel consumption rate, Eq. 3.13, into Eq. 2.26. Finally, the hydraulic equation, Eq. 2.17, together with the

gas flow equation, Eq. 2.21, are solved over Δt_f . Conservation equations for oxygen and exhaust gas concentrations are not solved over Δt_f , because their concentrations remain constant.

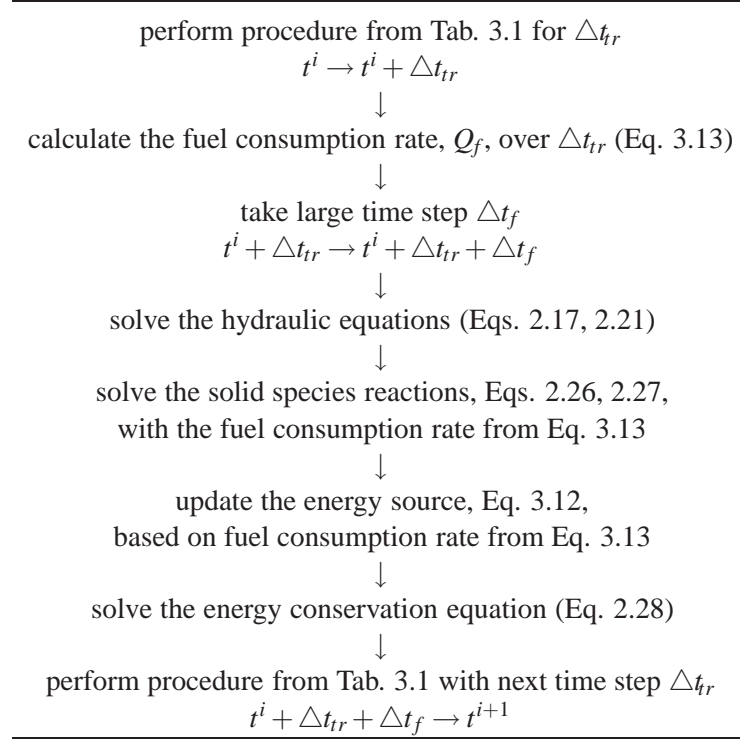


Table 3.2 Sequence of solving the set of equations over the time steps $t \rightarrow t^i + \Delta t_{tr} + \Delta t_f \rightarrow t^{i+1}$

A verification for the assumption of constant oxygen distribution over large time steps is presented in Fig. 3.3. The results have been obtained from a simulation example, which is presented below (Sec. 3.5). The diagram shows the maximum and the average differences in oxygen concentration between two consecutive time steps, i.e. after a simulation time over the transport time step $\Delta t_{tr} = 50s$ plus the extrapolation time step $\Delta t_f = 100 \Delta t_{tr}$. The maximum is calculated according to

$$\Delta c_{O_2, max} = \max \left(|c_{O_2}^{i+1} - c_{O_2}^i| \right), \quad (3.15)$$

where the time step size between t^{i+1} and t^i is $\Delta t_{tr} + \Delta t_f$. An average difference is determined as

$$\Delta \bar{c}_{O_2} = \frac{1}{m} \sum_m |c_{O_2}^{i+1} - c_{O_2}^i|, \quad \forall m \quad \text{where} \quad |c_{O_2}^{i+1} - c_{O_2}^i| > 10^{-4}. \quad (3.16)$$

m is the number of nodes where the difference in oxygen concentration between two consecutive time steps, $|c_{O_2}^{i+1} - c_{O_2}^i|$, is larger than 10^{-4} . This constraint has been used to

exclude nodes away from the combustion center, where the oxygen concentration is not affected by any process.

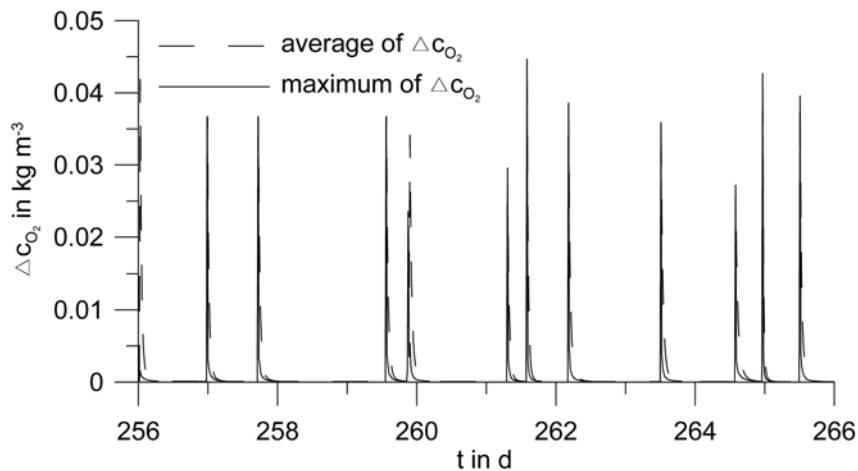


Figure 3.3 Maximum and average difference in oxygen concentration, defined as $\Delta c_{O_2} = c_{O_2}^{t^{i+1}} - c_{O_2}^i$, where $t^{i+1} - t^i = \Delta t_{tr} + \Delta t_f$

Fig. 3.3 shows that Δc_{O_2} is close to zero except for some discrete times. Here, the fire moves further through the grid, so that the oxygen distribution changes. However, the difference in oxygen concentration remains small even at these situations.

Finally, Tab. 3.3 presents the results from the investigation of the size of Δt_f . For the investigation, simulations were performed over 11 days of simulation time with time steps Δt_f of different size. The transport time step remained constant ($\Delta t_r = 50 s$). The difference in maximum temperature, ΔT_{max} , has been used to quantify the comparison between simulations with and without the additional calculation over the extrapolation time step Δt_f . The entries show that the difference ΔT_{max} increases with increasing extrapolation time step. However, the difference in maximum temperature becomes significant only when Δt_f is at least 100 times larger than Δt_r .

Δt_f in s	500	1000	1500	5000
ΔT_{max} in K	0.12	0.26	1.45	4.11

Table 3.3 Simulation results to investigate the difference in maximum temperature, defined as $\Delta T_{max} = |T_{max}(\Delta t_f) - T_{max}(\Delta t_r)|$, after 11 days of simulation time. $T_{max}(\Delta t_r)$ is the maximum temperature obtained without the extrapolation algorithm, $T_{max}(\Delta t_f)$ is the maximum temperature obtained from the calculation according to the procedure from Tab. 3.2.

3.2.3 Remarks to the Numerical Approach

The main progress by obtaining larger time steps through the operator-splitting approach lies in the fact that the time-consuming numerical solution of the transport equations (Eqs. 3.3) is performed for Δt_{tr} instead of Δt_{ch} . The progress is obtained because the time-consuming factor for finite-element discretization methods is given by the assembly of element matrices to discretize spatial derivations. For the present simulations the duration for assembling the matrices of species transport was 20 times larger than the time needed to solve the global algebraic system of equations.

For the nodewise time integration to calculate the chemical consumption or production (Eqs. 3.4) over Δt_{ch} , very short calculation times are obtained, because finite-difference time integrations are not very time consuming.

The introduction of a third time scale at which the oxygen distribution is constant makes the application of an extrapolation algorithm possible. The algorithm enables the simulation of underground coal fire propagation in time steps of 1000s or even more, so that the example simulations (Sec. 3.5) of a one-year burning coal fire took 53h calculation time with a common single-processor machine (2.8 GHz CPU frequency).

Concluding, the presented numerical procedure makes use of the fact that, at different time scales, different processes exhibit different dynamic behavior or have different influence on the dynamic development of the overall system. Therefore, further investigations of the temporal behavior and the influence of the involved processes is of special importance to find possibilities to simplify the numerical simulation.

3.3 Numerical Solution of the Forchheimer Equation

One additionally implemented algorithm is a solver for the Forchheimer equation (Eq. 2.21)

$$\nabla P - \rho^f(T)\mathbf{g} = -\frac{\mu}{k_{ij}}\mathbf{q} - \frac{c_F}{\sqrt{k_{ij}}}\rho^f|\mathbf{q}|\mathbf{q}. \quad (3.17)$$

Eq. 3.17 represents a nonlinear set of equations, wherein the equations are coupled through the Euclidian norm

$$|\mathbf{q}| = \sqrt{\sum q_i^2}. \quad (3.18)$$

Assuming isotropy ($k_{ij} = k$), the Forchheimer equation reads after re-arrangements in component notation (three-dimensional):

$$f_x: = \frac{\partial P}{\partial x} + \frac{\mu}{k}q_x + \frac{c_F}{\sqrt{k}}\rho^f\sqrt{q_x^2 + q_y^2 + q_z^2}q_x = 0 \quad (3.19)$$

$$f_y: = \frac{\partial P}{\partial y} + \frac{\mu}{k}q_y + \frac{c_F}{\sqrt{k}}\rho^f\sqrt{q_x^2 + q_y^2 + q_z^2}q_y = 0 \quad (3.20)$$

$$f_z: = \frac{\partial P}{\partial z} - \rho^fg_z + \frac{\mu}{k}q_z + \frac{c_F}{\sqrt{k}}\rho^f\sqrt{q_x^2 + q_y^2 + q_z^2}q_z = 0. \quad (3.21)$$

$(q_x, q_y, q_z) = \mathbf{q}$ are the components of the specific flow rate vector and g_z is the gravitational acceleration in z direction. This set of equations represents a typical problem where N

functional relations have to be zeroed:

$$\mathbf{f}(\mathbf{q}) = 0. \quad (3.22)$$

The set of equations (Eqs. 3.22) has to be solved numerically, because analytical solutions do not exist due to the coupling. The set consists of not more than three equations (for three-dimensional problems), and is also a rather simple function. The derivatives of the functions \mathbf{f} can easily be calculated, so that a Newton-Raphson method to solve the nonlinearly coupled system is useful.

The Newton-Raphson algorithm is based on the expansion of each of the functions \mathbf{f} into a Taylor series in the neighborhood of $\delta\mathbf{q}$ (Press et al., 1992):

$$f_i(\mathbf{q} + \delta\mathbf{q}) = f_i(\delta\mathbf{q}) + \sum_j \frac{\partial f_i}{\partial x_j}(\delta q_j) + O(\delta\mathbf{q}^2). \quad (3.23)$$

In Eq. 3.23,

$$\frac{\partial f_i}{\partial x_j} \equiv \mathbf{J} \quad (3.24)$$

is the Jacobian matrix. By neglecting terms of order $\delta\mathbf{q}^2$ and higher and by setting $\mathbf{f}(\mathbf{q} + \delta\mathbf{q}) = 0$, a set of linear equations is obtained for the corrections $\delta\mathbf{q}$ that move each function closer to zero:

$$\delta\mathbf{q} = -\mathbf{J}^{-1}\mathbf{f}. \quad (3.25)$$

Equation 3.25 is easily solved by the determination of \mathbf{J}^{-1} and subsequent multiplication with \mathbf{f} , so that Eq. 3.25 can be calculated. The corrections are then added to the solution vector:

$$\mathbf{q}_{new} = \mathbf{q}_{old} + \delta\mathbf{q}. \quad (3.26)$$

The described process is iterated to convergence, where the relative error

$$\varepsilon_r \geq \left| \frac{\mathbf{q}_{new} - \mathbf{q}_{old}}{\mathbf{q}_{new}} \right|, \quad \varepsilon_r > 0, \quad \varepsilon_r \in \Re \quad (3.27)$$

has been used as the termination criterion (Engeln-Muelliges and Reutter, 1996). More sophisticated Newton algorithms like the damped form (Engeln-Muelliges and Reutter, 1996, p. 146) showed no improvements in the computation performance.

3.4 Code Verification

Software packages that have been implemented in addition to the existing code by Thorenz (2001) were verified by comparison with analytic solutions or by benchmark comparison with the finite-element software COMSOL Multiphysics².

The term verification is here referred to as proving that an implemented software package or algorithm is running correctly (Konikow and Bredehoeft, 1992). Model validation and

²Femlab GmbH, Göttingen, Germany

calibration are not included in this section, but will be discussed later.

In the following verification results are exemplarily presented for the Forchheimer equation (Eq. 2.21), the chemical conversion of reactive educts into products (Eqs. 3.4, 3.5) and the source term (Eq. 3.12) for the energy balance equation (Eq. 2.28), which considers the generation of heat. A further verification is presented for the hydraulic equation, Eq. 2.17, because this equation needs to consider compressible gas flow, whereas compressibility stems from the temperature dependency of the fluid density. Finally, the mass flux has been integrated over the domain of a two-dimensional simulation example. Because, in the considered model, gas mass is neither destroyed nor produced, the integrated mass flux should be zero.

3.4.1 Verification of the Forchheimer Equation

The verification for the solver of Eq. 2.21 was performed by two-dimensional test simulations, whereas fluid flow takes place in one direction. Due to the one-dimensional flow, the simulation results can be compared with a one-dimensional analytic solution, Eq. A.5, which is derived in App. A.

Results are summarized in Tab. 3.4 for two different permeabilities. The permeabilities chosen are relatively high, so that the nonlinear dependency between pressure differences and the specific flow rate becomes relevant. Values within the table show that at most six iterations are needed until the convergence criterion (Eq. 3.27) is fulfilled.

$\Delta P/\Delta x$ (Pa/m)	$k = 10^{-6} m^2$		$k = 10^{-7} m^2$	
	$\#Iterations$ (-)	ϵ_r (-)	$\#Iterations$ (-)	ϵ_r (-)
10	5	8.06×10^{-4}	3	1.36×10^{-4}
20	6	2.8×10^{-5}	4	1.0×10^{-6}
30	6	2.19×10^{-4}	4	1.1×10^{-5}
40	6	7.42×10^{-4}	4	5.1×10^{-5}
50	7	1.0×10^{-6}	4	1.48×10^{-4}

Table 3.4 Results for the investigation of the Newton-Raphson algorithm, demonstrated by the number of iterations and relative error (Eq. 3.27) for different pressure differences, $\Delta P/\Delta x$ and different permeabilities k

Fig. 3.4 graphically presents a comparison between the analytic solution (Eq. A.5, App. A) and the numerical simulation for two permeabilities. The comparison shows good agreement between simulation results and the analytical solution.

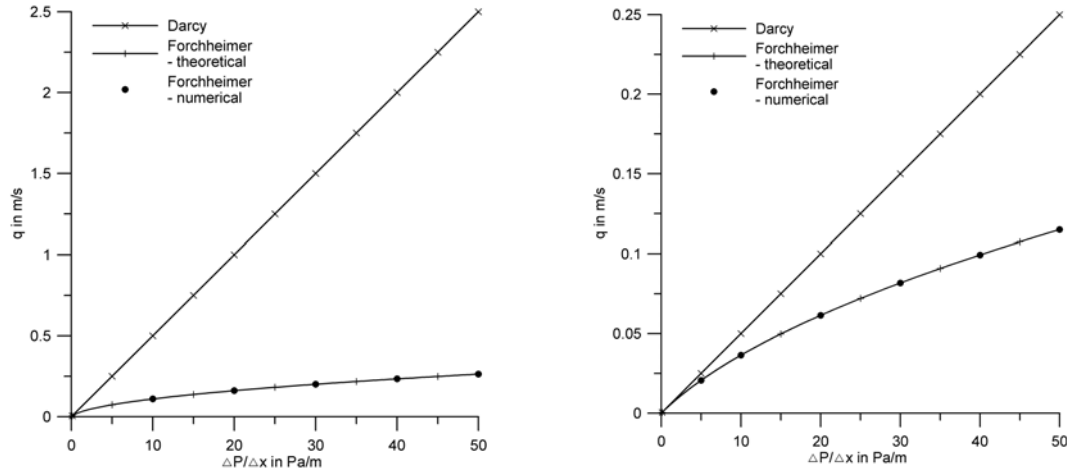


Figure 3.4 Comparison between analytic and numerical solution of the Forchheimer equation, Eq. 2.21, for $k = 10^{-6} m^2$ (left) and $k = 10^{-7} m^2$ (right). For illustration of nonlinear effects, the linear Darcy law (Eq.2.20) is also shown.

3.4.2 Consumption/Production of Chemical Species and Heat

A verification for the numerical solution of heat generation is based on Eq. 2.28, where transportation terms are omitted:

$$c^b \frac{\partial T}{\partial t} = Q_H. \quad (3.28)$$

The heat production source is obtained from Eqs. 2.26 and 2.29:

$$Q_H = -\Delta H Q_f = \Delta H c_f c_{O_2} k_0 e^{-\frac{E}{RT}}. \quad (3.29)$$

Assuming constant oxygen and fuel concentrations, $c_f = const.$, $c_{O_2} = const.$, the heat source term depends on the temperature only: $Q_H = Q_H(T)$. Hence, Eq. 3.28 can be integrated to obtain an analytical solution:

$$T(t) = T_0 + \frac{Q_H}{c^b} t. \quad (3.30)$$

The analytic solution describes a system that is heating up by a heat generating source.

Likewise, the approach to numerically solve the consumption of reaction educts and the production of reaction products according to Eqs. 3.4 and 3.5 is verified against the analytical solution, where the source term is assumed to depend on the considered variable, only. E.g., the consumption of fuel is expressed as:

$$\frac{\partial c_f}{\partial t} = Q_f = -c_f c_{O_2} k_0 e^{-\frac{E}{RT}}, \quad (3.31)$$

wherein c_{O_2} and T are held constant, and the corresponding analytical solution is:

$$c_f(t) = c_{f,0} - Q_f t. \quad (3.32)$$

A comparison between the analytical solutions from above (Eqs. 3.30 and 3.32) and simulation results is presented in Fig. 3.5. These verification examples, as well as verifications for the other chemical species (not presented here) show good agreement.

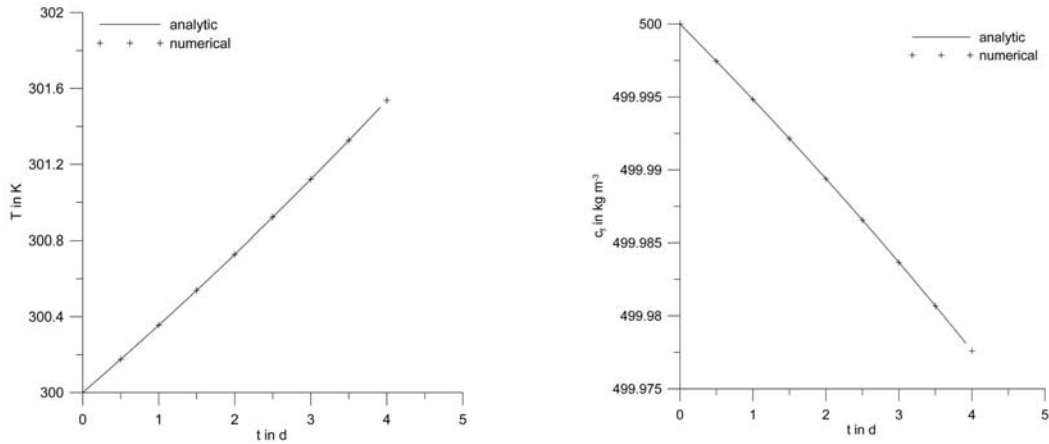


Figure 3.5 Comparison of the temperature development (left) and the coal consumption (right) between analytic and numerical solutions

3.4.3 Solution of the Hydraulic Equation

The hydraulic equation, Eq. 2.17, has been derived from the mass balance equation for an ideal gas and includes the gas density as a function of temperature.

This functionality is needed to consider thermal buoyancy as the driving force for fluid motions. One frequently applied simplification is the Boussinesq-Approximation (e.g. Tritton, 1970; Dirsch, 1998; Holzbecher, 1998; Kolditz et al., 1998), where the density is assumed to be constant except in the term expressing thermal buoyancy. The approximation is not valid for underground coal fires, because large density variations have to be expected due to the large temperature range the gas is exposed to (see Fig. 2.4). However, the density is nearly independent of pressure variations, hence previous studies by Evans and Raffensperger (1992) or De Ville (1996) are not relevant here.

A verification of the hydraulic equation has been performed by comparison between simulation results obtained from Rockflow and the commercial finite-element simulator COMSOL Multiphysics. The simulation is performed under the steady-state assumption, hence the mass balance including density variations is expressed by Eq. 2.15:

$$\nabla \cdot \mathbf{j}_m = \nabla \cdot (\rho^f \mathbf{q}) = \rho^f \nabla \cdot \mathbf{q} + \mathbf{q} \cdot \nabla \rho^f = 0. \quad (3.33)$$

The temperature-dependent fluid density is used according to Eq. 2.19. For \mathbf{q} (the specific flow rate) Darcy's law (Eq. 2.20) is assumed. The one-dimensional form of Eq. 3.33 has been solved based on the setup presented at the left hand side of Fig. 3.6. The setup applies in z -direction, hence thermal buoyancy acts. The temperature distribution is assumed to

be linear, so that the fluid density distribution according to the blue line in Fig. 3.6 a) is obtained.

In Fig. 3.6 a) the pressure is kept zero at the top. At the bottom boundary a no flow condition is assumed. Consequently, a hydrostatic pressure distribution according to

$$P_{hyd} = g \int_{z=10m}^{z=0m} \rho^f(z) dz \quad (3.34)$$

is obtained as presented in the figure, with a magnitude of $60 Pa$ at the bottom. The pressure distribution is described by a non-linear function, as a result of temperature dependent density variations. With the considered setup, gas flow does not set in, because there is no driving force.

In Fig. 3.6 b) Dirichlet boundary conditions are presumed at both bounds, resulting in a pressure distribution which is superimposed to the hydrostatic pressure from Fig. 3.6 a). In contrast to Fig. 3.6 a) gas flow sets in, due to the externally imposed pressure gradient. Magnitudes for the specific flow rate range between $1 \times 10^{-5} m s^{-1}$ and $4 \times 10^{-5} m s^{-1}$. The specific flow rate is not constant, hence the continuity assumption ($\nabla \bullet \mathbf{q} = 0$) obtained from the Boussinesq-Approximation is not valid here. Instead, the mass flux ($\mathbf{j}_m = \rho^f \mathbf{q}$, cf. Eq. 2.11) must to be constant, as described by Eq. 3.33. This fact is well reproduced by the simulation, where $\mathbf{j}_m = 1.215 kg m^{-2} s^{-2}$ has been obtained (Fig. 3.6 b). Because mass is neither destroyed nor produced, mass entering the domain also leaves it. Therefore, the sum over all mass fluxes becomes zero.

The mass flux calculation has also been investigated by means of the two-dimensional simulation example in the next section (Sec. 3.5). For the verification, the mass flux has been integrated over the whole calculation domain, including the interior and the boundaries. From the integration, a value of $j_m = 9.03 \times 10^{-6} kg m^{-2} s^{-1}$ has been calculated, which can be considered as sufficiently close to zero.

Fig. 3.7 presents simulation results for the one-dimensional mass balance equation, but in the horizontal direction. Hence, thermal buoyancy is excluded. The pressure is kept constant at the bounds, hence a pressure gradient is obtained. The pressure obeys is a non-linear distribution due to the (non-linear) temperature dependent density distribution. This non-linearity proves that the mass balance is solved for compressible gas flow. If incompressibility would hold, the pressure distribution would become linear.

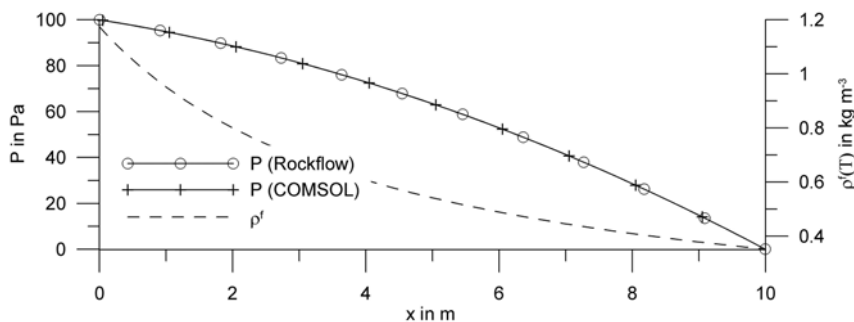


Figure 3.7 Comparison of the pressure drop between Rockflow and COMSOL Multiphysics simulations without thermal buoyancy. The density is $\rho^f(T) = \rho_0 \frac{T_0}{T}$, for which a linear temperature profile from $T = 300\text{ K}$ (at $x = 0\text{ m}$) to $T = 1000\text{ K}$ (at $x = 10\text{ m}$) is assumed.

3.5 Simulation Example

In the following the application of the numerical approach is illustrated by a two-dimensional simulation example of the underground coal fire propagation.

3.5.1 Setup

The two-dimensional model for the simulation is given in Fig. 3.8. It assumes one coal seam cropping out under a scarp. The seam is embedded in a geologic formation. Gridding has been performed with GINA (Kunz, 2005), with local grid refinement in the coal seam to avoid numerical oscillations. The grid is made up of 7841 elements and 7980 nodes, with six degrees of freedom at each node.

This model is used throughout the thesis, hence the simulations have been performed within a two-dimensional domain. The model can be regarded as a slice of a three-dimensional body whose extent and structure is equal to the slice in the lateral direction. Hence, the application of this model presumes irrelevant processes in the lateral direction. This assumption likely loses validity when a detailed simulation of a specific fire site is addressed, due to the three-dimensional nature of the processes. However, this thesis approaches the investigation of principle phenomena, for which a two-dimensional setup is sufficient.

In Rockflow a third dimension is realized for such two-dimensional slices by specifying a 'slice thickness'. The governing balance equations are then integrated over this thickness to obtain three-dimensional physical quantities from actually two-dimensional simulations (see Kolditz, 1996, for mathematical formulations). This method has been implemented for simulations based on hybrid modeling approaches, where two-dimensional discrete fractures are embedded in three-dimensional domains. For the discrete fractures, the third dimension is considered by the integration over the fracture aperture.

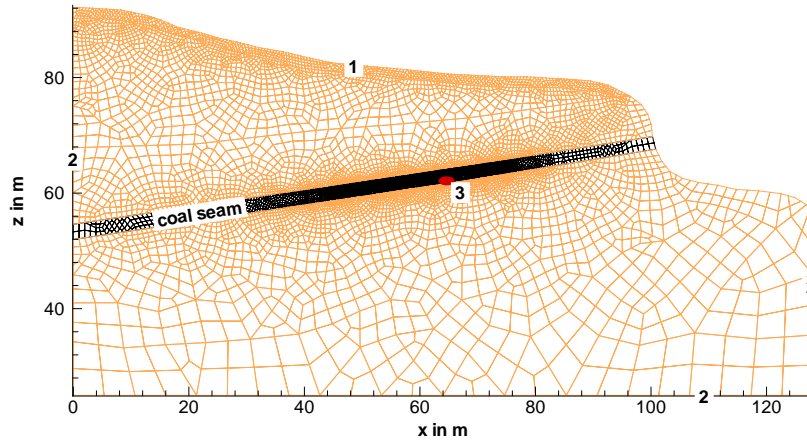


Figure 3.8 Setup for example simulations. Boundary conditions were set as follows. At boundary 1, constrained boundary conditions apply for the temperature and the fluidal species concentrations, depending on the direction of gas flow. If gas gets out of the surface, Neumann boundary conditions apply. When gas enters the subsurface, Dirichlét boundary conditions apply, with values $T = 300K$, $c_{O_2} = 0.297kgm^{-3}$, and $c_{eg} = 0kgm^{-3}$. For the pressure, Dirichlét boundary conditions apply according to a hydrostatic distribution. At boundary 2, Neumann boundary conditions apply for all variables. At location 3, an initial combustion center is assumed, with $T = 500K$.

For this work the slice thickness is assumed to be one meter, so that subsequently given physical units express quantities per meter (m^{-1}). E.g., a flow rate Q expressing the injection of fluid into a system is given in units of cubic meters per second per meter slice thickness: $m^3 s^{-1} m^{-1}$.

Initial and Boundary Conditions

The initial pressure is assumed to obey a hydrostatic distribution according to

$$P(z) = P_0(z_0) + \rho_0^f(T_0)\mathbf{g}\Delta z, \quad (3.35)$$

with $\Delta z = (z_0 - z)$, $P_0(z_0) = 101325 Pa$ at $z_0 = 96m$, $\rho_0^f(T_0 = 300K) = 1.27kgm^{-3}$, and $\mathbf{g} = 9.81ms^{-2}$, acting in z -direction. The boundary conditions for P are assumed to be no-flow (Neumann type) for boundaries 2, and constant pressure values (Dirichlét type) for boundary 1. Pressure values were set according to the distribution from Eq. 3.35.

Initial conditions for oxygen are set to the oxygen and exhaust gas concentrations of environmental air: $c_{O_2,0} = 0.297kgm^{-3}$ and $c_{eg,0} = 0kgm^{-3}$. Boundary conditions for c_{O_2} and c_{eg} were also set of no-flow type at boundaries 2. At the surface (boundary 1), constrained boundary conditions are used (cf. Sec. 2.2.4), depending on the direction of gas flow. In case of gas inflow, gas contains the oxygen and exhaust gas concentrations of the environmental air. In contrast, oxygen and exhaust gas concentrations in gas leaving the surface are a result of previous propagation paths through the subsurface. E.g., gas leaving the surface

exhibits zero oxygen concentration after having passed the combustion center. In that case, the boundary conditions are set to free-convective-outflow boundary conditions.

For temperature the same constrained boundary conditions apply as for the reactive fluid components. In case of inflowing gas, the temperature value is set to $T = 300\text{ K}$ (Dirichlet). Initial temperature is also $T = 300\text{ K}$ everywhere, except within the initial combustion center, where $T = 500\text{ K}$ holds. Initial conditions for fuel and solid products were set to $c_{f,0} = 850\text{ kg m}^{-3}$ and $c_{sp,0} = 0\text{ kg m}^{-3}$, respectively.

Parameters

Parameters used for the simulation are summarized in Tab. 3.5. Tables 2.1 and 2.2 give reaction kinetic parameters. Isotropy is assumed, as well as a homogeneous distribution of the parameters. No distinction is made between the coal seam and adjacent rocks, unless explicitly specified. The reference thermal conductivity λ_0 (cf. Eq. 2.35) is a result of laboratory measurements of samples from Chinese coal (Schmidt et al., 2005) and rock samples (Wessling and Kessels, 2005a) from the Wuda coal mining area. The constant storativity as defined in Eq. 2.18 can be estimated from the pressure-dependent density formulation, $\rho^f(P) = \rho_0^f P/P_0$, so that $\partial\rho^f/\partial P \sim 10^{-5}$ and $S \sim 10^{-6}\text{ Pa}^{-1}$, when $\Phi \sim 0.1$. The dimensionless form-drag constant (cf. Eq. 2.21) is $c_F = 0.5$. The molecular diffusion coefficient is taken from Massmann and Farrier (1992), and the heat capacities stem from Schmidt et al. (2005) for coal and Cermak and Rybach (1982) for rock.

Description	Parameter	Value	Unit
Bulk heat capacity of coal, rock	c^b	$5.57 \times 10^5, 1.92 \times 10^6$	$\text{J m}^{-3} \text{K}^{-1}$
Form-drag constant	c_F	0.5	—
Specific heat capacity of fluid	c_p^f	1000	$\text{J kg}^{-1} \text{K}^{-1}$
Molecular diffusion coefficient	D_{mol}	10^{-6}	$\text{m}^2 \text{s}^{-1}$
Permeability	k	10^{-9}	m^2
Storativity	S	10^{-6}	Pa^{-1}
Length of oxygen drop	ℓ	0.05	m
Longitudinal, transversal dispersion lengths	α_l, α_t	0.5, 0.1	m
Constant for radiation	β	7×10^{-9}	$\text{W m}^{-1} \text{K}^{-4}$
Thermal conductivity of coal, rock	λ_0	0.1, 2.0	$\text{W m}^{-1} \text{K}^{-1}$
Fluid viscosity	μ	1.81×10^{-5}	Pa s
Porosity of coal, rock	Φ	0.4, 0.2	—

Table 3.5 Thermal and hydraulic parameters for the example simulation

3.5.2 Simulation Results

Fig. 3.9 shows the distributions of exhaust gas and oxygen, which build up due to the underground combustion, i.e. the consumption of oxygen and the production of exhaust gas. The extent of the unburnt coal seam (bottom figure) is marked by the black isolines giving the coal concentration $c_f = 850 \text{ kg m}^{-3}$ (which is the initial value). The streamlines show the direction of gas motions. A cloud develops in the adjacent beds with zero oxygen and maximum exhaust gas concentration, according to the stoichiometry from Eq. 2.7.

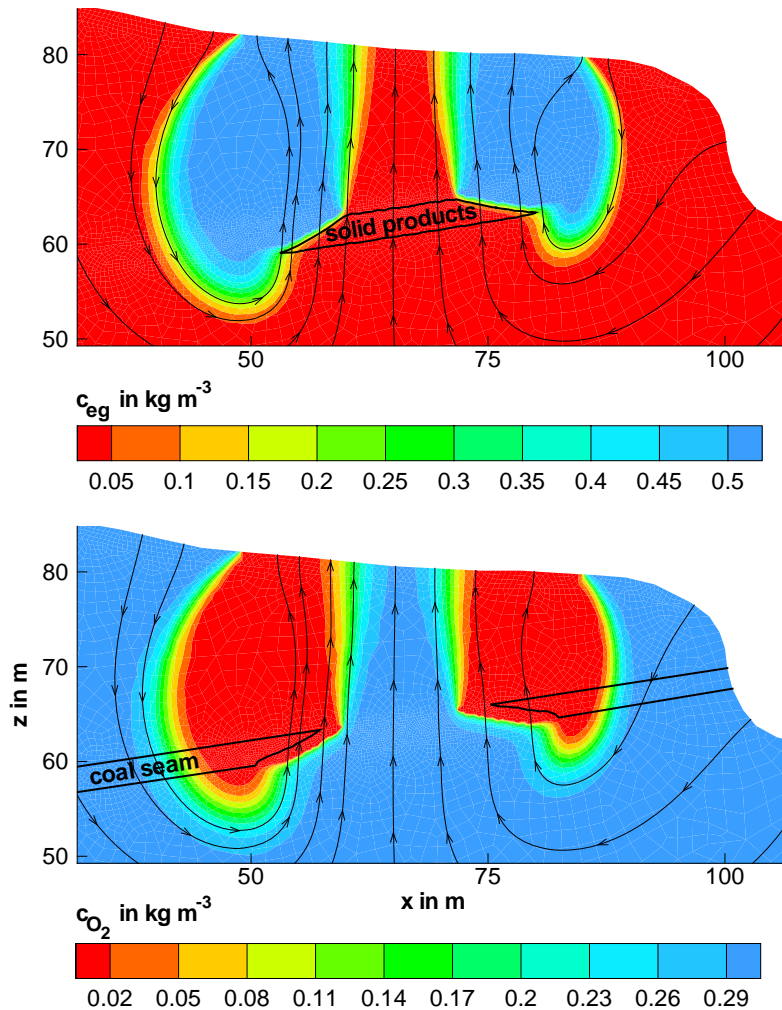


Figure 3.9 Distribution of the exhaust gas c_{eg} (top) and the oxygen concentration c_{O_2} (bottom) after 242 days of simulation time. Black isolines mark the concentration of solid products, $c_{sp} = 380 \text{ kg m}^{-3}$ (top), and the initial coal concentration, $c_{f,0} = 850 \text{ kg m}^{-3}$ (bottom). Streamlines marked with arrows give the direction of gas flow.

Fig. 3.10 presents the simulated fire propagation for three consecutive times, and the re-

sulting temperature distribution. The underground coal fire penetrates in the up- and downward direction through the seam. A maximum temperature of 1309K is reached by the upward moving fire, whereas the downward moving one exhibits lower values. The temperature remains rather constant even after 591 days.

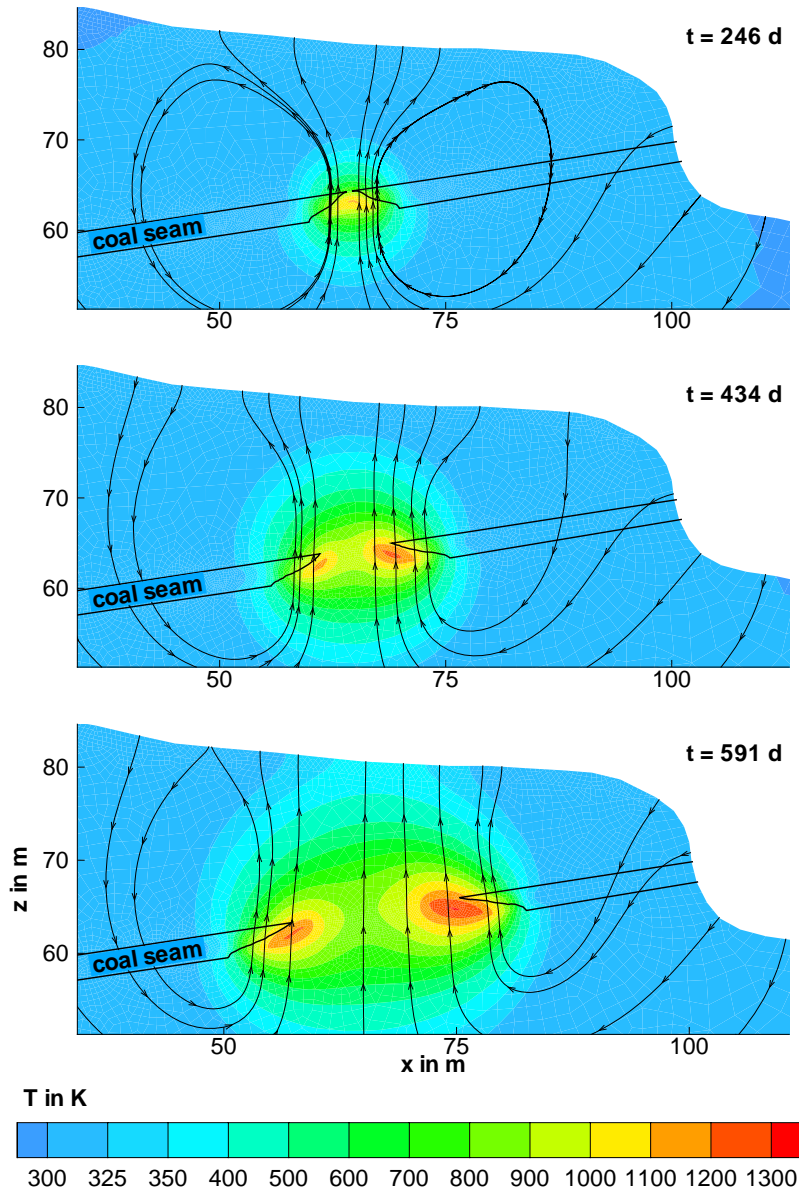


Figure 3.10 Temperature distribution due to the underground coal fire at three different times (note the unevenly scaled levels at low temperature). Black isolines mark the initial coal concentration, $c_{f,0} = 850\text{kgm}^{-3}$. Streamlines marked with arrows give the direction of gas flow.

The temporal development of the maximum combustion temperature is presented in Fig. 3.11. It first increases and then shows a valley-shaped trend. This trend results from the dynamic development of the combustion center, which first appears as a point-wise geometry and thereafter becomes elongated. Finally, the elongated shape breaks down into two combustion centers that move in the up- and downward directions through the seam.

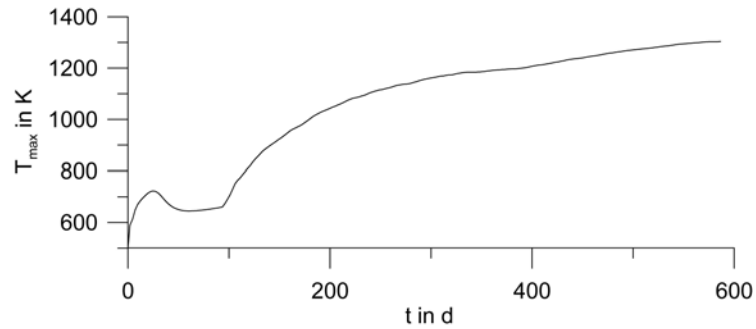


Figure 3.11 Dynamic development of the maximum combustion temperature

Of practical relevance are simulated magnitudes of physical variables at the surface of the domain. These values can be compared with *in-situ* measurements obtained at real coal fire sites. One such variable is the specific flow rate. A distribution of the simulated absolute value of the specific flow rate is presented in Fig. 3.12. The flow rate is largest where the combustion temperatures are highest, i.e. in the up- and downward moving combustion centers. At the surface a magnitude of $q = 0.7 \text{ m h}^{-1}$ is obtained.

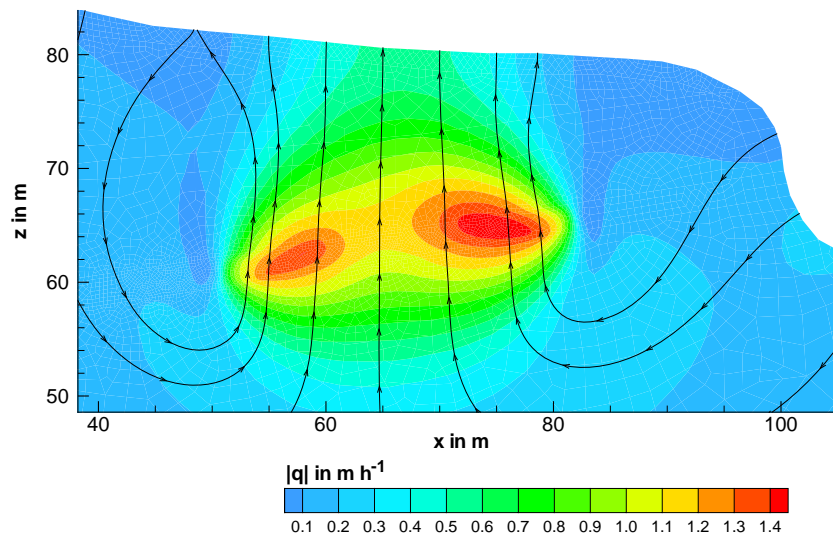


Figure 3.12 Distribution of the specific flow rate, given by its absolute value, $|q|$, after a simulation time of 591 days

Finally, a discussion of the energy balance in the underground coal fire system is of practical interest. Once the energy release is known, the amount of consumed fuel can be estimated according to the heating value of coal and the relation from Eq. 2.29.

The energy release becomes observable when the temperature at the surface increases in comparison to the ambient temperature. An extraction of released energy in the seam from surface measurements only implicates two difficulties.

First, the surface temperature results from an energy balance between the energy flux from the coal seam and the net energy flux from the near-surface including an exchange with the atmosphere (e.g. solar radiation). Hence, the net energy flux needs to be subtracted from the total one to obtain the energy flux from the burning coal seam only. Second, heat released by the combustion does not necessarily reach the surface. This aspect originates from the different time scales at which the transport mechanisms for thermal energy, convection and conduction, take place.

Convective transport is driven by thermal buoyancy and thus rapidly occurs once a combustion center has formed. Accordingly, an increased gas temperature is observable whenever the exhaust gas escapes through the surface. Of course, the gas temperature needs to retain its temperature during its flow through the system. This is likely the case in large-scale fractures, where an exchange of thermal energy between gas and rock is constrained to the fracture surfaces.

Heat conduction as a slow mechanism primarily heats up the rock around the combustion center. An increased temperature of the rocks at the surface will, if at all, set in late. A temperature anomaly at the surface resulting from heat conduction depends on the distance to the combustion center and on the propagation rate of the fire. For fast and deep fires, the energy release by the combustion is either too far away from the surface (deep fires) or too short (fast fires) as being able to cause temperature anomalies at the surface. Conduction will therefore only cause temperature anomalies if the fire is slowly propagating and at sufficiently shallow depth.

The slow-going mechanism of heat conduction can be demonstrated by the thermal relaxation time (Vogel, 1997):

$$\tau_{th} = \frac{c^b \ell^2}{\lambda}, \quad (3.36)$$

where λ is the heat conductivity, c^b is the bulk heat capacity and ℓ is a characteristic length. With $\lambda = 2 \text{ W m}^{-1} \text{ K}^{-1}$ for rock and $c^b = 1.92 \times 10^6 \text{ J m}^{-3} \text{ K}^{-1}$ (cf. Tab. 3.5), τ_{th} is in the order of three years. Heat conduction would thus require three years to transport heat from a ten meter deep coal fire ($\ell = 10 \text{ m}$) to the surface.

The energy flux (Eq. 2.30) has been calculated from the simulation example (Fig. 3.13). The contour plot shows the temperature distribution after a simulation time of 585 days. The red graph (top figure) presents the surface temperature, which is increased compared to the ambient temperature of 300 K . For the energy flux \dot{j}_h , three profiles are presented for the values below and above the coal seam, and just below the surface. \dot{j}_h is of similar magnitude below and above the seam. Hence, heat is not only released towards the surface, but also down into the rock. Of course, this downward moving heat will not be observable from surface measurements. An additional result is that the total energy flux through the

surface is much smaller than the sum of values below and above the seam (Tab. 3.6).

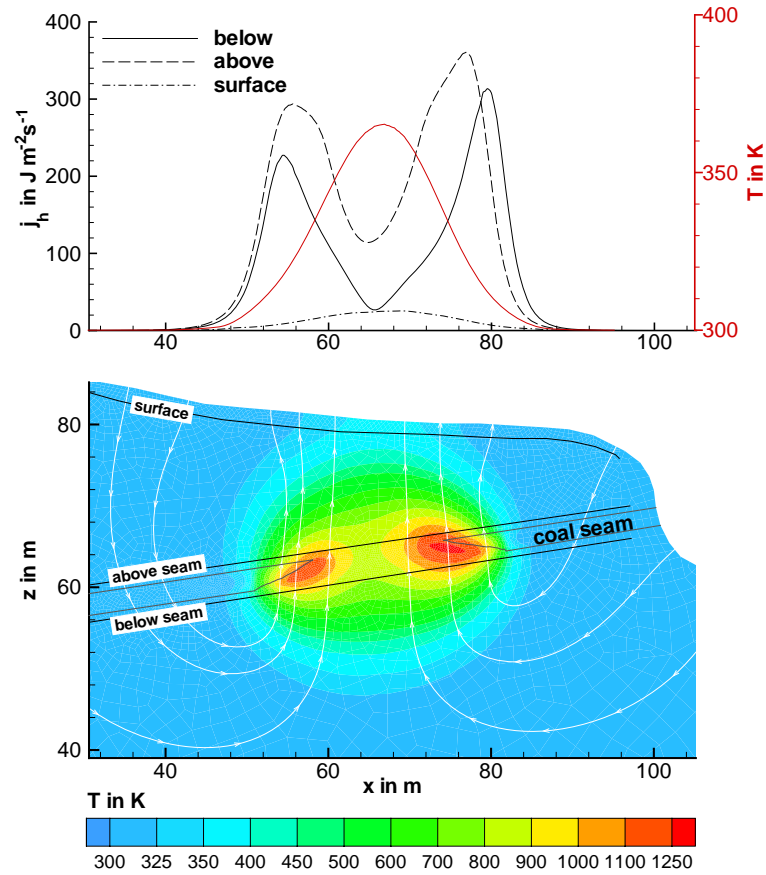


Figure 3.13 Simulation results after a simulation time of 585 days. Bottom: Temperature distribution due to the coal fire. White streamlines mark the flow direction of gas. Top: Energy flux j_h in $J m^{-2} s^{-1}$ below and above the coal seam, as well as just below the surface. The red graph gives the surface temperature.

	below surface	above seam	below seam
Polyline length in m	82	79	79
Integrated energy flux in $J s^{-1}$	5.25×10^2	1.07×10^4	6.24×10^3

Table 3.6 Total energy flux integrated along the profiles as presented in Fig. 3.13 (note that the setup is assumed to be one meter thick in the third dimension, hence the area through which energy flux takes place is calculated by the polyline length times the slice thickness of one meter).

Another aspect that should be discussed is the temporal development of the energy release. Fig. 3.14 shows the temporal development of the amount of consumed coal, the resulting energy release according to Eq. 2.29 and the integrated energy flux through the surface. The flux through the surface increases after 270 days of simulation time, which is delayed in comparison to the energy release from the coal combustion.

These simulation results demonstrate that temperature or heat flux measurements at the surface can underestimate the total amount of released energy and hence underestimate the total amount of consumed coal.

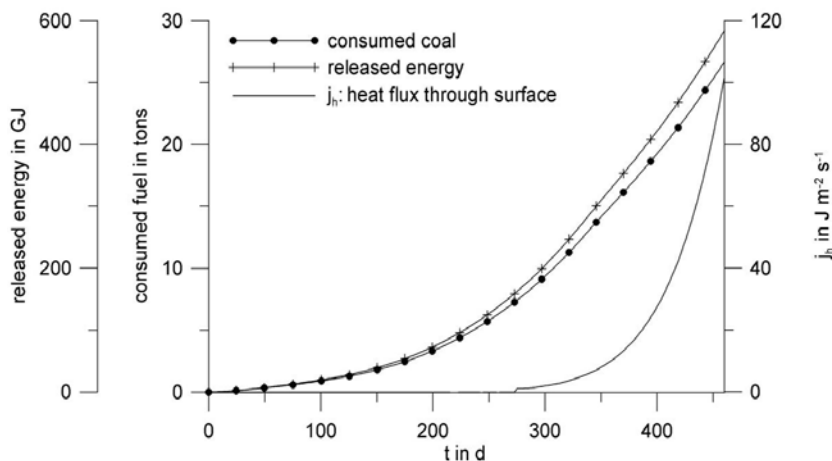


Figure 3.14 Cumulative energy release, coal consumption and energy flux, j_h , through the surface

3.5.3 Definition of the Propagation Rate

The fire propagation rate will be used throughout this work as a quantity that can be obtained from simulation results. This quantity will be used to characterize the underground coal fire. Due to the setup (cf. Fig. 3.8), the fire propagation rate is likely not constant. Rather, the distance between the atmospheric oxygen reservoir and the combustion center in the seam permanently changes due to the declination of the seam and the uneven topography. Hence, a dynamic development of the fire propagation rate has to be expected. Additionally, the upward and downward moving fires likely show different behavior in fire propagation, because of the asymmetric setup.

In the following, the dynamic development of the fire propagation rate is investigated. Aim is to find a proper definition, which will be used throughout the following discussions.

The discussion on the propagation rate is based on the illustration in Fig. 3.15. It shows the fire propagation as simulated in the example from the previous section. White isolines mark the combustion front at different times, where the coal concentration is as high as at the initial state ($c_{f,0} = 850 \text{ kg m}^{-3}$). Thus, these isolines mark the untouched coal seam. The geometry of the combustion front is approximated by the black lines.

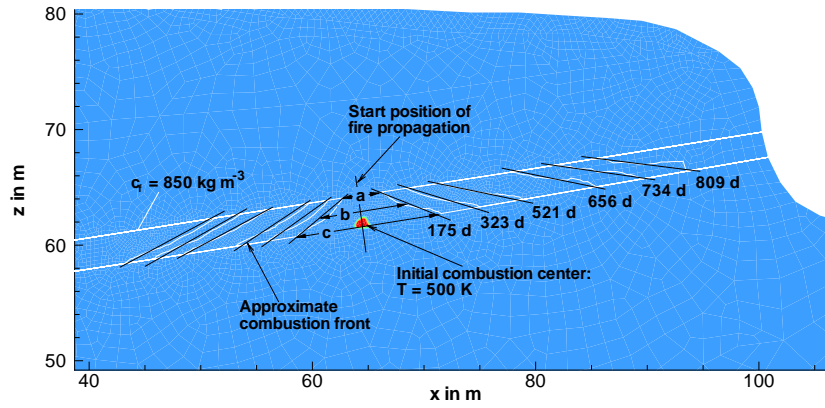


Figure 3.15 Illustration for the definition of the propagation rate. White isolines mark the coal concentration $c_{f,0} = 850 \text{ kg m}^{-3}$ at different times in days. Black lines approximate the geometry of the combustion front.

The distance between the combustion fronts of the up- and downward moving fire fronts is determined in two different ways: (1) as the average of distances 'a' and 'c', termed l in the following. l is determined according to $l = (a + c)/2$. (2) as the distance 'b' in the center of the seam. With these definitions the fire propagation rate becomes $v_{pr}^{av} = 0.5l/t$ and $v_{pr}^c = 0.5b/t$, respectively, where t is the simulation time. Superscripts *av* and *c* stand for *average* and *center*. Division by two is performed to determine the fire propagation rate in only one direction, however, without distinction between the up- and downward fire propagation rates.

Additionally, both definitions (1) and (2) were used separately for the up- and downward moving fires, i.e. the distances between the approximate geometries of the combustion fronts and the start position line of fire propagation (see Fig. 3.15). The latter definitions are used to investigate the difference in fire propagation between up- and downward moving fires. For the upward moving fire, the propagation rates are termed $v_{pr}^{av,up}$ and $v_{pr}^{c,up}$. For the downward moving fires, $v_{pr}^{av,d}$ and $v_{pr}^{c,d}$ are used.

Finally, attention is paid on the dynamic development of the fire propagation rate, for which the rates are determined according to the distances the combustion front moves between two consecutive times. Thus, the fire propagation rates are formulated as $v_{pr,dyn}^{av} = \Delta l / \Delta t$ and $v_{pr,dyn}^c = \Delta b / \Delta t$, where e.g. Δb is the distance $b_{t=521d} - b_{t=323d}$ between combustion fronts a time interval $\Delta t = 521d - 323d$ apart. The results of investigation of fire propagation are presented in Tabs. 3.7 and 3.8.

t in d	v_{pr}^c	$v_{pr,dyn}^c$	v_{pr}^{av}	$v_{pr,dyn}^{av}$
175	8.3	8.3	8.4	8.4
323	7.3	6.2	7.5	6.3
512	6.6	5.3	6.6	5.1
656	8.4	15.4	8.4	15.4
734	9.2	16.0	9.1	14.9
809	10.9	16.6	9.8	16.9

Table 3.7 Fire propagation rates in ma^{-1} without distinction between up- and downward moving fires. Definitions: $v_{pr}^c = 0.5(b/t)$, $v_{pr,dyn}^c = 0.5(\Delta b/\Delta t)$, $v_{pr}^{av} = 0.5((a+c)/2t)$, $v_{pr,dyn}^{av} = 0.5((\Delta a/\Delta c)/2t)$, see Fig. 3.15 for nomenclature.

t in d	$v_{pr}^{c,up}$	$v_{pr,dyn}^{c,up}$	$v_{pr}^{c,d}$	$v_{pr,dyn}^{c,d}$
175	9.0	9.0	7.6	7.6
323	8.0	6.7	6.4	5.0
512	7.5	6.7	5.6	4.2
656	9.9	19.1	6.8	11.7
734	10.9	19.1	7.4	11.7
809	11.8	21.0	7.9	13.3

Table 3.8 Fire propagation rates in ma^{-1} for the up- and downward moving fires, respectively. Definitions: $v_{pr}^{c,up} = b^{up}/t$ and $v_{pr,dyn}^{c,up} = \Delta b^{up}/\Delta t$ for the upward moving fires, $v_{pr}^{c,d} = b^d/t$ and $v_{pr,dyn}^{c,d} = \Delta b^d/\Delta t$ for the downward moving fires, see Fig. 3.15 for nomenclature.

From the results the following attributes concerning the propagation rate are observed:

1. The propagation rate is not constant, and different definitions result in different propagation rates. With all definitions, the fire propagation rate first decreases, and then increases with time.
2. Concerning the rate between up- and downward moving fires, there is insignificant difference between the average propagation rate (for distances at the top and bottom of the seam) and the propagation rate defined in the center of the seam.
3. A significant difference is observed between the static and the dynamic definition, respectively. If the propagation rate is determined from the travel distance beginning

at the starting position (static definition), the rate remains more or less constant. For the dynamic definition, according to which the propagation rate is determined from the travel distance between two consecutive time steps, the rate is more variable.

4. Finally, the upward moving fire is faster than the downward moving one. This observation is likely based on the oxygen pathway, which gets smaller for the upward and larger for the downward moving fire, respectively, with increasing time. Another reason might be the direction of convective energy transport, which occurs in the upward direction. Because, for the upward moving fire, the seam dips towards the same direction as convective energy transport, the front of the upward moving fire may be heated more efficiently than the downward moving one, resulting in an accelerated fire propagation.

Due to the observations from above, i.e. the dynamic behavior of the fire propagation rate, a proper definition of the propagation rate needs to be defined in order to enable the comparison between different simulation results. For the following considerations, the propagation rate is defined as the rate observed after the fire front reaches a distance of 20 meters in the center of the seam (distance 'b' in Fig. 3.15). The propagation rate is then determined according to (cf. Fig. 3.15)

$$v_{pr}^c = 0.5(b/t). \quad (3.37)$$

4 Sensitivity Studies

In the following, a sensitivity study is presented where the influence of various parameters on the fire propagation is investigated. Parameters under investigation are:

- k in m^2 , the permeability, which is a parameter in the Forchheimer equation, Eq. 2.21,
- λ_{eff} in $W m^{-1} K^{-1}$, the effective thermal conductivity, Eq. 2.35,
- ℓ in m , the Representative Length, which represents a macroscopically averaged length over which the oxygen concentration within the combustion front decreases from its initial value to $1/e$ (see Sec. 2.2.3 for the definition).

Parameters k and λ_{eff} are considered because they are assumed to have strong influence on the dynamic behavior of underground coal fires. Variations of ℓ have been investigated because ℓ has been introduced into the model as a new macroscopic parameter.

The underground coal fire is characterized by its propagation rate through the seam as defined in Sec. 3.5.3 and by the maximum combustion temperature. For this study, the setup from the example simulation (Sec. 3.5, Fig. 3.8) was taken. Parameters that have not been changed for the sensitivity study are given in Tab. 3.5. A summary and a discussion about the orders of magnitude of simulation results are given at the end of this chapter.

4.1 Permeability Variations

Beside of the fluid viscosity, which varies over one order of magnitude for a temperature range $300 K < T < 1000 K$ (VDI-Wärmeatlas, 2002), k is the proportionality factor relating pressure gradients to the specific flow rate q , which is defined as the volume flow rate Q through an area of size A : $q = Q/A$. The specific flow rate is coupled to the convective transport for energy and chemical species. An influence of k on the fire propagation rate can be expected, because an increase of q increases the amount of oxygen that is convectively transported to the fire. In addition, the permeability might influence the combustion temperature due to the coupling between the specific flow rate and convective energy transport.

The permeability exclusively depends on the structural nature of discontinuous porous or fractured media and varies over many orders of magnitude for different rocks. E.g., clay exhibits permeabilities of about $10^{-18} m^2$, whereas the permeability of sandstones varies between $10^{-12} m^2$ and $10^{-16} m^2$ (Guéguen and Palciauskas, 1994). Coarse-grained gravels exhibit values around $10^{-7} m^2$ (Nield and Bejan, 1999).

For the investigation of permeability variations a homogeneous distribution of k is assumed, with the same values for seam and embedding rocks. Thus, the considered continuum-based model allows an investigation of the fire development with respect to matrix flow through adjacent rock formations. Flow in fractures has not been considered.

For $\ell = 0.05\text{ m}$ and $\beta = 7 \times 10^{-9}\text{ W m}^{-1}\text{ K}^{-4}$, the following results were obtained: For permeabilities $k \leq 10^{-10}\text{ m}^2$, an underground coal fire did not develop. Obviously, the nest within the seam (Fig. 3.8) with $T = 500\text{ K}$ is not sufficient for ignition. For higher permeabilities the propagation rate varies between 3 meters per year for $k = 5 \times 10^{-10}\text{ m}^2$ and 218 meters per year for $k = 10^{-8}\text{ m}^2$. A graphical representation is given in the summary, together with variations of the propagation rate in dependence of λ_{eff} .

The development of the maximum combustion temperature is presented in Fig. 4.1 for different permeabilities. For $k = 10^{-8}\text{ m}^2$ the fire propagates very fast and reaches the boundaries of the domain in less than 100 days. Hence, the temperature development is rapidly changing and, after 100 days, becomes strongly influenced by the boundary conditions. For permeability values $k = 5 \times 10^{-10}\text{ m}^2$ and $k = 10^{-9}\text{ m}^2$ the maximum temperature first increases and then converges to a constant value. For $k = 10^{-9}\text{ m}^2$ and $k = 5 \times 10^{-10}\text{ m}^2$, the maximum temperature converges against 1400 K and 1000 K , respectively.

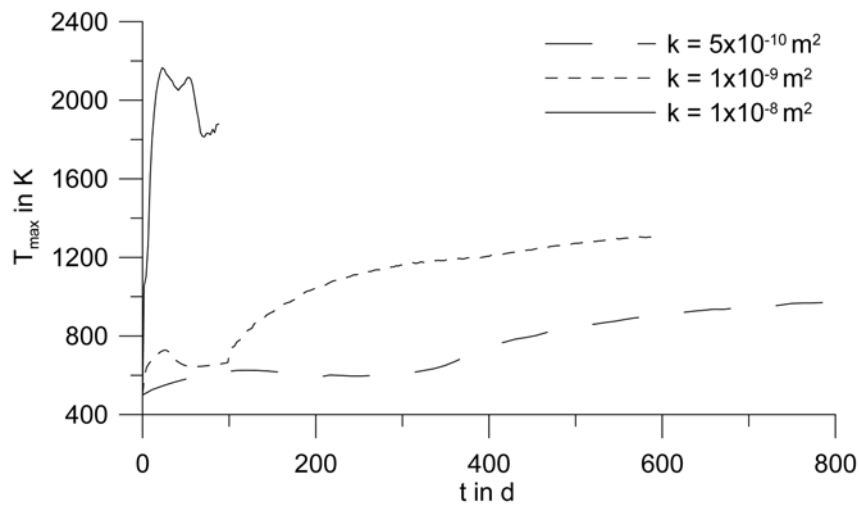


Figure 4.1 Development of the maximum temperature for different permeabilities k . $\ell = 0.05\text{ m}$, $\beta = 7 \times 10^{-9}\text{ W m}^{-1}\text{ K}^{-4}$.

4.2 Thermal Conductivity Variations

In the following, attention is paid on conductive and radiative heat transport. The mechanisms are expressed by the effective thermal conductivity (Eq. 2.35):

$$\lambda_{eff}(T) = \lambda_0 + \beta(T - T_0)^3 = \lambda_0 + \lambda_r. \quad (4.1)$$

λ_0 is the thermal conductivity at ambient (reference) temperature T_0 , where radiation has minor influence on heat transport. λ_0 is an important parameter for the ignition of an intact coal seam. When λ_0 is small, heat accumulates due to insufficient heat release by conduction, which in turn accelerates the chemical reaction. Hence, ignition may occur. In

contrast, large values of λ_0 cause an effective transport of heat. Then, heat does not accumulate and the coal does not ignite.

Variations of λ_0 can occur due to mechanical disruption of coal as a result of thermal expansion and subsequent cracking. Higher thermal conductivities are observed for media having a well-connected structure like fine-grained sandstones, in comparison to highly discontinuous media with a badly-connected structure. Thus, an increase in porosity decreases the thermal conductivity (see e.g. Clauser and Huenges, 1995, for such observations).

The reason for this behavior is that conductive heat flow in the minerals of the solid matrix is higher than in air. For the latter, the thermal conductivity is in the order of $0.05 \text{ W m}^{-1} \text{ K}^{-1}$ (VDI-Wärmeatlas, 2002). Thermal conductivities for coal and sandstone are $0.1 - 1 \text{ W m}^{-1} \text{ K}^{-1}$ (Zelkowski, 1986) and $2 - 3 \text{ W m}^{-1} \text{ K}^{-1}$ (Guéguen and Palciauskas, 1994), respectively, due to the high thermal conductivities of the rock-forming minerals.

At high temperatures, the term $\beta(T - T_0)^3$ in Eq. 4.1 becomes dominant. In this temperature regime the coal fire is sensitive to the constant β .

This part of the sensitivity study is divided into two parts. The first part investigates the influence of λ_0 on the development of the small initial nest with increased temperature of 500 K (Fig. 3.8). The second part considers the influence of radiant heat transport. Here, the coal fire is characterized by the maximum combustion temperature.

4.2.1 Influence on the Ignition of Coal Seams

The ignition of the coal seam has been investigated by varying the thermal conductivity between $0.1 \text{ W m}^{-1} \text{ K}^{-1} \leq \lambda_0 \leq 1.0 \text{ W m}^{-1} \text{ K}^{-1}$ for coal and $2.0 \text{ W m}^{-1} \text{ K}^{-1} \leq \lambda_0 \leq 3.0 \text{ W m}^{-1} \text{ K}^{-1}$ for rock. Radiation has been omitted, hence $\beta = 0$.

The results are presented in Fig. 4.2. The diagram shows that, for the considered model, the coal seam only ignites when $\lambda_0 = 0.1 \text{ W m}^{-1} \text{ K}^{-1}$ for coal and $\lambda_0 = 2.0 \text{ W m}^{-1} \text{ K}^{-1}$ for embedding rocks. At higher values ignition does not occur, because the heat within the initial high-temperature nest is effectively removed by the surrounding material.

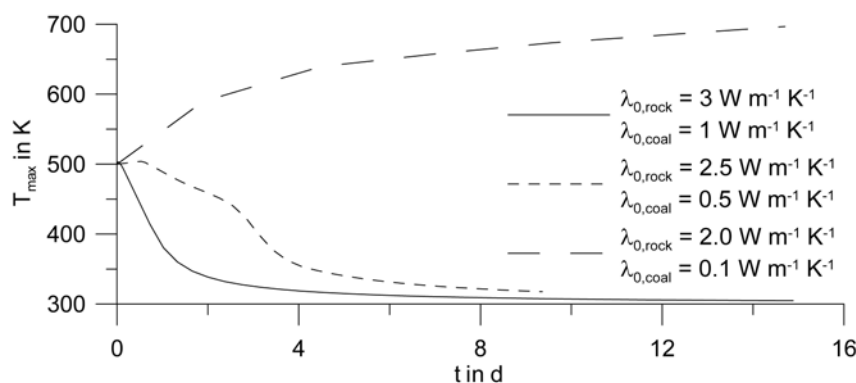


Figure 4.2 Temporal development of the maximum temperature with respect to variations of λ_0 for coal and rock, respectively

4.2.2 Influence on Burning Coal Seams

Once burning, radiation becomes an effective heat transport mechanism that controls the combustion temperature. The sensitivity study has been performed by varying the constant β in Eq. 4.1. The temperature dependent thermal conductivity for different values of β is presented in Fig. 4.3.

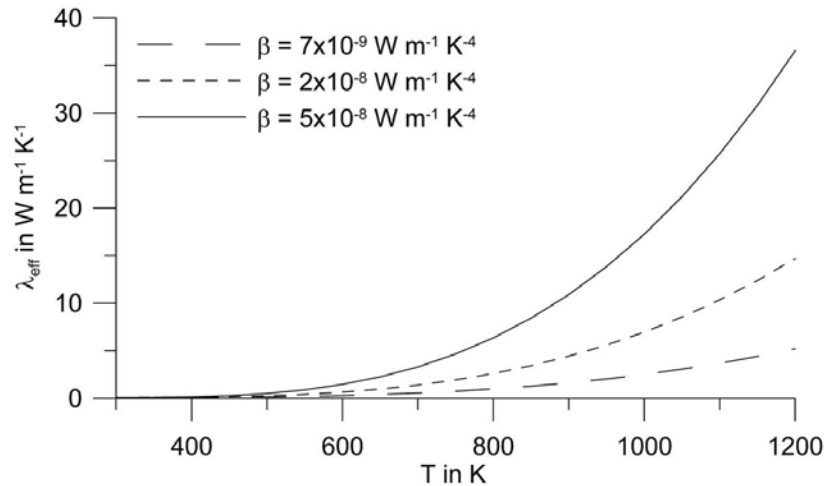


Figure 4.3 Temperature dependent thermal conductivities, $\lambda_{eff}(T)$, Eq. 4.1, for different values of β

Fig. 4.4 presents the simulated coal fire after 484 days with respect to different temperature dependent thermal conductivities from Fig. 4.3. The black lines representing the distribution of the coal concentrations show that the fire propagated nearly the same distance through the seam. The propagation rate is thus nearly independent of the thermal conductivity.

The temporal development of the maximum combustion temperature varies for different effective thermal conductivities λ_{eff} (Fig. 4.5). Increasing β (i.e. increasing the dominance of radiative heat transport) decreases T_{max} . For $7 \times 10^{-9} \text{ W m}^{-1} \text{ K}^{-4} \leq \beta \leq 5 \times 10^{-8} \text{ W m}^{-1} \text{ K}^{-4}$ the maximum temperature varies between 900 K and 1300 K ($k = 10^{-9} \text{ m}^2$), and between 1400 K and 2200 K ($k = 10^{-8} \text{ m}^2$). Total neglect of radiation ($\beta = 0$) yields strongly increasing temperatures, up to unrealistically high values after 100 days of simulation time. Accordingly, radiation can be said to be the only heat transport mechanism that lowers the combustion temperature to reasonable magnitudes (e.g. Stracher and Taylor, 2004, report about combustion temperatures up to 1300 K).

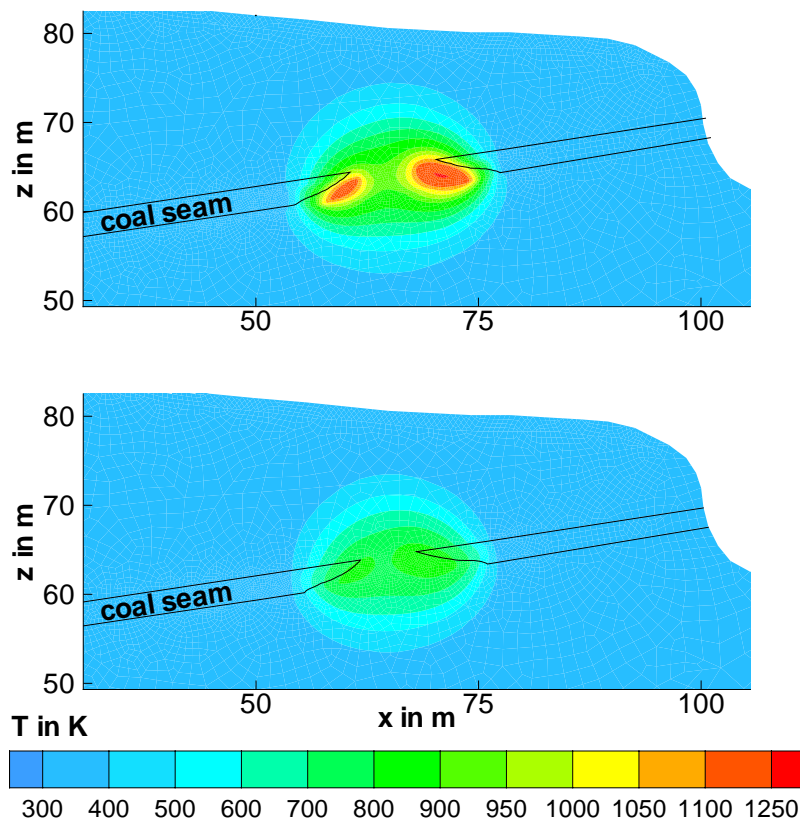


Figure 4.4 Temperature distribution (colored contours) and distribution of coal (represented by black lines) after 484 days obtained for different effective thermal conductivities λ_{eff} , where $\beta = 7 \times 10^{-9} \text{ W m}^{-1} \text{ K}^{-4}$ (top) and $\beta = 5 \times 10^{-8} \text{ W m}^{-1} \text{ K}^{-4}$ (bottom).

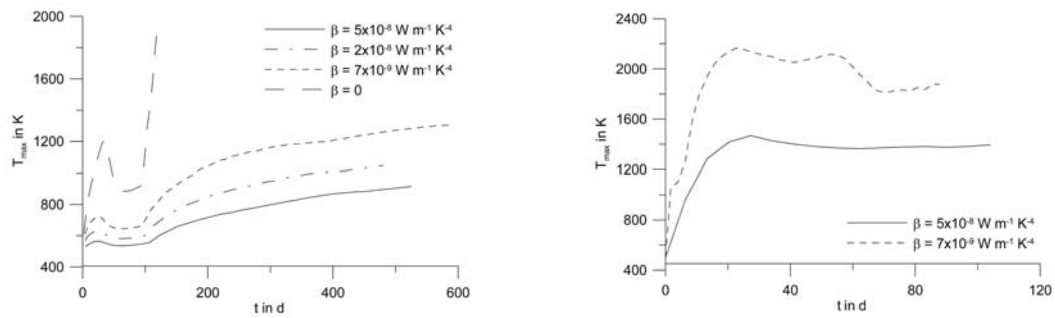


Figure 4.5 Temporal development of the maximum temperature for different temperature dependent thermal conductivities and for permeabilities $k = 10^{-9} \text{ m}^2$ (left) and $k = 10^{-8} \text{ m}^2$ (right)

4.3 Variations of the Representative Length

For the sensitivity study of ℓ the permeability and the constant β in the effective thermal conductivity were taken as $k = 10^{-9} m^2$ and $\beta = 7 \times 10^{-9} W m^{-1} K^{-4}$, respectively. The simulated fire propagation rates are summarized in Table 4.1 for the range $0.005 m < \ell < 0.5 m$. Propagation rates between 3.7 and 9.7 meters per year are obtained for this range.

ℓ in m	0.005	0.05	0.5
v_{pr} in ma^{-1}	10	4	4

Table 4.1 Fire propagation rates, v_{pr} , for varying Representative Lengths, ℓ (values have been rounded of, see discussion in Sec. 4.5)

The development of the maximum combustion temperature is presented in Fig. 4.6. Accordingly, T_{max} increases faster the smaller ℓ is. The long-term trend of the maximum temperature is similar for the whole range of ℓ , reaching approximately 1300 K.

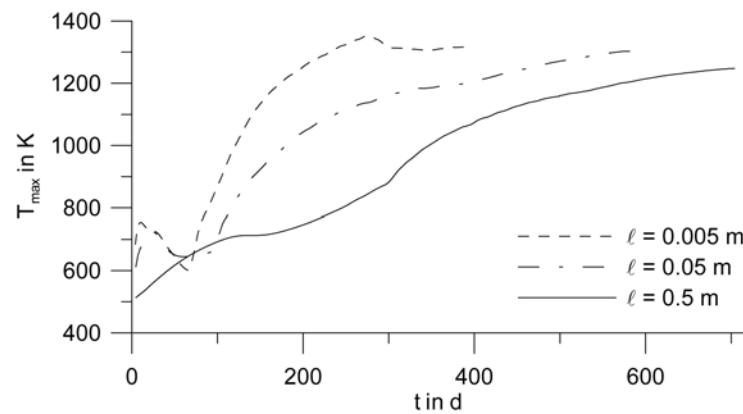


Figure 4.6 Temporal development of the maximum combustion temperature for different Representative Lengths ℓ

4.4 Summary

For the sensitivity study coal fires have been analyzed with regard to the fire propagation rate and the maximum combustion temperature. These properties have been investigated concerning variations of the effective thermal conductivity λ_{eff} , the permeability k , and the Representative Length ℓ .

In comparison to the effect of k and λ_{eff} , variations of the Representative Length show an insignificant influence on both, the fire propagation rate and the maximum combustion temperature. The fire propagation rate varies by a factor of three for a range of ℓ over two orders of magnitude. The long-term behavior of the maximum temperature is similar.

The fire propagation rate in dependence of λ_{eff} and k is graphically presented in Fig. 4.7. Based on Fig. 4.7 and the representations from above, the following conclusions can be drawn from the sensitivity study:

1. The permeability needs to be sufficiently high ($k > 10^{-10} m^2$) to sustain an underground coal fire. This observation has already been concluded by Huang et al. (2001) from temperature and gas transport simulations.
2. Permeability variations have major influence on the fire propagation rate. This is not a surprising result, because an increase of k also increases the volume flow rate of oxygen. An increase of the permeability by half an order of magnitude increases the fire propagation rate by one order of magnitude.
3. For permeabilities $k \geq 10^{-8} m^2$ very high propagation rates are observed. However, it is dubious whether the surrounding medium can still be considered as porous at such high values. The physical model becomes unrealistic when the void space in the rocks gets too large. Hence, observations obtained for $k \geq 10^{-8} m^2$ need to be handled with care.
4. Permeability also affects the combustion temperature, which is likely due to the coupling between convective energy transport and the specific flow rate. For the considered range of permeabilities the maximum combustion temperature remained below 2400 K, whereas this value has been obtained for the dubiously high permeability value of $k = 10^{-8} m^2$. Otherwise, the maximum combustion temperature does not exceed 1400 K.

For further improvements of the model, the above observations could be validated by laboratory experiments in which the fire propagation rate through a probe is investigated with a predefined volume flow of oxygen. In this context, the magnitude of the Representative Length could also be investigated.

Results of the sensitivity study give the following suggestions for fire safety and fire fighting issues:

- The constant λ_0 in the effective thermal conductivity λ_{eff} controls the ignition of coal seams. It has been shown that the seam ignites only for small λ_0 . Thus, fine-grained coal material with a low thermal conductivity (which is e.g. left in abandoned mines)

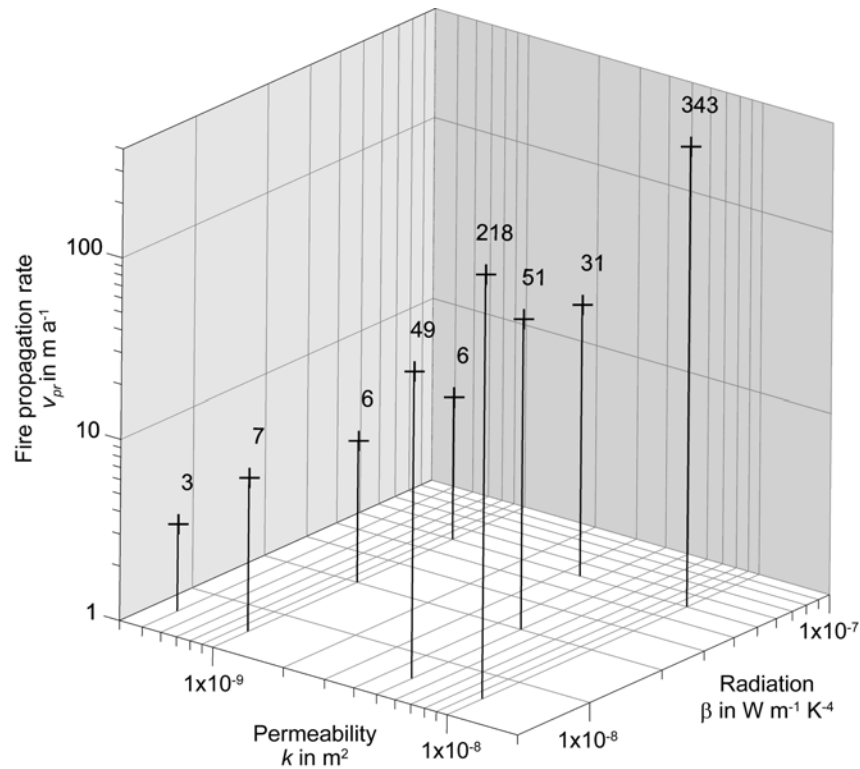


Figure 4.7 Fire propagation rate, v_{pr} , in dependence of the effective thermal conductivity, $\lambda_{eff} = \lambda_0 + \beta(T - T_0)^3$, and the permeability, k

should be sufficiently protected. One possibility is to seal the material to circumvent oxygen penetration.

- The permeability around an underground coal fire needs to be sufficiently high to ensure oxygen supply by thermal buoyancy as driving mechanism. According to the simulations, permeabilities $k \leq 10^{-10} \text{ m}^2$ are too small to sustain a fire. Accordingly, underground fires need to be embedded in highly permeable porous rocks, like coarse-grained sandstone, or other causes must exist which enable oxygen penetration. One possibility is the existence of large-scale fractures through which a massive amount of oxygen can flow. Also, abandoned coal pits from small enterprises may cause oxygen supply. Finally, weathering-induced pressure gradients can lead to oxygen flow, in addition to convection by thermal buoyancy.

4.5 Orders of Magnitude of Simulation Results

The orders of magnitude over which simulation results change are important for a later comparison between simulation results and *in-situ* measurements. In addition, the following estimates demonstrate the applicability of the numerical simulation.

The spatial resolution of the simulation results depends on the size of the discretizing grid. At the surface, which is the relevant region for *in-situ* measurements, the grid resolution is about one meter. Readings about spatial extents are thus in the accuracy of one meter, so that decimal places can be neglected.

Fire propagations and resulting combustion temperatures have been simulated over time scales of years. The fastest propagation rate was 343 meters per year (Fig. 4.7), which is approximately 1 meter per day. Neither *in-situ* observations nor simulation results (compare the definition of the propagation rate, Sec. 3.5.3) can resolve a propagation rate of 1 meter per day. Hence, times smaller than one day do not need to be considered for the fire propagation. If no external processes are involved (which take place on time scales smaller than one day), the distributions of the temperature field and the oxygen and exhaust gas concentrations are directly dependent on the fire propagation rate, hence these distributions will also be presented with a maximum resolution of one day. If external processes are relevant, like daily varying atmospheric pressure distributions at the surface, a finer temporal resolution is necessary (e.g. in Sec. 5).

The specific flow rate is another observable which will be later compared with *in-situ* measurements. The rate is usually measured over minutes to hours, due to its low magnitudes (giving a lower bound) and the temporal variability at larger time scales (giving an upper bound). Hence, it is appropriate to specify specific flow rates in units of meters per hour. For a given permeability, the specific flow rate varies by one order of magnitude (Tab. 4.2, Fig. 3.12). Hence, a resolution smaller than one order of magnitude is not necessary.

Finally, the temperature in the system is in the order $O(10^3)$, so that decimal places for temperature readings are irrelevant.

k in m^2	10^{-8}	10^{-9}	5×10^{-10}
q_{min} in mh^{-1}	2	0.1	0.04
q_{max} in mh^{-1}	14	1.4	0.61

Table 4.2 Range of specific flow rates q for different permeabilities k according to Wessling and Kessels (2005b). q_{min} : minimum specific flow rate, q_{max} : maximum specific flow rate.

5 System Response Investigations

The flow behavior around the coal fire influences the combustion and the distribution of anomalies at the surface, like increasing temperatures or carbon dioxide concentrations. Detection of such anomalies is frequently performed to investigate the extent and development of the fire below surface.

In this chapter the response of the flow behavior on barometric pressure changes is investigated. Aim of this investigation is to quantify the response, as this is essential for the interpretation of *in-situ* measurements. The flow behavior is characterized by the flow velocity of gas, which in turn affects convection of chemical species and heat.

Previous investigations about the influence of barometric pressure changes on the flow behavior in the subsurface were for example performed by Massmann and Farrier (1992); Landmeyer (1996); Ahlers et al. (1999). Simulations by Massmann and Farrier (1992) showed that such changes cause horizontal gas transport in the vadose zone, which may significantly affect the readings from gas monitoring. Additionally, an influence of pressure changes on the flow behavior depends on complex interactions among many variables, including site geometry, material properties such as permeability, and the amplitude and period of the pressure. Landmeyer (1996) investigated the response of water levels on a winter cyclone moving across the Southeastern states of Georgia and South Carolina (US). Performed low barometric pressure recordings thus provided an investigation on regional scales. His methodology proved useful in examining the degree of aquifer confinement by using climatologic data. Ahlers et al. (1999) investigated the unsaturated zone near possible nuclear waste disposals. They interpreted the observed phase shift and amplitude change of the pneumatic records between the surface and subsurface, respectively.

Whereas the influences of pressure variations on the groundwater level and on gas transport in the vadose zone (both being rather passive systems) are straightforward, the flow behavior around underground coal fires is affected by complex interactions between changing atmospheric conditions and processes involved in such fires. Particularly near the surface, the following phenomena may affect the flow behavior:

1. Turbulent flow causing small-scale fluctuations in temperature and in species concentration. Turbulence can appear in large-scale discontinuities like fractures, where the flow velocity can be high.
2. Daily atmospheric pressure variations, causing changes in the flow velocity of exhaust gas and consequently affecting convective transport processes.
3. Daily varying heat exchange between the solid rock and the exhaust gas, caused by the changing solar irradiation between day and night. Accordingly, daily temperature variations in the exhaust gas have to be expected.

4. Instantaneous changes in the fracture system by rock-mechanical failure causing abrupt changes in temperature and species concentration due to suddenly changing flow paths in the overlying beds.
5. Changes in the regional weather pattern affecting wind direction and/or strength.
6. The slow propagation of the combustion center leading to long-term variations in temperature and species concentration.

The influence of external impacts plays a significant role for the interpretation of *in-situ* measurements and thus have to be removed from the signals to obtain the fire-induced signal only.

In-situ investigations of the interaction between the fire propagation and external impacts were performed by Schlömer et al. (2006). The authors performed temperature and species concentration measurements in the exhaust gas above an underground coal fire over a time period of four months. Additionally, a meteorological station recorded wind direction and velocity, as well as temperature and barometric pressure. Surprisingly, Schlömer et al. (2006) did not find any correlations between temporal changes in the weather pattern and monitored data. He argues that the occurrence of large-scale fractures likely causes a problem when interpreting *in-situ* measurements. The flow pattern in such large-scale fractures can become highly complex when being affected by winds according to hardly predictable rules.

Investigations of simplified systems will help to improve the understanding of the flow behavior around underground coal fires. As a first step, this chapter presents numerical simulations to investigate the influence of barometric pressure variations on the flow behavior. The influence of winds is also considered. Different from large-scale fracture systems as observed in coal fire sites, the homogeneous setup from Sec. 3.5 is used for simplicity. The purpose of the investigations is to understand the interaction between external variations and underground coal fires. It is not the aim to achieve a good agreement between simulation results and *in-situ* observations.

First, the response to atmospheric pressure variations will be discussed. Then, the influence of wind is presented and conclusions are drawn from the investigations.

5.1 The Influence of Atmospheric Pressure Variations

In the following, the circulation system will be investigated with respect to temporal pressure variations at the boundary of the domain. A prescribed temporal pressure variation is set at the boundary according to data from *in-situ* measurements. The ambient temperature and atmospheric pressure variations (Fig. 5.1) were in fact monitored in Fire Zone 3.2 of the Wuda coal mining area (Inner Mongolia, PR China). That test site will be described in Sec. 6.1 in more detail.

For simulation, the setup from the simulation example (Sec. 3.5) is used, which exhibits an uneven topography. Hence, a hydrostatic pressure distribution needs to be superimposed to the pressure variations at the boundary. The hydrostatic pressure distribution depends

on the density of air, which is in turn is a function of the current pressure and temperature situation of the air. Thus, the investigation of the influence of atmospheric pressure variations presumes the consideration of temperature and pressure curves at the boundary of the domain.

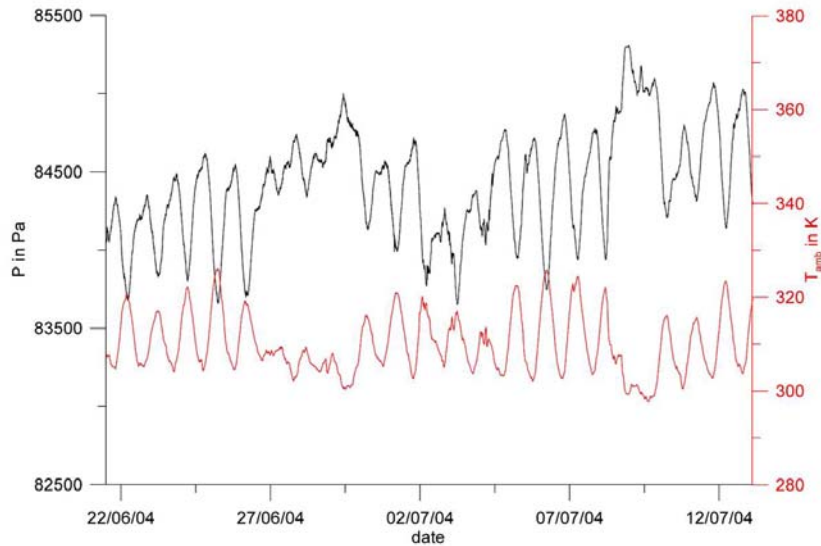


Figure 5.1 Pressure and ambient temperature variations used as boundary conditions for the simulation. The data have been monitored in Fire Zone 3.2 of the Wuda coal mining a (Inner Mongolia, PR China). For monitoring, a ProData data logger (Co. Phytex, Braunschweig, Germany) has been used, together with a PT100 sensor.

Atmospheric pressure variations can be expected to have an influence on gas motions through the subsurface. The expectation can be illustrated by an analytical solution for diffusion into a half space under sinusoidally varying surface conditions, assuming a homogeneous medium. If the surface pressure varies according to

$$P(z = 0, t) = P_0 \cos(\omega t), \quad (5.1)$$

the pressure P at depth z and time t is given by (Carslaw and Jaeger, 1959, pp. 65 - 66):

$$P(z, t) = P_0 e^{-z\sqrt{\omega/2D}} \cos(\omega t - z\sqrt{\omega/2D}). \quad (5.2)$$

D is the diffusivity and ω is the frequency. Eq. 5.2 describes the dependence of the attenuation and phase lag on depth; diffusivity and frequency also influence the signal characteristics in the subsurface. Eq. 5.2 shows that the transient signal will undergo little amplitude attenuation and phase lag for large values of diffusivity, while the transient signal will show larger amplitude attenuation and phase lag for small values.

For underground coal fires, gas diffusion plays an insignificant role. Instead, free thermal

convection can be expected to be the main driving force for gas motions, whenever externally induced pressure differences (e.g. caused by mine ventilation) are absent. Thus, some theoretical aspects concerning the interaction between thermally driven gas convection and temporally changing atmospheric pressures are useful for later discussion.

5.1.1 Extensions of the Model

For the consideration of temporal pressure and temperature variations in the atmosphere, i.e. $P = P(t), T = T(t)$, the density model in the physico-chemical setup has been extended. The density is formulated as the previously described equation-of-state from Sec. 2.2, Eq. 2.14:

$$\rho^f(P(t), T(t)) = \frac{P M_{air}}{T R}. \quad (5.3)$$

This density model includes the dependency on pressure and temperature, in contrast to the previous model, where only the temperature dependency has been considered.

In the mass balance equation, Eq. 2.17, the density appears in the storativity definition, Eq. 2.18, which had been assumed to be constant:

$$S = \Phi \frac{1}{\rho^f} \frac{\partial \rho^f}{\partial P}. \quad (5.4)$$

S has been derived from Eq. 2.16 by consideration of fluid compressibility with respect to pressure variations, only. This assumption will be further used for this investigation. The assumption is not valid within a small layer below the surface. In that layer, temporal temperature changes are expected due to the penetration of the temperature fluctuations at the boundary. However, the penetration depth will not exceed some centimeters for daily or weekly varying temperature fluctuations (for an estimation of the penetration depth, see Kessels, 1980, p. 32).

Continuing with the discussion about the pressure dependent density variations, the storativity (Eq. 5.4) can be transformed by insertion of the density model, Eq. 5.3:

$$\Phi \frac{1}{\rho^f} \frac{\partial \rho^f}{\partial P} = \Phi \frac{T R}{P M_{air}} \frac{\partial}{\partial P} \left(\frac{P M_{air}}{T R} \right) = \frac{\Phi}{P} =: S'(P(t)). \quad (5.5)$$

Due to a time-dependent pressure function, $P(t)$, the modified storativity is also a function of time. S' as a function of atmospheric pressure variations is graphically presented in Fig. 5.2, where $\Phi = 0.2$ has been used. The figure shows that variations in S' are two orders of magnitude smaller than the absolute value of S' . Therefore, assuming a constant storativity for the following investigations will have insignificant influence on the simulation results.

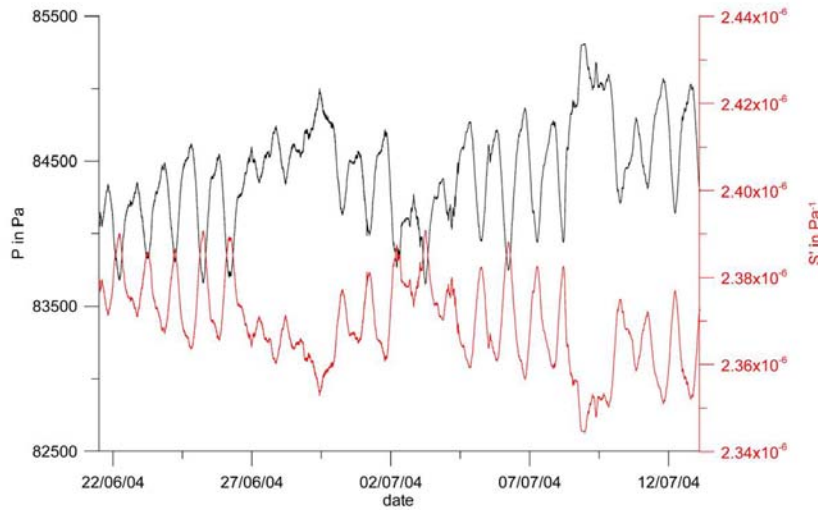


Figure 5.2 Time dependent modified storativity S' in Pa^{-1} as a function of monitored barometric pressure variations (cf. Eq. 5.5). For the porosity, $\Phi = 0.2$ has been used.

For further theoretical considerations, the mass balance equation, Eq. 2.17, is discussed. Insertion of Darcy's law,

$$\mathbf{q} = -\frac{k}{\mu}(\nabla P - \rho^f(P, T)\mathbf{g}) \quad (5.6)$$

into Eq. 2.17 gives after some re-formulations

$$\nabla^2 P = \underbrace{S' \frac{\mu}{k} \frac{\partial P}{\partial t}}_1 + \underbrace{\nabla \bullet \rho^f(P, T)\mathbf{g}}_2 \quad (5.7)$$

\mathbf{q} is the specific flow rate, k is the permeability, μ is the dynamic viscosity, \mathbf{g} is the gravitational acceleration (cf. Tab 3.5). Eq. 5.7 states that pressure differences giving rise to fluid motions (the left hand side) result from two mechanisms: temperature dependent pressure variations, formulated by term 1, and thermal buoyancy, formulated by term 2.

5.1.2 Boundary Conditions

Boundary conditions for pressure and temperature were extended to consider externally imposed temporal variations of these variables. In case of Dirichlét boundary conditions for pressure, a hydrostatic distribution is required for the simulator. For that purpose, the pressure at the boundary is formulated as

$$P(z, t) = P_{z_0}(t) + \mathbf{g} \int \rho^f(P(z, t), T_{amb}(t)) dz \quad (5.8)$$

$$= P_{z_0}(t) + \mathbf{g} \int \frac{P(z, t)}{T_{amb}(t)} \frac{M_{air}}{R} dz. \quad (5.9)$$

$P_{z_0}(t)$ and $P(z,t)$ are the pressure variations at reference height z_0 and height z , respectively, and $T_{amb}(t)$ is the variation of the ambient temperature at the boundary. Eq. 5.8 can be extended to

$$\begin{aligned} P(z,t) &= P_{z_0}(t) + \mathbf{g} \left(\int \frac{P_{z_0}(t)}{T_{amb}(t)} \frac{M_{air}}{R} dz + \int \frac{P(z,t) - P_{z_0}(t)}{T_{amb}(t)} \frac{M_{air}}{R} dz \right) \quad (5.10) \\ &= P_{z_0}(t) + \mathbf{g} \left(\int \frac{P_{z_0}(t)}{T_{amb}(t)} \frac{M_{air}}{R} dz + \int \frac{\Delta P(z,t)}{T_{amb}(t)} \frac{M_{air}}{R} dz \right). \end{aligned}$$

The pressure difference in the second integral of Eq. 5.10 is of about three orders of magnitude smaller than the absolute value of the atmospheric pressure. Thus, the second integral can be neglected, resulting in the formulation

$$P(z,t) = P_{z_0}(t) + \mathbf{g} \frac{P_{z_0}(t)}{T_{amb}(t)} \frac{M_{air}}{R} \Delta z \quad (5.11)$$

for the temporal development of the absolute pressure at the boundary. Boundary conditions for chemical components were not changed, hence the conditions from the simulation example were used (cf. Sec. 3.5).

The following discussion is based on atmospheric pressure variations. Temperature variations will not be considered in detail, because they only have an influence in the small surface layer.

5.1.3 Simulation

The simulations have been performed by extending the example from Sec. 3.5. An underground coal fire within the seam has already been developed, but without consideration of external influences. Beginning after 596 days of simulation time, the ambient temperature and atmospheric pressure variations were included as boundary conditions (Fig. 5.1).

The system response was then investigated at different locations within the system, from which three of them are presented here. The three observation points are located in the combustion center of the downward moving fire (point 1, Fig. 5.3), just below the surface (point 2), and in the zone where the oxygen concentration is changing (point 3, Fig. 5.4). Simulation has been performed over the monitoring time of 20 days. Due to that short time interval and a slow fire propagation rate (~ 10 meters per year), the locations of the combustion centers remain nearly constant. The temperature and oxygen distribution do not change remarkably during the simulation, hence the distributions from Figs. 5.3 and 5.4 are representative for the whole investigated time.

For each process, a different response time can be expected, because the processes take place at different time scales. Hence, a response time for the pressure, the temperature and the concentration of chemical species exists. For the latter two, conductive and convective transport mechanisms can also respond differently to externally imposed influences. The following investigations concentrate on convective transport mechanisms, because conduction/diffusion takes place at time scales much longer than the time period for which monitored data are available.

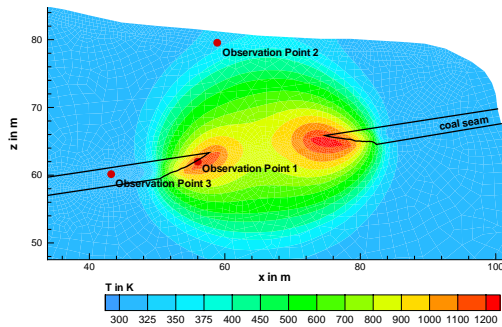


Figure 5.3 Temperature and observation points for the system response investigations

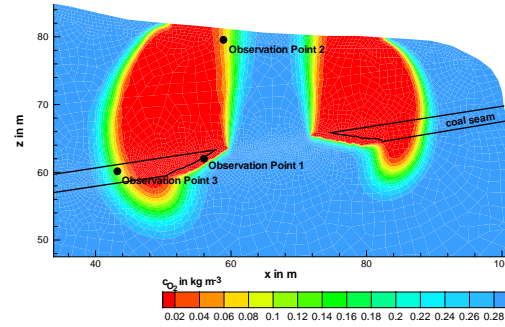


Figure 5.4 Concentration of oxygen and observation points for the system response investigations

Impulse Response

Atmospheric pressure variations at the surface affect the gas motions in the subsurface. Gas motion is the mechanism for convective transport of heat and species. As a first step, the influence of atmospheric pressure variations on gas motions is demonstrated by simplified pressure boundary conditions.

Dirichlet pressure boundary conditions were imposed at the surface as a function with positive constant slope. The pressure function and the system response at observation point 1 are presented in Fig. 5.5. The system response is characterized by the absolute value of the specific flow rate $|\mathbf{q}|$ which affects convective temperature and species transport.

The system response can be divided into four parts (cf. Fig. 5.5) with different interactions between external impacts (represented by the pressure boundary conditions) and the underground coal fire system:

1. In the first part, pressure boundary conditions are not changing with time. For a short simulation time (in comparison to coal fire propagation times), the system temperature does not change. Hence, thermal buoyancy does not change and $|\mathbf{q}|$ remains constant (cf. Eq. 5.7).
2. At the beginning of part two, pressure boundary conditions start to interact, resulting in a response of $|\mathbf{q}|$. Two impulses, one from above (term one in Eq. 5.7) and one from below due to thermal buoyancy (term two in Eq. 5.7) interact with each other.
3. The response of $|\mathbf{q}|$ is observed until the end of part two. At the beginning of part three, the rate of change in P equals the rate of gas flow resulting from thermal buoyancy. As a consequence, $|\mathbf{q}|$ remains constant, but of lower value in comparison to the initial case, although pressure is steadily increasing.
4. In part four, the pressure at the boundary is held constant, but of higher value in comparison to the initial case. Due to this change, $|\mathbf{q}|$ again gets constant after a short reaction time. Thereby, the value of $|\mathbf{q}|$ achieves the same magnitude as at the beginning (part one).

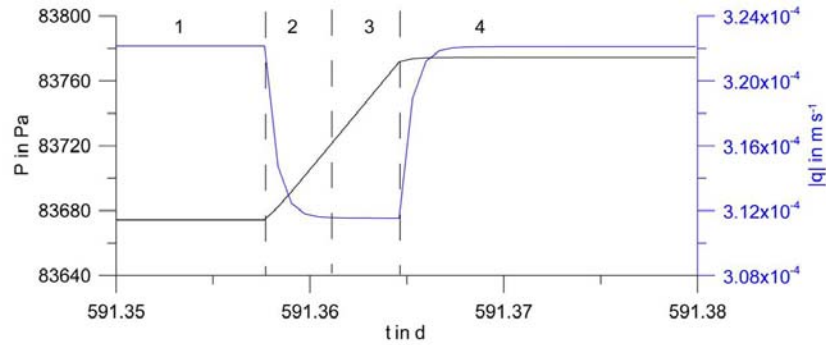


Figure 5.5 Response at observation point 1 of the absolute value of the specific flow rate, $|q|$, (the blue graph) to Dirichlet boundary conditions for the pressure as a function with constant positive slope (the black graph)

Response on Pressure Variations

The previous study shows that the specific flow rate responds to temporal pressure changes at the surface. Hence, a response on the distributions of temperature and species concentrations can also be expected, whenever convection is the dominant transport mechanism for these variables.

The response on pressure variations at the boundary is discussed for the pressure, the temperature, and the oxygen concentration. Therefore, the temporal behavior of these variables is considered at the observation points. In addition, temporal changes of the spatial oxygen distribution are introduced.

The pressure response is presented in Fig. 5.6 for observation points 1 and 3. The pressure at observation point 2 shows marginal differences to the pressure variations at the boundary, due to the small distance between the boundary and that observation point. The pressure increases with increasing depth, due to the hydrostatic distribution. Oscillations with a one-day period are observed for all observation points. A lateral variation of the system response can be investigated by comparison between the pressure at observation points 1 and 3 (Figs. 5.3 and 5.4). Any lateral variation of the system response is not observed, as shown by the nearly same pressure graphs in Fig. 5.6. A phase shift between the pressure at the surface and at the subsurface observation points is not resolved. Likewise, the amplitude does not change with increasing distance from the surface.

Temporal changes of the spatial oxygen distribution are presented in Fig. 5.7, where isolines mark the concentration $c_{O_2} = 0.16 \text{ kg m}^{-3}$. The contour plot presents the temperature distribution for orientation. The isolines show that the oxygen distribution varies during one day. The variations are observed for the whole system, except in the combustion center.

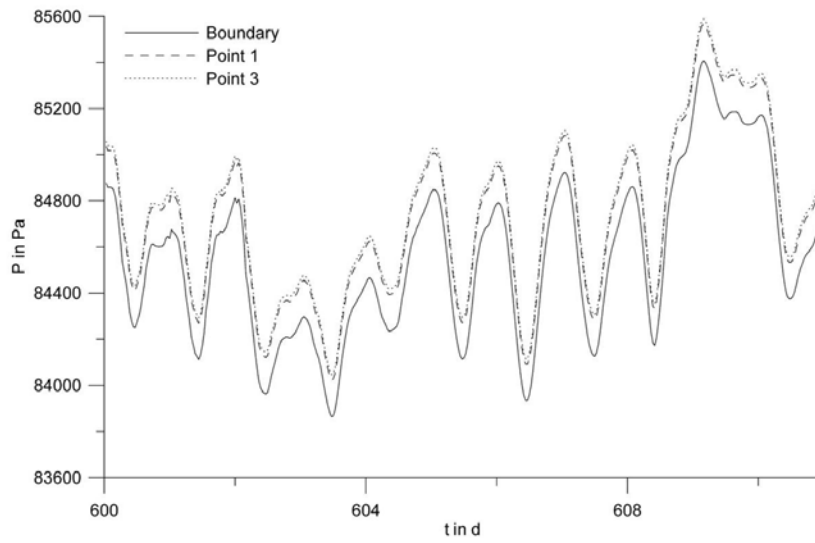


Figure 5.6 Pressure response at observation points 1 and 2 to the externally imposed pressure variations at the boundary

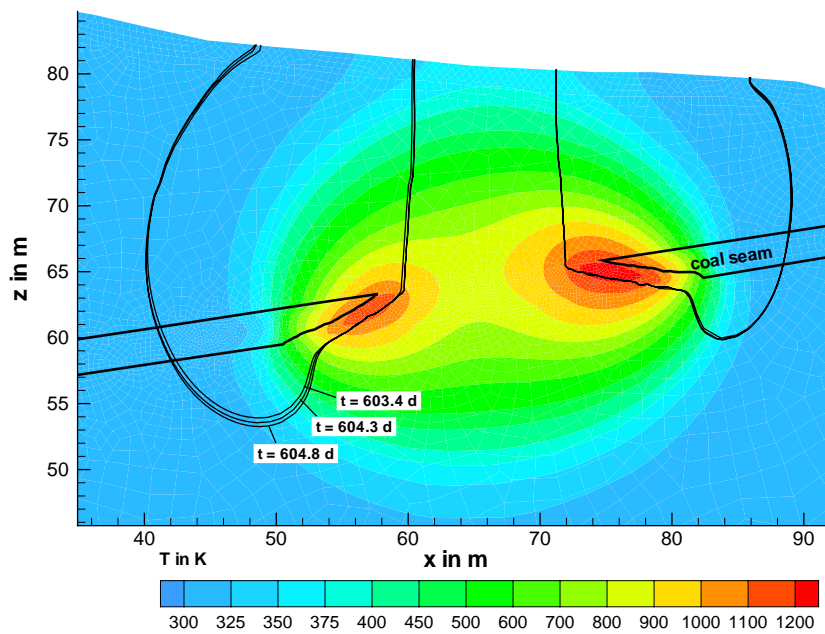


Figure 5.7 Illustration of the varying distribution of the oxygen concentration with time. The oxygen concentration is marked by the isolines, where $c_{O_2} = 0.16 \text{ kg m}^{-3}$.

The response of the temperature and the oxygen concentration at single observation points is graphically presented in Figs. 5.8. The top figure shows that both, the temperature and the oxygen concentration are responding to the pressure signal. The oxygen concentration oscillates according to the pressure with a time shift of about 0.3 days. The amplitude of oscillations is very small. The amplitude of the temperature response is higher, varying about 6 Kelvin within 11 days. The oscillations do not clearly reflect the pressure signal, hence no phase shift is obvious. There might be a response on pressure signals with low frequency (around 604 days), but the daily oscillations observed for the pressure are not clearly present.

At observation point 2 (the center figure) a response on atmospheric pressure variations is given by the oxygen concentration. Besides of the daily oscillations, the oxygen signal shows an increasing trend. A phase shift between pressure and oxygen concentration is not given, which can be concluded from the obvious reflection of small-scale fluctuations with periods smaller than 1 day. The temperature in the center figure shows a non-linearly increasing trend about three Kelvin. Daily oscillations corresponding to pressure variations are not visible.

The bottom figure shows similar results as the center figure. The oxygen concentration responds to the pressure signal, with a phase shift of 0.6 days. The amplitude of the oscillation of the oxygen concentration varies by about a considerable value of 0.8 kg m^{-3} . During days 600 – 604, a long-term decreasing trend exists in both, the pressure and the oxygen concentration signal. At 610 days, the response of the oxygen concentration to the pressure becomes irregular, i.e. no 0.6-days phase shift is visible. The temperature increases linearly with time, by about 0.6 Kelvin. The graphs show that there is a different system response by species concentrations and the temperature, respectively. Species concentrations are responding at all three observation points to atmospheric pressure variations. In contrast, the temperature field responds to pressure variations only at observation point 1, i.e. in the combustion center.

The different observation of the temporal behavior between the species concentration and the temperature field indicates that different transport mechanisms are dominating. Convection of heat and species is affected by the flow velocity, which is in turn a result of thermal buoyancy. Thus, the specific flow rate is higher in and near the combustion center (where high temperatures prevail), in comparison to the locations apart from the combustion center (compare Fig. 3.12). For species concentrations, convection is the dominant transport mechanism throughout the subsurface system, because a response to externally imposed pressure variations is observable. Dispersion or molecular diffusion plays an insignificant role. In contrast, the temperature field is affected by convection in the combustion centers and by conduction at the other locations.

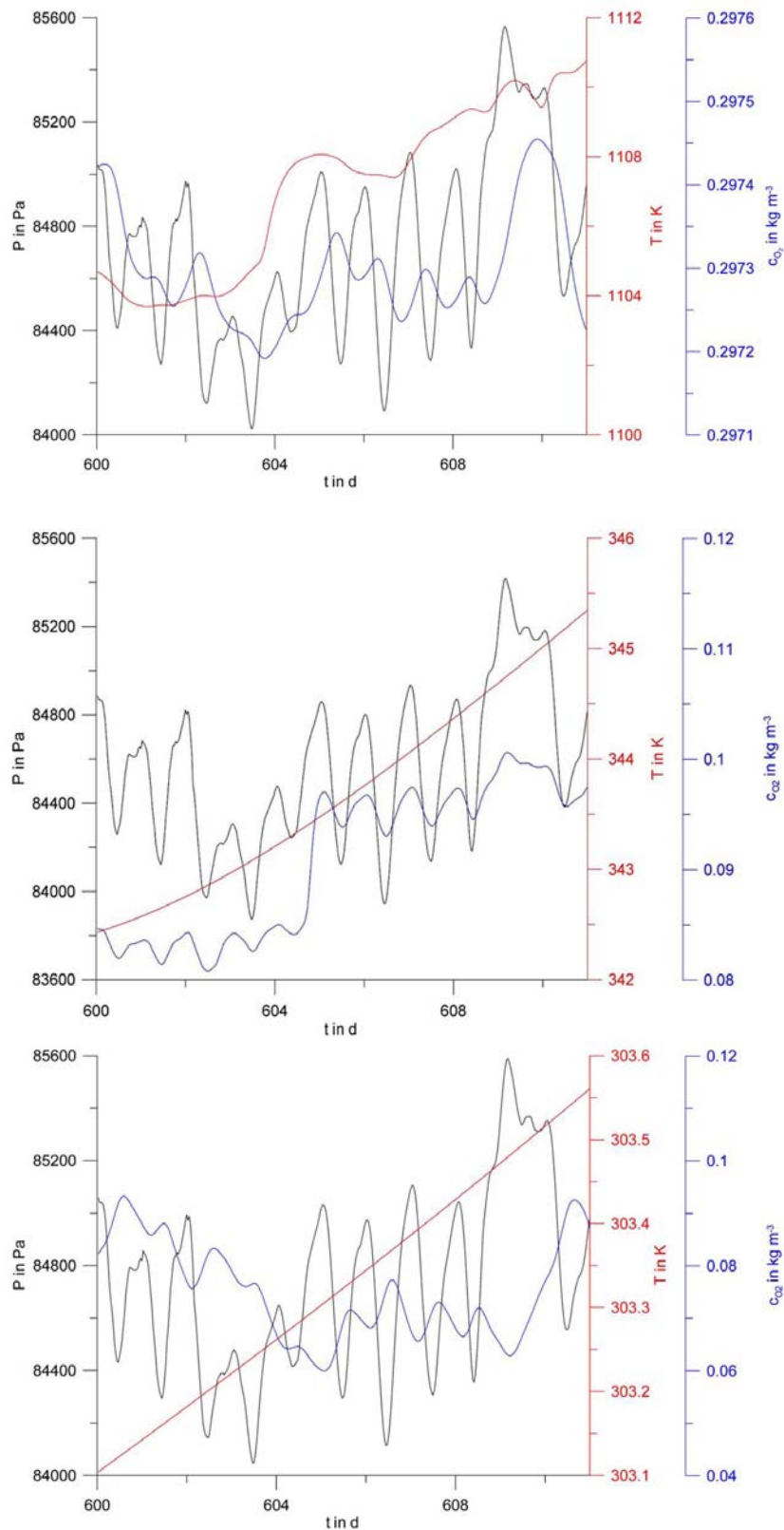


Figure 5.8 Response of temperature, oxygen concentration and pressure to atmospheric pressure variations at different observation points. Top: Observation point 1; center: Observation point 2; bottom: Observation point 3. Atmospheric pressure variations as in Fig. 5.6.

5.2 Influence of Winds

The influence of wind on coal fires has previously been investigated by Brooks et al. (1988a) as being a source for self-ignition in coal stockpiles. For underground coal fires, strong winds may result in increasing oxygen entry into the subsurface system through the discontinuous medium.

The investigation into the influence of winds is based on the simulation example from Sec. 3.5. Beginning with the developed underground coal fire as initial state, the simulations have been continued with a modified pressure distribution along the boundary of the domain (Fig. 5.2). The setup assumes an increased pressure at the outcrop, resulting from wind blowing against that outcrop.

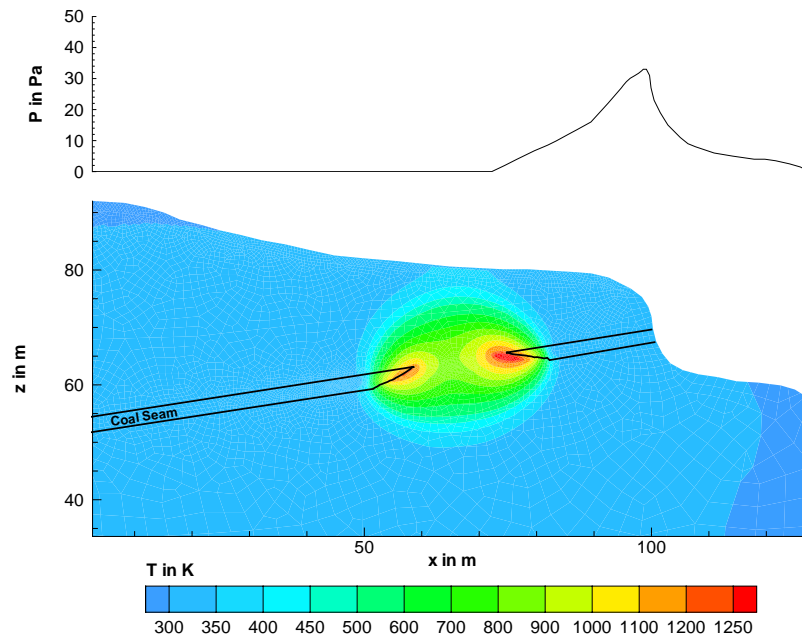


Figure 5.9 Setup for the investigation of wind blowing against the outcrop. The contour plot (bottom) shows the initial temperature distribution, the top graph presents the pressure distribution (hydrostatic part extracted) along the surface boundary.

The influence of winds is illustrated by the oxygen distribution. Fig. 5.10 shows the oxygen distribution as a result of wind in comparison to the case with only thermal buoyancy as driving mechanism. The results show the distribution after a simulation time of 15 days. Obviously, the oxygen distribution arising from the upward moving fire becomes smaller under the influence of winds.

The maximum temperature did not show significant variations under the influence of winds. After 15 days, the maximum temperature raised from $T_{max} = 1306K$ to $T_{max} = 1307K$ for both simulations (with and without wind).

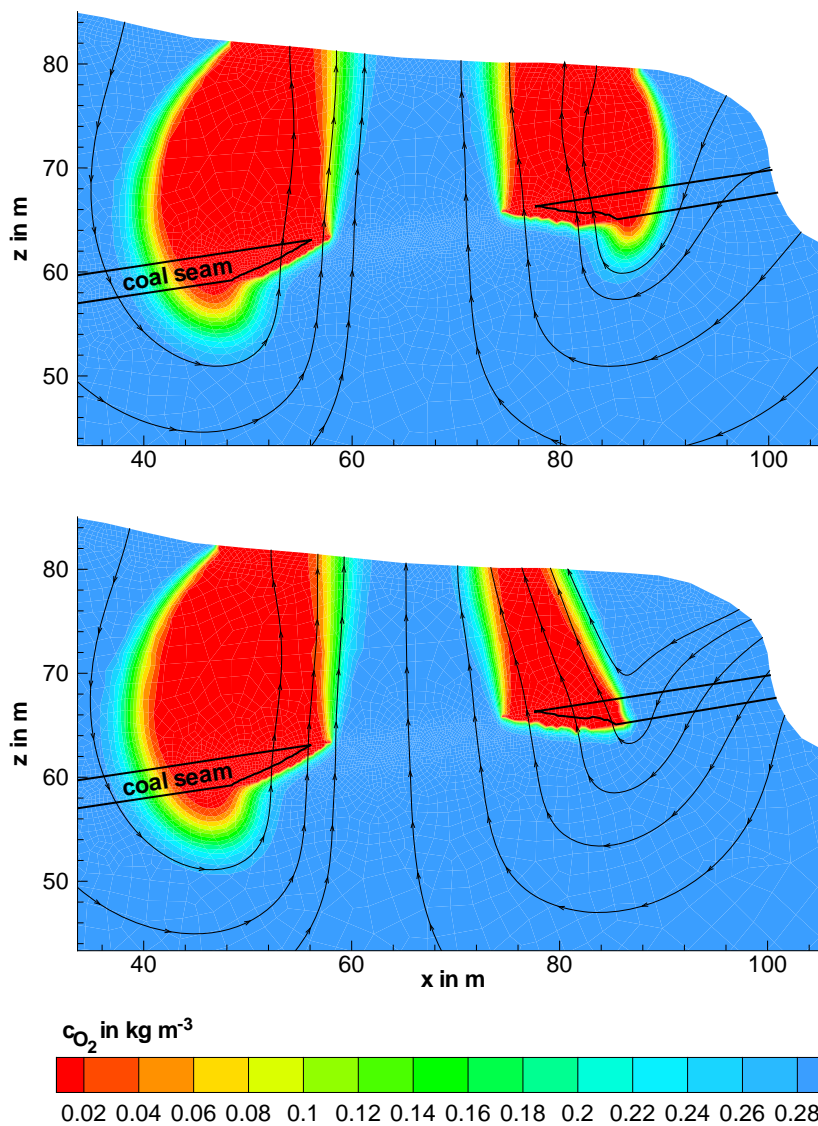


Figure 5.10 Distribution of the oxygen concentration: Without (top) and with (bottom) wind-induced pressure rise at the outcrop

5.3 Conclusions Drawn from System Response Investigations

From the previous investigations, the flow behavior proved to be of highly complex nature. Even though a continuum approach has been used with a homogeneous distribution of macroscopic parameters, the simulations show that atmospheric pressure variations result in a complex system response. Besides of different phase shifts between the pressure and the oxygen concentration at different observation locations, irregular responses were observed

for which an explanation is not obvious.

In addition, winds blowing onto an outcrop proved to affect the flow system. This system likely becomes even more complex when the heterogeneous nature of the overlying beds is included into the model. The circulation of gas in large-scale fracture networks will likely behave much more sensitive to wind. Concluding, the flow pattern developing around an underground coal fire is an overall response to complex internal processes involved due to the coal fire and of external processes in the atmosphere.

This result is important to properly interpret *in-situ* measurements. Single measurements, e.g. of temperature or gas concentrations, may show different values, depending on the measurement time. Conclusions drawn from such measurements to the underground fire situation may become incorrect unless external influences have been extracted from the recorded signals. Therefore, monitoring over longer times is preferential than only collecting data at single times.

Despite the observed complexity, such flow patterns seem to be less significant for the overall combustion process. Neither wind nor atmospheric pressure variations changed significantly the system. E.g., the combustion temperature remained constant under the influence of wind, and the temperature increase (by 6 Kelvin, Fig. 5.8) observed during the influence of atmospheric pressure variations can also be expected without external influences. However, this conclusion can only be drawn for the short time intervals over which the investigations have been performed. Predictions for possible influences over longer times are not possible here.

6 Validation and Calibration Through *In-situ* Measurements

The application of numerical simulations to predict the behavior of a system relies on sufficiently accurate validation and calibration of the model by comparison with *in-situ* observations.

As confusion seems to persist in the definitions of validation and calibration (Konikow and Bredehoeft, 1992), these terms as understood by the author are briefly explained. Validation is defined as the procedure to check the ability of a site-specific model to represent the cause and its impacts at a particular area. Calibration is done by comparing observations of physical values to corresponding values calculated by the model. The calibration procedure includes the varying of parameter values within reasonable ranges until the differences between observed and computed values are minimized. Once consistency is obtained, the matched set of parameter values is taken for prognostic simulations.

Model verification has already been performed in Sec. 3.4, together with the explanation of implemented numerical algorithms.

This chapter is concerned with the comparison between *in-situ* observations and simulation results for model calibration and validation. One fire zone is presented as a test site where *in-situ* measurements were performed during various field trips. A selection of the readings useful for comparison with simulated values are summarized, and validation and calibration possibilities are discussed. Finally, some new methods are proposed for the exploration of underground coal fires by surface measurements.

6.1 Description of the Test Site

The test site for *in-situ* investigations is located in the Shenhua Group Coal Mining Area of Wuda (Distinct Wuhai, Inner Mongolia, PR China, see e.g. Bin and Yi, 1999). The investigations were performed within the framework of the Sino-German Research Initiative "Innovative Technologies for Exploration, Extinction and Monitoring of Coal Fires in North China", which started in May 2003. Since then, intensive research activities were performed to better understand the onset and propagation of coal fires. Results from geophysical, geological and geographical disciplines were combined, including laboratory measurements.

The coal field of Wuda is an isolated outcrop of Permo-Carboniferous strata in the northern part of the Helan Shan (see Hofmann, 1993, for a detailed description of the Helan Shan mountains). A more specific presentation of the geology of the Wuda test site is given in Gielisch and Kahlen (2003), from which some aspects are presented here. The subsurface strata are made up of clastic sediments ranging from claystones, siltstones, sandstones, to conglomeratic sandstones bearing 18 coal seams. Fig. 6.1 presents the general stratigraphy.

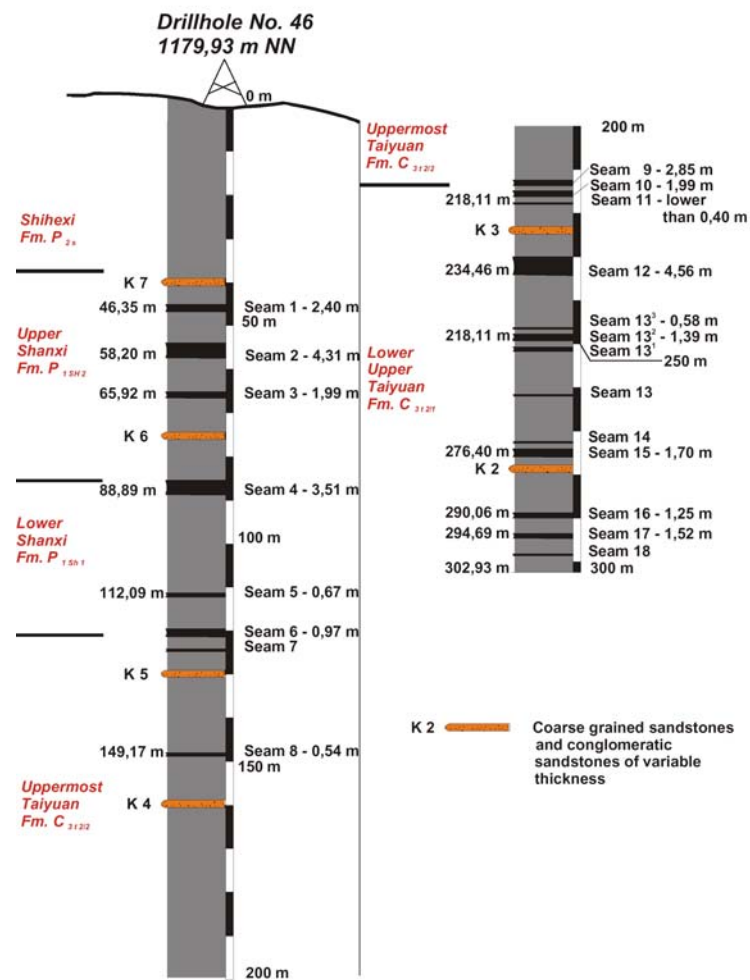


Figure 6.1 General stratigraphy of the Wuda coal mining area, taken from Gielisch and Kahlen (2003)

The sequence forms a syncline, which is cut off in the center of the structure. In the whole area, coal bearing strata are mined by the Wuda Coal Mining Company (Shenhua Group Ltd.) and small private enterprises. In the syncline, more than 17 fire zones are known, with seams burning at the outcrop or below the surface.

The coal rank, a petrographic classifier, determines the degree of diagenesis or coalification that a coal has undergone by burial and tectonic effects. One parameter is the vitrinite reflectance as a measure of the amount of vitrinite contained in the coal. Vitrinite is one of three macerals, which is composed of woody material (Thomas, 2002). The vitrinite reflectance of Wuda coal ranges between 0.83%*Rr* and 1.69%*Rr*, with an average of 0.91%*Rr* (Kus et al., 2006). The carbon concentration of the Wuda coal falls in the range between 84 and 99% (daf=dry and ash free). Wuda coal thus belongs to the coalification

group (the coal rank) of high volatile A bituminous coal (Thomas, 2002; Kus et al., 2006). Following the world trend of coal porosities by Radlinski et al. (2004), Wuda coal exhibits porosities between 3 and 18%. Further coal petrographic characteristics of the Wuda coal are summarized in Dai et al. (2002).

Within the Wuda coal field, Fire Zone 3.2 has been selected as one of the test areas for the Sino-German Research Initiative (Fig. 6.2 presents a satellite image). In that fire zone, seam no. 9 is burning at the outcrop, as least since the begin of the Initiative. Likewise, seam no. 10 is burning, but approximately 10m below the surface. Seam no. 12 (approx. 20m below the surface) was observed to burn since 2004. However, the fire in seam no. 12 was excluded from further investigations, because observation from the surface was difficult.

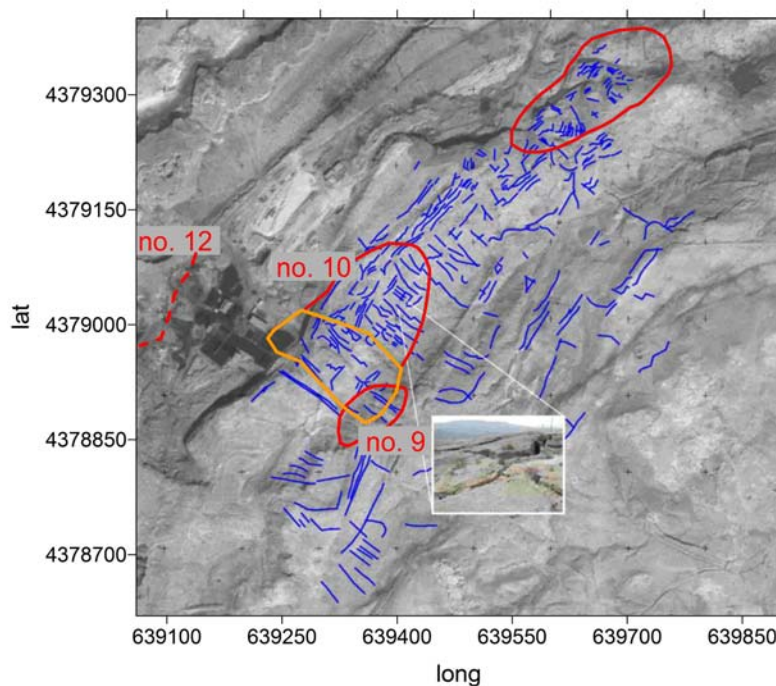


Figure 6.2 Location of coal fires (red polygons) in Fire Zone 3.2 (Wuda). Labels mark the number of the burning seam (for attributes, see Fig. 6.1). Burning areas (solid polygons) were mapped in 2003 by Gielisch and Künzer (2003). The extent and location of the fire in seam no. 12 (dashed line) is estimated according to temperature anomalies at the surface and in boreholes, observed during a field trip in June 2004 (Jia, 2004). The blue pattern represents mapped cracks and crack systems based on Quickbird satellite data from October 2003, the orange polygon marks mine activities in seams no. 12, 13 and 15 (Buhrow et al., 2004b). The satellite image has been kindly permitted by the DFD/DLR (German Remote Sensing Data Center (DFD)/ German Aerospace Center (DLR), Wessling, Germany) and will be used throughout the thesis.

Fig. 6.2 also presents cracks and crack systems in the overlying beds of Fire Zone 3.2. The beds above the burning coal seam no. 10 are intersected by large-scale fractures as can be seen in the inlet. The crack structure has been obtained from interpretation of a satellite image, in combination with *in-situ* mappings (Gielisch and Künzer, 2003). The structure is important for the comparison between *in-situ* measurements and numerical simulation. Particularly, the large-scale fractures are potential migration pathways for gas flow. They will dominate the flow system whenever they are hydraulically connected to the underground combustion centers.

In Fire Zone 3.2, coal is mined in the "Su Hai Tu" underground coal mine (Buhrow et al., 2004b), where digging takes place in seams no. 12, 13 and 15. An approximate location of a mine panel is shown in Fig. 6.2 by the orange polygon. The exact extension of the mine is unknown, due to the permanent closure of the mine drifts (see Fig. 3 in Buhrow et al., 2004b). Nevertheless, still active mining is performed close to Fire Zone 3.2.

Beneath the highly discontinuous structure of the overlying beds, various measurements in that fire zone showed a high heterogeneity in the temperature distribution (Schlömer et al., 2006; Wessling et al., 2006), the gas compositional distribution (Litschke, 2005; Litschke et al., 2006; Schlömer et al., 2006) and flow rates of exhausting combustion gas (Litschke, 2005; Litschke et al., 2006). For investigation into the CO_2 mass flow, Litschke (2005); Litschke et al. (2006) mapped crack systems and performed gas flow and gas concentration measurements. Mapping results of thermally active and inactive crack systems are presented in Fig. 6.3.

Detailed measurements were performed after each crack system was classified into characteristic structures, like cracks, vents, funnels, semi-funnel and sponge-like structures. The mass flow of CO_2 combustion gas has then been measured in two different ways: First, the CO_2 mass flow was determined at all structures of each crack system, and an average CO_2 mass flow value has been calculated. Second, the CO_2 mass flow has been measured at a representative structure of some crack systems only. The obtained CO_2 mass flow values have been taken as representative values for a whole crack system. The uncertainty of the second measurement is the selection of representative structures from visual indicators only (Litschke, 2005).

The individual readings show a high local variability of the CO_2 mass flow within each particular crack system. In addition, a comparison between different crack systems shows that each crack system is different. Hence, a representative crack system is difficult to find.

A comparison between the two types of measurement (detailed and approximate) in two cases gave total CO_2 mass flow values in the same order of magnitude. In three other cases, the CO_2 mass flow values differed by one order of magnitude, depending on the type of measurement. From that comparison, Litschke (2005) suggests to use the first (detailed) method, which is, though time-consuming, more accurate than the second one.

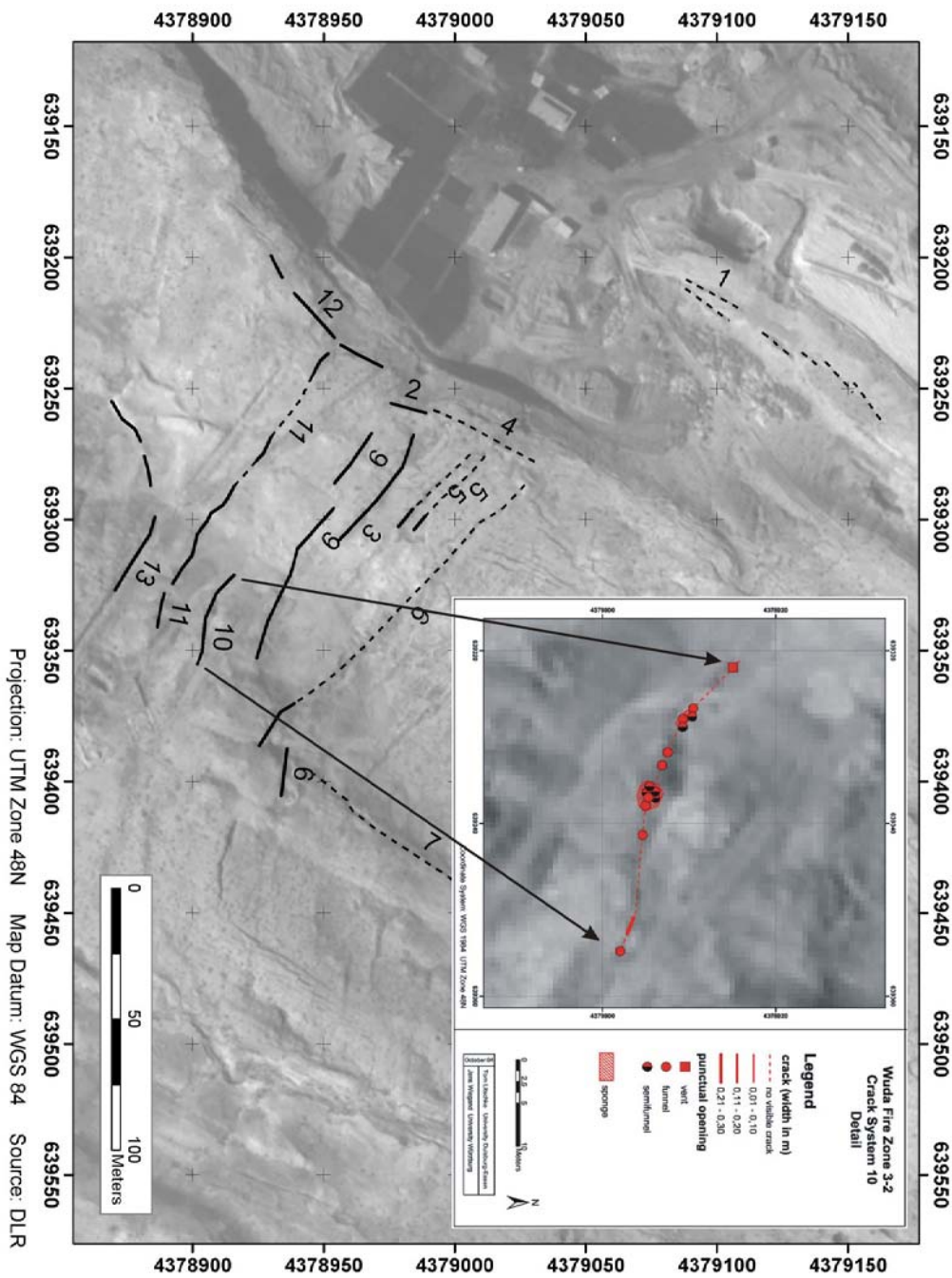


Figure 6.3 Mapped thermally active and inactive crack systems in Fire Zone 3.2 taken from Litschke et al. (2006). Solid lines represent thermally active and dashed lines inactive crack systems. The inset presents details of crack system no. 10, which is subdivided into cracks and punctual openings like vents, funnels, semi-funnels and sponges (see Litschke et al., 2006, for a detailed description of the objects).

Summarizing the above-presented situation at Fire Zone 3.2, *in-situ* investigations reflect a highly heterogeneous nature of the overlying beds. The interpretation of the crack system shows that large-scale discontinuities are a dominant structure in the rock formations, compared to the (small-scale) porous nature of the original beds. The CO_2 mass flow values demonstrate the local variability of gas flow within one crack system, but also the difference between crack systems.

The highly heterogeneous nature poses a serious problem for finding a representative elementary volume as introduced in Sec. 2.1.1. Averaging over large-scale discontinuities to derive macroscopic single- or multi-continua formulations, after which macroscopic variables can be treated homogeneous in the statistical sense, seems extremely difficult unless impossible.

In addition to the problem of finding representative elementary volumes, the flow system in the highly heterogeneous beds is complex due to the unknown connectivity between cracks below the surface, and due to the hardly quantifiable influence of natural external phenomena like weather changes. Concerning the latter aspect, results from Sec. 5 show that even atmospheric pressure variations affect the subsurface circulation behavior.

6.2 *In-situ* Measurements

Many other types of measurements have been performed within the Sino-German Research Initiative, including passive seismics, geophysical investigations (Schaumann et al., 2006), satellite imaging (Tetzlaff, 2004; Zhang, 2004; Kuenzer, 2005; Kuenzer et al., 2007), gas composition (Litschke, 2005; Litschke et al., 2006; Schlömer, 2005), temperature and differential pressure (Kessels et al., 2006b; Wessling et al., 2006) and ventilation (Litschke, 2005; Litschke et al., 2006) measurements. Some of the data can be compared with simulation results and are presented in the following.

6.2.1 Ventilation Measurements

Besides of CO_2 mass flow measurements, Litschke (2005); Litschke et al. (2006) performed ventilation measurements at the crack systems (Fig. 6.3). Ventilation measurements were conducted near the surface by use of emission chambers (see Cardellini et al., 2003, for details) and a pitot-static tube.

Some data are presented in Tab. 6.1 (published in Wessling et al. (2006)). In total, the measurements covered an area of approximately $14,000m^2$. A total flow rate Q of approximately $37,000m^3h^{-1}$ was detected for the exhaust gas. For each structure, the specific flow rate, q in mh^{-1} , can be calculated by dividing the flow rate through the area over which the flow rate has been measured. The measurement results show that the specific flow rate varies over four orders of magnitude between cracks and undisturbed soil. Once again, these measurements prove the high variability of processes taking place in the largely heterogeneous overlying beds.

As a rough approximation an average value for the specific flow rate may be calculated by dividing the total flow rate of $Q = 37,000m^3h^{-1}$ through the area covered by the mea-

surements, yielding a value of $q = 2.7 \text{ m h}^{-1}$. This value needs to be handled with care, because it cannot be regarded as a representative value for any underground coal fire at any time at any location of the domain. Rather, the value is a result of measurements within one short period of time. In addition, the value strongly depends on the size and structure of the measurement area. Increasing that area may or may not significantly change the total flow rate, depending on whether additional large-scale fractures are included into the extended area or not.

Structure class	Average area A in m^2	Average Flow rate Q in $\text{m}^3 \text{ h}^{-1}$	Specific flow rate q in $\text{m}^3 \text{ h}^{-1} \text{ m}^{-2} = \text{m h}^{-1}$
Crack	5	22,456	4,237
Vent	– ^(a)	2,302	–
Funnel	– ^(a)	653	–
Semi-Funnel	– ^(a)	75	–
Sponge	72	1,642	23
Undisturbed soil	13,868	10,022	1
Total	13,945	37,150	

^(a)not determined because too small and therefore irrelevant

Table 6.1 Results of ventilation measurements from Litschke (2005). The data as presented in the table are summarized and published in Wessling et al. (2006). Decimal places have been skipped as irrelevant.

6.2.2 Pressure Measurements

Possible driving forces for gas ventilation are externally imposed pressure differences or pressure differences resulting from thermal buoyancy. In Fire Zone 3.2, prevailing pressure differences between the ambient pressure and the pressure below the surface were measured. The measurements were undertaken in nine boreholes, all cased to a depth of approx. 20 to 25 meters. In that depth, coal seam no. 12 intersects. Hence, the readings reveal information about the possible ventilation system for that seam.

The measurement procedure is illustrated in Fig. 6.4. If air inflow or outflow takes place through the boreholes, a pressure difference must exist as driving force for gas motions. The difference is given between the pressure P_{atm} in the near-surface atmosphere and the pressure P_2 prevailing at the downhole end of the casing. For hydraulic investigations, the boreholes were covered with a steel plate interrupting air inflow or outflow (right hand side

of Fig. 6.4). Consequently, the pressure P_1 at the borehole's top end decreases or increases to a value that must be equal to the pressure P_2 , reduced by the hydrostatic part at the end of the casing: $P_1 = P_2 - P_{hyd}$. Thus, the measurement of the pressure difference between P_{atm} and P_1 yields the dynamic part of the pressure difference that must prevail between the atmosphere and a subsurface level at the downhole end of the casing. As long as the pressure field remains constant over long times, the pressure field is a spatially smoothly varying potential. Accordingly, the determined dynamic pressure differences are not only valid for the boreholes, but also prevail in the far-field around the borehole locations.

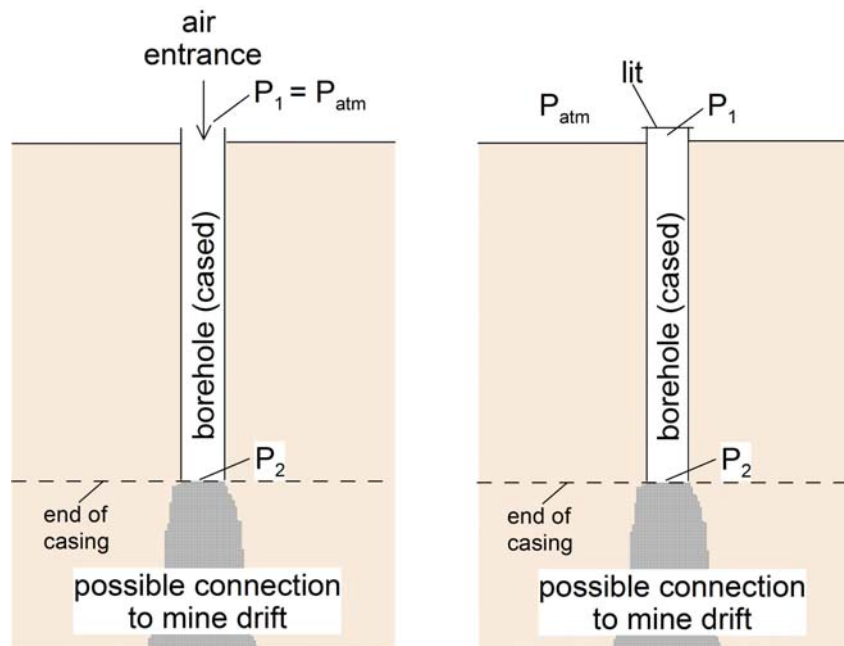


Figure 6.4 Illustration of pressure measurements. P_{atm} is the ambient atmospheric pressure. Left: Cased borehole through which air inflow takes place. Right: Covered borehole, where air entrance is prohibited. The borehole is possibly connected to a mine drift (see Buhrow et al., 2004b, for mine activities in Fire Zone 3.2).

The differences between the ambient pressure and the pressure at approximately 20 meters below the surface range between -0.25 and -2.2 millibar (Fig. 6.5). The negative sign indicates that all wells showed inflowing gas behavior. Two reasons can explain this observation: either pressure differences have been measured which emerge from mine ventilation or pressure differences developed through temperature dependent density variations as a result of thermal (natural) convection. The more likely reason is discussed below, when the measurements are compared with simulation results.

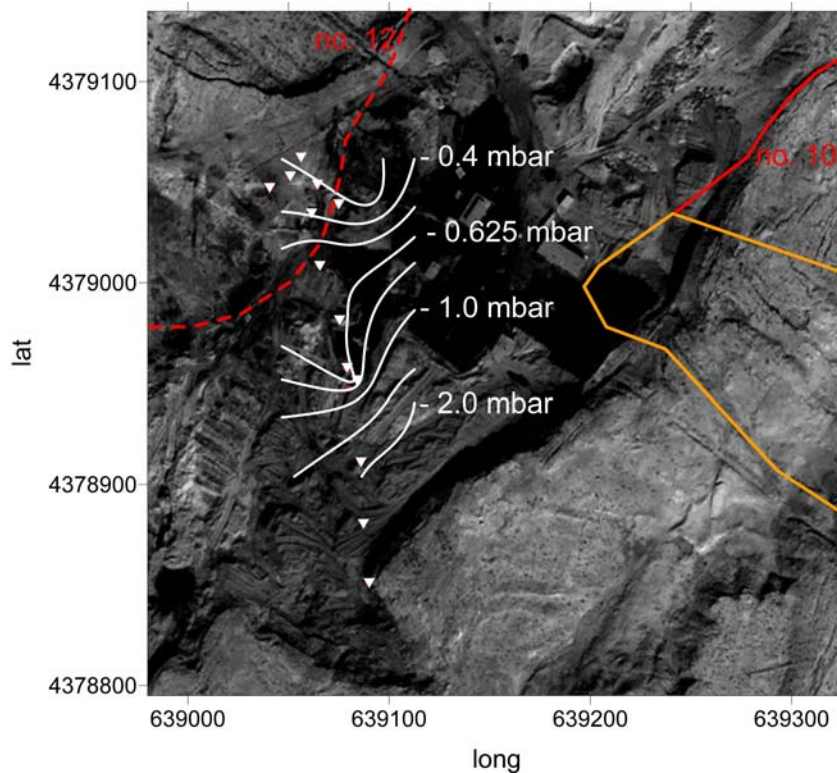


Figure 6.5 Measured pressure differences between the atmosphere and the dynamic pressure prevailing approximately 20 meters below the surface. Triangles show the borehole locations where measurements have been performed.

6.2.3 Temperature Measurements

Temperature was monitored to investigate temporal variations. In addition, measurements were performed at different locations to obtain the spatial temperature distribution above an underground coal fire. Increased temperatures in comparison to the ambient one may be a result of two mechanisms. Either, hot exhaust gas is transported to the surface by convection, or the increased temperature is a result of heat conduction, mainly taking place through the solid rock matrix. This aspect has already been discussed in Sec. 3.5.2, where the simulated energy flux was presented.

Temporal Variations

In Fire Zone 3.2, two sensors were installed for temperature monitoring over some weeks (Fig. 6.6). One sensor has been installed in a small opening at which escaping exhaust gas was visible. The second sensor has also been installed in an opening, but the opening has been closed after installation. Both sensors are located approx. 0.75 m below the surface, a distance of approx. 2 m apart. Due to the depth of installation, daily temperature variations

resulting from solar radiation have likely no influence.

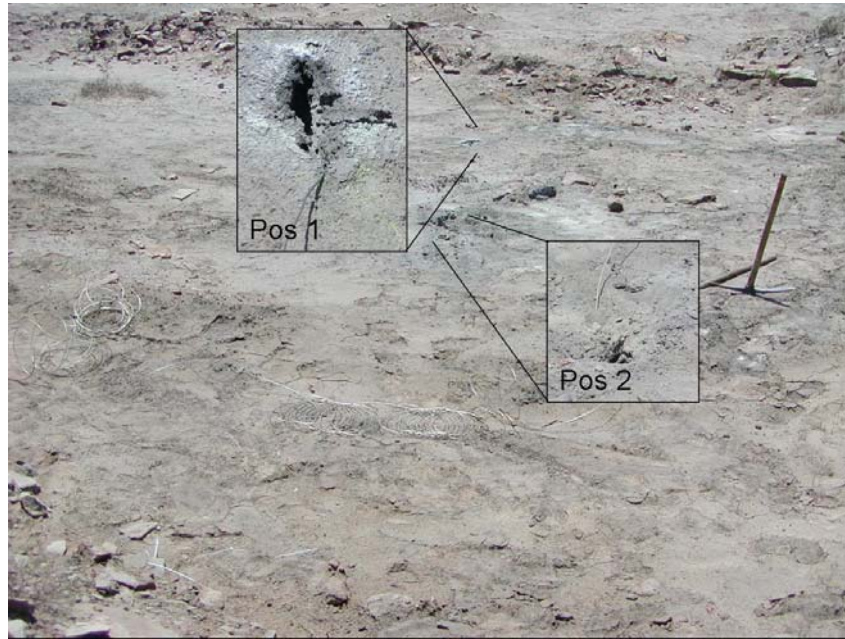


Figure 6.6 Environment for the installation of the temperature sensors in Fire Zone 3.2. The sensors have been installed approx. 0.75 m below the surface. Pos. 1 is the open, Pos. 2 is the covered location.

Fig. 6.7 shows the recorded temperatures. The gas temperature in Pos. 1 behaves slightly increasing (0.3 K per day) at an average value of 725 K and presents daily fluctuations. The increase may result from continuous temperature rise of the bedrock around the opening.

At the covered location, the temperature does not show strong fluctuations. Especially, daily temperature variations are less pronounced than at the open location (compare the inlet in Fig. 6.7). This fact indicates that convective heat transport (cause by gas motions, which is influenced by atmospheric pressure variations, see Sec. 5.1) is weaker at the covered location. The readings from the covered location can be fitted by an exponential function

$$f(t) = A + Be^{-Ct}, \quad (6.1)$$

where $A = 571\text{ K}$, $B = 1.3 \times 10^{-4}\text{ K}$ and $C = 14.8\text{ s}^{-1}$ yield a standard deviation of 0.72 K . Such a function is a solution for the equation of linear flow of heat through an infinite cylinder (Carslaw and Jaeger, 1959, p. 198 ff). The readings can be further analyzed to obtain a temperature distribution around the covered opening, which is yet beyond the scope of this work.

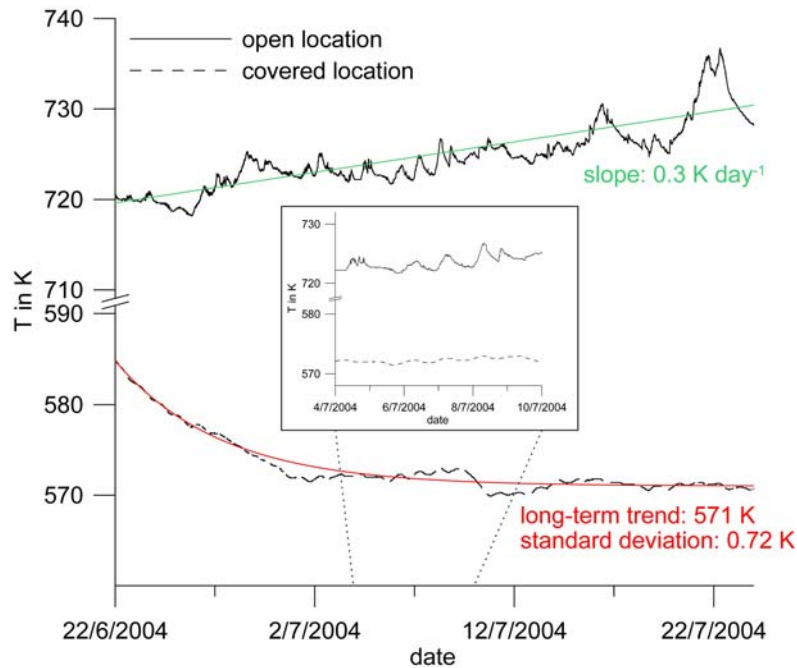


Figure 6.7 Monitored temperatures in the opening (Pos. 1, Fig. 6.6) and in the covered location (Pos. 2). Colored lines represent linear or exponential fits, corresponding slope and standard deviation are given by the labels. The inset shows a section of the readings, to present daily temperature fluctuations.

The exponential temperature decrease results from the (at least partly) interruption of convective heat flow by gas motions. Before coverage, hot gas heated up the rocks around the previous opening. Coverage interrupts gas flow, hence heat decays in the surrounding rocks. The temperature decreases to the one prevailing in the far-field, which is given by the constant $A = 571 \text{ K}$ in Eq. 6.1. This value, still high above the ambient temperature, is thus the temperature of the rocks around the previously open location.

From the temperature behavior at the open and covered locations, the conclusion can be drawn that the spatial variability of overlying beds is also reflected by the temperatures. A distance approx. 2 meters apart, the temperature difference was about 50 K . In addition, the temperature is likely not only increased (compared to the ambient temperature) at locations where hot gas escapes but also at seemingly less permeable locations. Whether convection or conduction is the dominant heat transport mechanism at such less permeable locations cannot be answered, but an influence by convection is observed even at the covered location.

Spatial Variations

The temperature distribution at the near-surface of Fire Zone 3.2 is presented in Fig. 6.8 (Schlömer, 2005). Most temperature values are in the low-temperature range ($T < 353 \text{ K}$), which is close to the average ambient temperature. High temperature anomalies ($T > 453 \text{ K}$) are hardly observed. Also, it cannot be observed that temperatures measured in exhaust gas

are higher than values taken in the soil. It is therefore difficult to estimate the temperature of the underground fire from near-surface temperatures.

In the center of Fire Zone 3.2 the temperature distribution appears to be rather heterogeneous. Especially, the distribution is not smooth, i.e. very hot temperatures are observed close by locations with a rather low temperature.

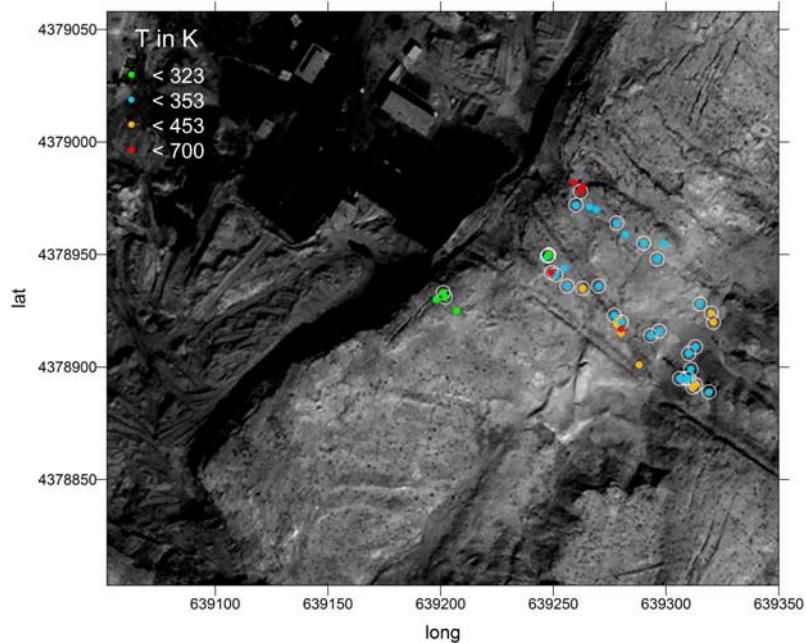


Figure 6.8 Spatial distribution of the near-surface temperature in Fire Zone 3.2 (Schlömer, 2005). The white framed values have been measured in the soil, the others were taken in visible exhaust gas of fractures or other openings.

6.2.4 Gas Compositional Measurements

The composition of the exhaust gas cannot be considered by the numerical model, because only one exhaust gas component is involved in the chemical reaction of Eq. 2.7. In reality, different chemical species like CO_2 , CO or SO_2 are mixed in one single gas phase. Also, convection of involved chemical components (exhaust gas and oxygen) is assumed to be driven by the flow of one single gas phase. Hence, a distinct consideration of component transport within the gas phase is not possible. Due to these simplifying assumptions, measurements of the gas composition are of little relevance for this work.

Some insight may be obtained from measurements of the CO/CO_2 ratio in the exhaust gas, because that ratio characterizes the prevailing combustion mechanism. Either a complete or an incomplete mechanism may proceed at different combustion temperatures (Harju, 1980). Complete combustion takes place when sufficient oxygen is available. In that case, little CO is produced, resulting in a low CO/CO_2 ratio. The temperature of complete combustion is higher compared to that of incomplete combustion, where coal is rather smol-

dering than burning. The incomplete mechanism continues to prevail when an insufficient amount of oxygen is available. Consequently, higher amounts of CO are produced, resulting in an increased CO/CO_2 ratio.

Except for exhaust gas, oxygen is a transported chemical component that is involved in the physico-chemical model. Hence, oxygen measurements may also be used to compare simulation results with *in-situ* measurements. In what follows, results from near-surface measurements of the CO/CO_2 ratio and of the oxygen concentration are presented.

Measurements of the CO/CO_2 Ratio

For Fire Zone 3.2, Fig. 6.9 presents the measurement results of CO/CO_2 ratios (Schlömer, 2005). The distribution of the CO/CO_2 ratio shows a separation into two regions. In the center of Fire Zone 3.2, the ratio is increased in comparison to its north-eastern and south-western parts. Hence, different combustion mechanisms can be attributed to the center and the peripheral zones, respectively. In the peripheral zones with zero to low emitted CO , a complete combustion seems to proceed. In the center part of the fire zone, the seam is more likely smoldering, thereby producing high amounts of CO .

On possible reasons for the development of the zones with different combustion mechanisms can only be speculated. Mining-induced zones with different permeabilities may be one explanation. They may result in different amounts of oxygen inflow. Alternatively, two separate fires may have been developed, which now move towards each other.

From the distribution of the CO/CO_2 ratio, conclusions may be drawn on the temperature distribution in the seam. It may be expected that higher fire temperatures are observed at the peripheral regions than in the central part of Fire Zone 3.2. Then, near-surface measurements of the combustion gas can be used as an indicator for the fire temperature. This option, however, is not reflected in the data of the combustion gas temperature near the surface as a comparison with the spatial temperature distribution shows (Fig. 6.8).

Oxygen Concentration Measurements

Observations of the oxygen (O_2) concentration are presented in Fig. 6.10 (Wessling et al., 2006). The O_2 concentrations range from values close to zero to the O_2 concentration of fresh air ($c_{O_2} = 0.297 \text{ kg m}^{-3}$, four samples).

The data do not allow a clear separation into regions with different oxygen concentration. Instead, the oxygen concentration seems to be randomly distributed over the whole fire zone. It is furthermore unclear, whether gas ventilation takes place below the four sites where samples show O_2 concentration of fresh air. In the absence of gas ventilation, the oxygen concentration of fresh air has been measured. Also, potential mixing with fresh air along the migration path may have corrupted the measured values. Mixing may result from a complex flow pattern within the heterogeneous beds and would increase the oxygen concentration in the exhaust gas. However, such kind of mixing is not observed from the CO/CO_2 ratios. Due to these facts, a rather high uncertainty has to be attributed to the observations of the oxygen concentration.

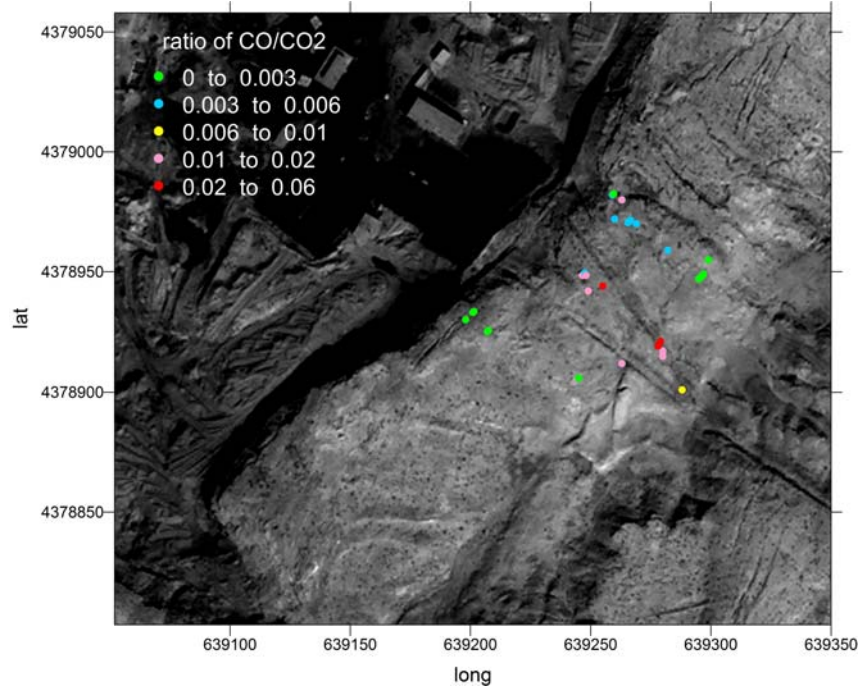


Figure 6.9 Observations of CO/CO_2 ratios in Fire Zone 3.2 by Schlömer (2005)

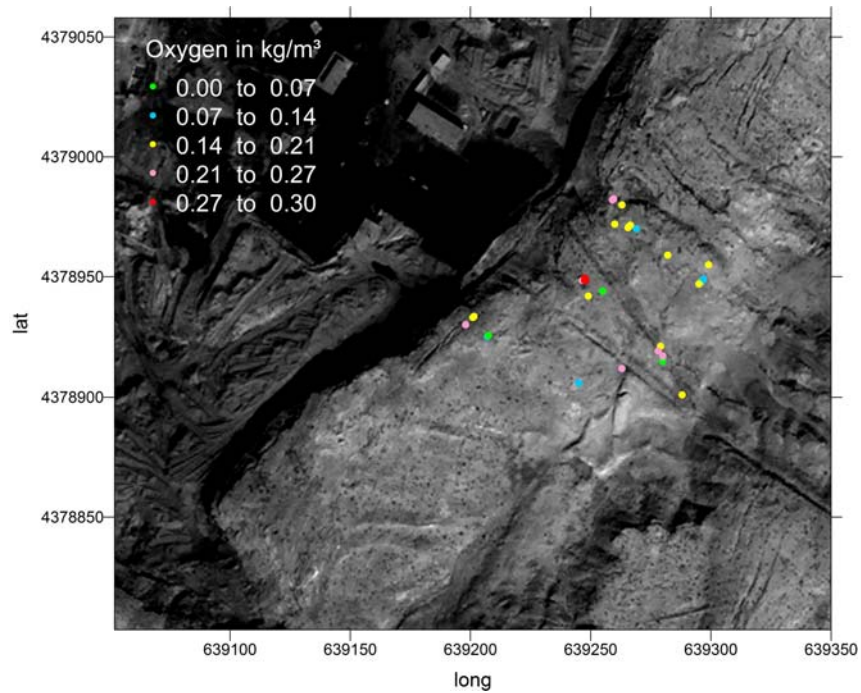


Figure 6.10 Observation of oxygen concentrations above burning coal seam no. 10 in Fire Zone 3.2 (Wessling et al., 2006)

6.3 Validation and Calibration

A comparison between *in-situ* observations from the previous section and simulation results is discussed in the following. The simulation results should reproduce the reality sufficiently well. In the present case, the main difference between model and reality is how fractures are considered. Whereas large-scale fractures are present in the surrounding beds around underground coal fires, the model assumes a porous structure described as a continuum on the macroscopic level. Hence, comparison between simulation results and *in-situ* observations is limited, as will be discussed at the end of this section.

Furthermore, the influence of mines on the ventilation system around coal fires obtained little attention during the field trips. Therefore, the numerical model does not include any mining-induced processes, which yet may be involved in Fire Zone 3.2 (Buhrow et al., 2004b). It may well be possible that mine ventilation causes additional oxygen flow through the system.

6.3.1 Simulation Results Compared to *In-situ* Observations

The following presentation is based on the results of the simulation example (Sec. 3.5) and on results obtained by the sensitivity study in Sec. 4.

Fire Propagation Rate

So far, a direct investigation of the fire propagation rate through an underground coal seam has not been reported. Alternatively, different approaches have previously been performed to conclude on the fire propagation rate from surface indications like visual observations, ground-based monitoring or remote sensing.

The simplest method for the determination of the fire propagation rate is visual observation, i.e. people concerned with the investigation and/or supervision of coal fires estimate the propagation rate after some years of observation. E.g. Nolter and Vice (2004) report about a front advancing approximately 20 meters per year for the Centralia coal fire (Pennsylvania, U.S.).

Prakash et al. (1999) and Prakash and Vekerdy (2004) present an investigation of the underground fire development based on the interpretation of multi-temporal night-time thermal images obtained from remote sensing. Within the Rujigou coalfield (Ninxia Hui Autonomous Region, PR China) Prakash and Vekerdy (2004) classified two fire sites as dynamic (Figures 6 a) and d), p. 114 of Prakash and Vekerdy, 2004), because they are showing a prominent change in their location with time. The progress of the movement has been found to vary depending on several factors, such as the amount of coal available. Therefore, the fire propagation rate has not been quantified. An own estimation based on the same Fig. 6 d), p. 114 of Prakash and Vekerdy (2004) yields maximum values of up to 30 meters per year.

Schlömer et al. (2006) performed long-term monitoring of the temperature of gas exhausting from fractures. He proposes slow propagation rates (< 10 meters per year) for Fire Zone 8 in the Wuda coal mining area. The rates are deduced from temperature decrease or in-

crease at discrete locations, and by a change in the CO/CO_2 ratio.

The above studies or observations confirm a propagation rate of underground coal fires of roughly 10 to 100 meters per year. Simulation results from the sensitivity study (Fig. 4.7) show similar values i.e. between 3 and 340 meters per year. The upper bound is dubious, because the assumed physico-chemical model loses validity at high permeabilities (see discussion in Sec. 4).

Temperature and Specific Flow Rate

Fig. 6.11 shows the temperature distribution around the combustion center (bottom) and the specific flow rate and the temperature at the surface of the domain (top graphs). The figure shows the results at $t = 246$ days of simulation time (beginning from the initial state from the simulation example, Fig. 3.8), with parameters $k = 3.5 \times 10^{-9} m^2$ for the permeability, and $\beta = 5 \times 10^{-8} W m^{-1} K^{-4}$ for the constant in the expression for the effective thermal conductivity.

The temperature field shows two hot combustion centers that propagate in the up- and downward directions through the coal seam. The temperatures in the combustion centers are rather high. Similarly high temperatures (of up to $1300 K$) were observed by Stracher and Taylor (2004). In addition, the CO/CO_2 ratios (Fig. 6.9, p. 100) prove the existence of fire locations, where complete combustion takes place. At these locations, high combustion temperatures can be assumed. However, a separation between fire locations with complete and smoldering combustion (indicated by different combustion temperatures) cannot be deduced from the simulation results.

The simulated surface temperature (Fig. 6.11) is increased to $509 K$ in the center. Similarly increased surface temperatures are well possible at sites where the seam is burning, as has been observed in Fire Zone 3.2 (compare Fig. 6.7, p. 97).

A comparison between the simulated and the *in-situ* observed flow rates is presented in Tab. 6.2. In the model, a gas volume of $72 m^3 h^{-1}$ is released through an area of $50 m^2$. The area is given by the length over which gas leaves the surface, $50 m$, times the depth (one meter) of the two-dimensional model. The depth of the two-dimensional model represents the third dimension, i.e. the "thickness" of a two-dimensional slice (see Sec. 3.5).

A comparison between simulated and observed flow rates shows that the observed flow rate is approximately 500 times larger than the simulated value. Hence, the flow rate of $37,000 m^3 h^{-1}$ would be obtained when the two-dimensional model would be extended to a 500 meter deep slice. For that model a surface area of 50 times $500 m^2 = 25,000 m^2$ would show escaping gas flow, which is of comparable order of magnitude as the investigated area of $14,000 m^2$ from Litschke (2005).

Of course, the fit between simulation and measurements can be improved by changing the permeability, but small changes make an insignificant change in the fire propagation rate (Sec. 4.4). Even a change of the fire propagation rate about some meters per years is not relevant for practical purposes, as *in-situ* determinations are only rough estimations. In addition, the measurements are highly uncertain. E.g., if a crack of one square meter size has not been considered by the measurements (Tab. 6.1), the roughly estimated specific

flow rate q (Tab. 6.2) would change from 2.7 to 3 m h^{-1} .

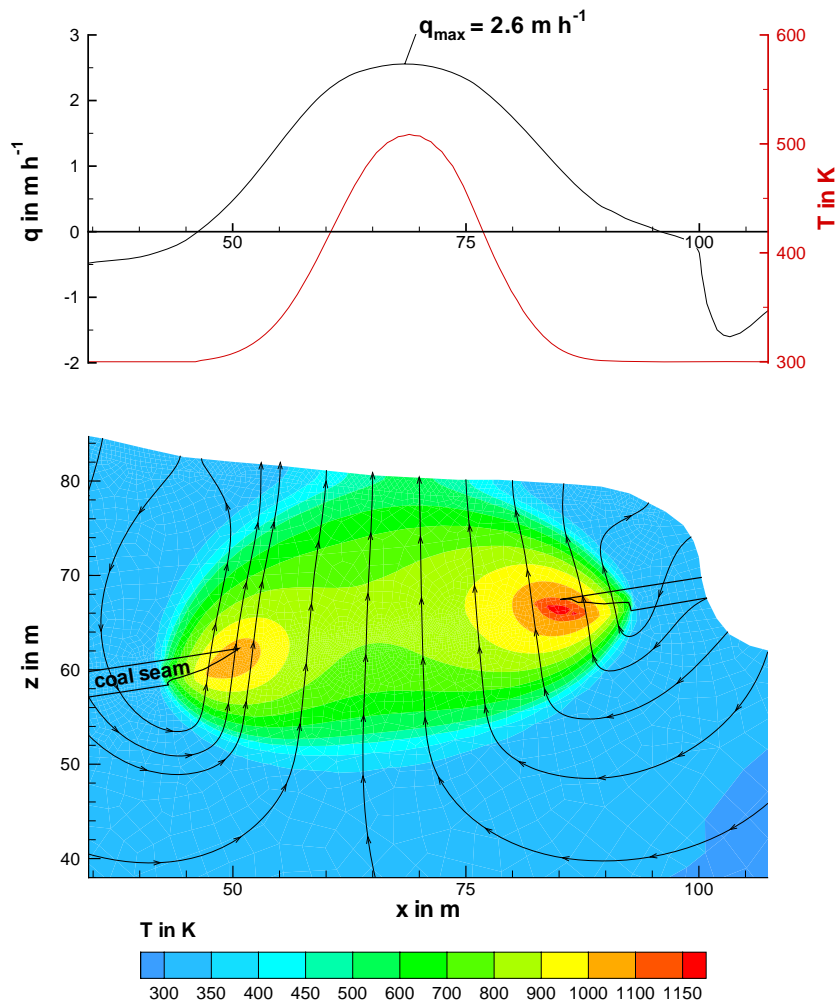


Figure 6.11 Simulation results (246 days of simulation time, beginning from the initial state from the simulation example, Fig. 3.8) with parameters $k = 3.5 \times 10^{-9} \text{ m}^2$ and $\beta = 5 \times 10^{-8} \text{ W m}^{-1} \text{ K}^{-4}$. Bottom: Temperature distribution in the subsurface. Top: Specific flow rate q and temperature T at the surface of the domain.

	simulated	observed by Litschke (2005)
specific flow rate	$2.6 m h^{-1}$ ^(a)	$2.7 m h^{-1}$ ^(b)
area of investigation	$50 m^2$ ^(c)	$14,000 m^2$
flow rate	$72 m^3 h^{-1}$ ^(d)	$37,000 m^3 h^{-1}$

^(a) maximum value

^(b) roughly estimated

^(c) simulated for a slice of 50m length and 1m depth

^(d) integrated along the 50m long surface (Fig. 6.11) where exhaust gas leaves the surface

Table 6.2 Comparison between simulated flow rates and ventilation measurements from Litschke (2005)

Pressure Differences

A further observable is the pressure difference between the atmospheric pressure and the pressure in the subsurface (Fig. 6.5). For comparison, the simulated absolute pressure P_{abs} has been reduced by the hydrostatic pressure P_{hyd} to obtain

$$P_{dyn} = P_{abs} - P_{hyd} = P_{abs} - (P_0(z_0) + \rho_0^f g(z_0 - z)), \quad (6.2)$$

where $\rho_0^f = \rho_0^f(T_0 = 300 K)$ and $g = 9.81 m s^{-2}$. The simulated pressure field is presented in Fig. 6.12 for two simulation times, 246 days (left) and 585 days (right). The pressure varies between -0.4 and $+0.06 mbar$, which can be regarded as an average pressure range giving rise to gas motions by thermal buoyancy. Note the seemingly wrong flow direction against the pressure gradient. In z -direction a calculated pressure gradient from the pressure field (Fig. 6.12) cannot be considered as the driving force for gas motions, because the dynamic pressure is superimposed by the temperature dependent hydrostatic pressure. This problem is discussed in more detail in App. C.

A comparison of the simulated (Fig. 6.12) and the measured (Fig. 6.5) pressure shows that measured values are about one order of magnitude larger than the simulated ones. These different observations are interpreted as resulting from different driving forces for gas motions. The only driving mechanism in the model is thermal buoyancy, hence the simulated pressure corresponds to a situation where no externally imposed pressure difference exists. Therefore, the high pressure differences in Fire Zone 3.2 cannot result from thermal buoyancy only. Instead, the high values are believed to be a result of mine ventilation (forced convection).

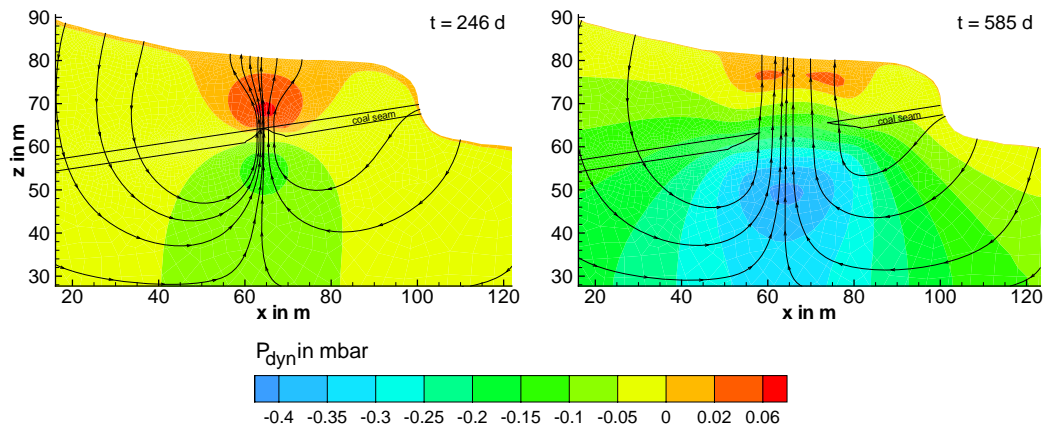


Figure 6.12 Distribution of the dynamic pressure after 246 days (left) and 585 days (right)

Distribution of the Oxygen Concentration

To better understand the observed oxygen concentrations, more information about the flow characteristics are necessary, e.g. whether values have been measured in pure exhaust gas or in gas mixed with fresh air. For the latter case, an interpretation is extremely difficult, because the mixing procedure within the discontinuous subsurface system is hard to grasp. Hence, the observations should not be used for model calibration. However, the four sample locations where the oxygen concentration of fresh air has been detected suggest to investigate the progress of the coal fire by surface measurements.

The idea comes from the simulation results (Fig. 6.13) for two consecutive times with a delay of 340 days. The contour plots show the oxygen concentration as a result of gas flow through the over- and underlying beds. Streamlines represent the flow direction, hence surface locations with in- and outflowing gas behavior can be distinguished from the streamline directions at the surface. The left figure shows the situation at which the coal seam has not yet fully burned out in the center. 340 days later, the coal seam here has burnt out, and the combustion centers spread along the seam in the down- and upward direction. As a consequence, high amounts of energy have accumulated in the surrounding rock formations (see Fig. 6.11 for temperature distributions when the combustion centers have spread out). Hence, thermal convection continues, although energy release from the underground combustion stopped due to the depleted fuel.

Most remarkably, as long as the coal seam has not completely burned out in the vertical, zero oxygen concentration is observed at locations where gas leaves the surface. After the fire breakthrough (the right figure) oxygen consumption stops due to the lack of fuel. The consequence is a recovery in oxygen concentration in the outflowing gas, varying between zero and the full concentration prevailing in air (0.29 kg m^{-3}).

The prediction of continuing gas flow due to temperature differences between the ambience and the underground, although fuel has depleted, is reasonable for the considered model, but requires experimental verifications.

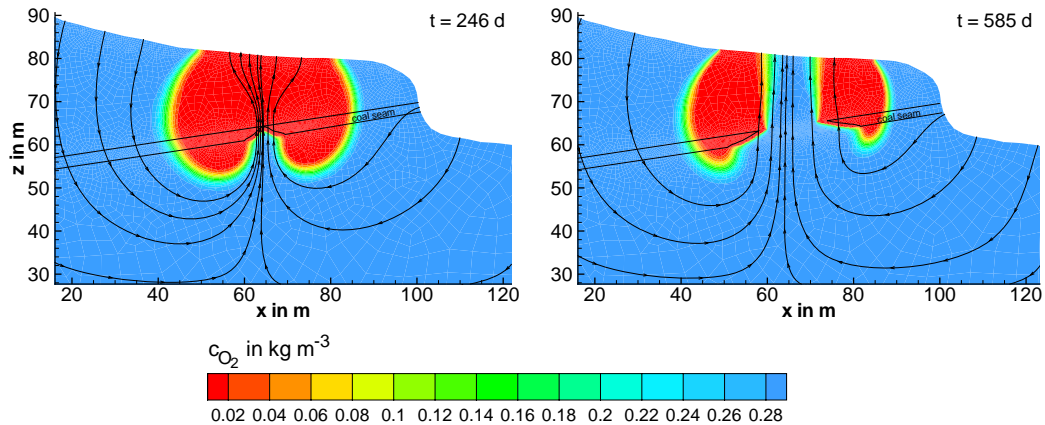


Figure 6.13 Simulation of the changes in oxygen concentration from 246 days (left) to 586 days (right). Initial conditions see Fig. 3.8.

6.3.2 Discussion on Calibration Possibilities and Limitations

After the presentation of simulation and measurement results, possibilities and limitations for model validation and calibration are discussed.

Validation

Some results obtained from numerical simulation have been presented which can be compared with *in-situ* observations and literature values, in particular the fire propagation rate, the temperature and the specific flow rate. These quantities came out in a reasonable order of magnitude, as the comparison with shows. Thus, the numerical model can be considered as validated, because properties of really existing underground coal fires can be reproduced by the simulation.

Calibration

Model calibration requires some discussion from both the simulation's and the measurement's point of view. The main problem for calibration results from the difference between the homogeneous model and the heterogeneous overlying beds (the heterogeneity is not only an attribute of Fire Zone 3.2, but is observed for many underground coal fires). From the measurement's point of view, the following difficulties arise:

1. A proper representative description for the crack systems from only visual indicators is limited and can result in errors, as has been observed by Litschke (2005). A representative description requires time-consuming, detailed measurements, whereas statistically representative information is only ensured for a sufficient amount of measurement values. Thus, either detailed, time consuming measurements are performed,

or uncertain values are obtained from simplified measurement approaches or insufficient numbers of measurement values. An open question is whether statistically representative information can be obtained for such highly heterogeneous systems.

2. The relevance of mining activities in Fire Zone 3.2 is hardly known. Neither the influence of mine ventilation on the gas circulation system nor the influence of rock mechanical failure have been investigated in detail, so that no sound conclusions can be drawn for Fire Zone 3.2.
3. Most measurements show a heterogeneous distribution. The CO/CO_2 ratio seems to be the only quantity from which Fire Zone 3.2 can be divided into different zones.
4. Partly confusing observations have been made by the *in-situ* measurements. The definition of zones with different CO/CO_2 ratio has not been reflected by the spatial temperature distribution at the surface. Furthermore, the measured temperature values are in contrast to temperatures expected from the interpretation of the CO/CO_2 ratio.
5. Finally, the influence of weather conditions on the flow behavior is still unclear for Fire Zone 3.2 (Litschke, 2005; Schlömer et al., 2006).

Summarizing, the complexity and heterogeneity of Fire Zone 3.2 does not allow a division into a few sub-zones with average physical quantities.

Moreover, the numerical model needs to be improved to allow for model calibration by means of *in-situ* measurements. Such improvements should be:

1. Using a hybrid approach to represent large-scale heterogeneities (fractures). A further extension is a model in which the permeability is statistically distributed. Simulation results from such a model can be better calibrated with statistically distributed measurement values.
2. Involving distinguishable combustion gases, especially CO and CO_2 , into the physico-chemical model gives additional calibration possibilities.
3. Once the mining situation in Fire Zone 3.2 is known, mine ventilation and developing large-scale fractures due to mechanical failure can be included.
4. A three dimensional model allows to properly assign measurement results. In addition, the stratigraphy of Fire Zone 3.2 can be included to investigate its influence.

So far, model calibration could not be achieved, due to the heterogeneous nature of Fire Zone 3.2 and the simplifications assumed for the numerical model. Further research is required to find proper upscaling approaches.

6.3.3 Possible Innovative Approaches for Coal Fire Exploration

Despite the difficult task of model calibration, the comparison between simulation results and *in-situ* observations gives rise to methods for the exploration of underground coal fires.

Measurements of pressure differences between the atmosphere and any subsurface level

inform about the driving mechanism for gas motions underground. Pressure differences higher than expected from thermal buoyancy likely originate from mine ventilation. If so, coal seams are supplied with additional oxygen, hence even intact seams are exposed to the danger of self-ignition. Simple measurements of pressure differences can thus help to prevent from ignition of unwanted fires.

A further innovative approach would be to measure the oxygen concentration in escaping exhaust gas. If the observation of high oxygen concentrations (near to the value of fresh air) proves to be realistic (Sec. 6.3.1), measurements of the oxygen concentration are an effective means to detect fuel-depleted locations within the seam by observations at the surface.

7 Simulation of Extinction Scenarios

Numerical simulations are finally applied to investigate the influence of extinction activities on the dynamic behavior of underground coal fires. Similar applications are essential for coal mining industries to develop efficient extinction strategies.

Extinction is performed by eliminating at least one of three conditions necessary for fire sustainment, i.e. the elimination of oxygen, of coal, and the reduction of heat generation by active cooling. In China, frequently applied extinction activities are the injection of water-plus-additives mixtures, as well as surface coverage with fine-grained, nearly impermeable material (Gielisch and Barth, 2003; Buhrow et al., 2004a). Water injection is performed to cool down the heated system in and around the combustion center, stopping further exothermic reactions. Surface coverage prevents oxygen entrance and thus quenches the fire.

The purpose of this chapter is to provide a perspective how simulation scenarios help to develop efficient extinction strategies. Two scenarios will be discussed: Extinction by surface coverage and extinction by water injection.

7.1 Simulations of Surface Coverage

The first extinction scenario deals with the interruption of oxygen supply by surface coverage with nearly impermeable material. Such material may be fine-grained sands or clay, whereas the latter one has the disadvantage of becoming brittle when getting dry. Of course, such extinction strategy presumes the penetration of oxygen from the surface. Otherwise, extended models need to be used.

For the simulation, the model from Sec. 3.5 (Fig. 3.8, p. 52) has been extended by a layer of two meter thickness at the top (Fig. 7.1). For this layer, a permeability of $k = 10^{-18} m^2$ is assumed as a typical value for clay (Guéguen and Palciauskas, 1994). The layer represents a hydraulic resistance (Bear and Bachmat, 1990)

$$r_h = \frac{l}{K} = \frac{l}{k/\mu} \quad (7.1)$$

of $r_h = 3.6 \times 10^{13} kg m^{-2} s^{-2}$ for gas flow through the surface.

The outcrops as well as the surface below the outcrop were not covered, in order to investigate such situations. With this model, the coal fire simulation has been continued, beginning with the situation from the top of Fig. 3.10 (p. 55) as initial state. Thus, the setup assumes the surface coverage after the coal fire burned for 246 days already.

Simulation results are shown in Fig. 7.1, after a simulation time of 521 days. Effects are thus regarded after the coal fire burned for further 275 days, with and without surface coverage. The figure gives a comparison between the unchanged model from the simulation example and the model including surface coverage.

The streamlines (representing gas flow direction) show that surface coverage interrupts oxygen penetration to the downward moving combustion center, where gas is now entirely circulating in the subsurface. In contrast, oxygen penetration through the uncovered surface area still supplies the upward moving fire. Escaping exhaust gas takes an extended way through the outcrop.

Surface coverage decreases the maximum temperature from $T_{max} = 1281 K$ (left figure) to $T_{max} = 917 K$ (right figure). Likewise, the fire propagation rate becomes lower as an effect of surface coverage (compare the isolines for coal concentration in Fig. 7.1). Compared to the initial temperature field (the one after 246 days, Fig. 3.10) with a maximum temperature of $T_{max} = 1111 K$, coverage reduced the maximum temperature by about $\Delta T_{max} = 194 K$. In contrast, the maximum temperature increases by about $\Delta T_{max} = 170 K$ without coverage.

These observations prove that oxygen supply may take place along a large surface area, particularly at surface locations (like outcrops) which are difficult to cover from the operational point of view. Additionally, oxygen supply may take place at surfaces which are not intuitively related to a specific coal fire (like the surface below the outcrop). Coverage of only the immediate surface above coal fires is obviously not sufficient to interrupt oxygen supply. Further scenario simulations with varying size of the covered surface area will give insight into the minimum extent required for a successful prevention of oxygen supply through the surface.

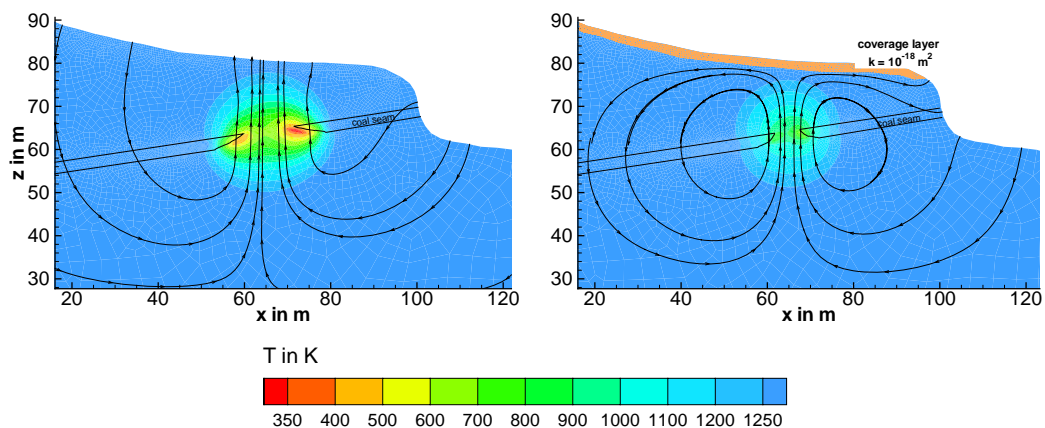


Figure 7.1 Comparison of the temperature and the coal distribution after surface coverage, simulation time is 521 days. Left: Unchanged situation; Right: Surface coverage with a layer of two meter thickness (permeability $k = 10^{-18} m^2$), hence a hydraulic resistivity of $r_h = 3.6 \times 10^{13} kg m^{-2} s^{-2}$ (cf. Eq. 7.1) is obtained. Isolines mark the coal concentration of $c_f = 850 kg m^{-3}$, streamlines represent the flow paths of gas.

7.2 Injection Simulation

A second extinction strategy is the injection of water into combustion centers in order to extract heat. After a brief explanation of *in-situ* observed extinction activities, simulation

results of a water injection scenario are discussed.

7.2.1 *In-Situ* Injection Activities

On June 25th, 2004 fire fighting activities were performed in Fire Zone 3.2, intending to protect mining activities against a fire front moving towards the mine shafts. One drilling master and different workers were met and interviewed about their present work (Jia, 2004).

The applied fire fighting procedure can be summarized as follows: A mixture of water and sand was injected into a gallery of boreholes (see Figs. 7.2 for an impression). The only driving force for water inlet was gravity, without active pumping. Water inlet took place over some days until the borehole was plugged, with flow rates of up to $50\text{m}^3\text{h}^{-1}$ and ca. $330\text{m}^3\text{day}^{-1}$. When one borehole was plugged, inlet was continued at the next borehole.

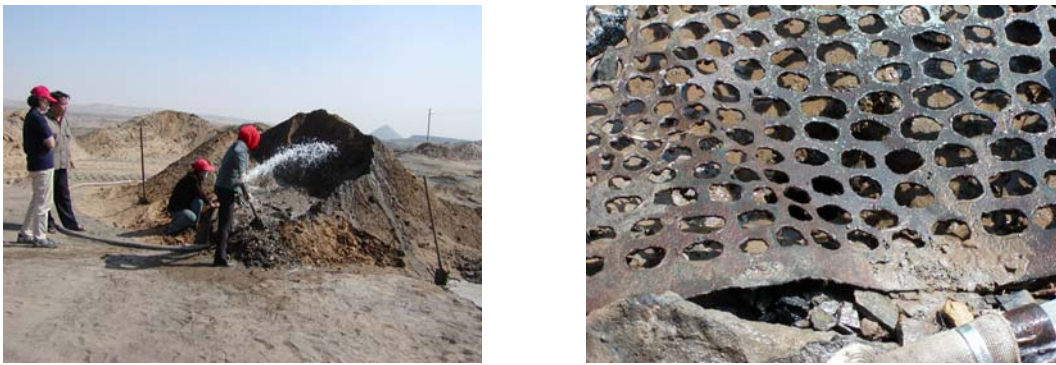


Figure 7.2 Extinction activities observed in Fire Zone 3.2 of the Wuda Coal Mining Area. Left: Preparation of water-mud mixture. Right: Sieve above the borehole, to ensure continuous injection.

The previously described extinction procedure may implicate some uncertainties which can be minimized through the application of scenario simulations. Whenever large-scale cavities exist due to the consumption of coal, passive water injection (driven by gravity only) will fill these cavities. Less permeable material like rock blocks containing small-scale pores are not passed through by the injection water, because the fluid chooses the path of lowest resistivity. As a consequence, only hot (coal or rock) material nearby the cavities is cooled. However, an enormous amount of thermal energy is likely stored in the solid, less permeable rock surrounding the coal fire (compare the large extent of the temperature fields in Fig. 3.10, p. 55). Of course, the temperature field around a coal fire depends on the time over which energy is released, so that heat is transported into the relatively fine-grained solid by heat conduction/radiation (convection is likely unimportant in fine-grained rock). But, once burning for more than a couple of months, fine-grained rocks around the coal fire store thermal energy. This thermal energy is not removed by water injection into the large-scale cavities, if water injection is only performed over some days. Furthermore, a difficulty for injection operations is to define an appropriate distance between boreholes, which should be sufficiently small to remove heat, but also as large as possible to reduce

drilling costs.

The discussed difficulties argue for the use of scenario simulations to investigate the efficiency of water injection activities. Scenario simulations may help to develop optimized borehole distances and duration times for water injection in order to guarantee sustained extinction success.

7.2.2 Model and Setup

The purpose of the presented scenario simulation is to demonstrate the above-stated difficulties arising from water injection into large-scale cavities. Therefore, simulations are performed based on a model sub-divided into a highly disturbed and an undisturbed domain (Fig. 7.3). Such kind of disturbed region results from mechanical failure (Buhrow et al., 2004a). Two locations (a and b) are assumed for water injection. The first location is placed in the combustion center of the downward moving fire, thus in the disturbed region. The second location is placed in the (undisturbed) coal seam in front of the combustion center. Of course, proper positioning of the injection locations presumes at least an approximate picture of the underground situation, which may be obtainable from geophysical investigations (see e.g. Schaumann et al. (2006); King (1987), Sternberg and Lippincott (2004) for previous attempts on geophysical investigations of underground coal fire locations).

Note that the setup represents a two-dimensional slice of one meter thickness (cf. Sec. 3.5). Hence, water injection is not represented by a point source for this model. Rather, the model assumes water injection within a lateral layer, which may be considered as a 'cooling wall'. In reality, locations for water injection will likely not be placed such dense as to represent a 'cooling wall'. Therefore, a more realistic simulation of water injection activities requires a three-dimensional setup.

The scenario simulations are based on the previously described physico-chemical model (cf. Fig. 2.3 on page 16), which has been chosen for simulation without external influences. Thus, processes relevant for systems containing water are not involved. Particularly, two-phase flow for water and gas cannot be considered. An application of this model for simulation of water injection thus presumes the following simplifications:

- Chemical reactions between coal and fluidal species contained in water and/or gas are omitted.
- The generation of latent heat due to the phase transformation of water to vapor is not considered.
- Due to its high heat capacity, water is an effective fluid for the transportation of heat. Therefore, water is assumed as the only fluid. Two-phase flow (including capillary forces) and the conversions between water and gas are not taken into account.
- For a proper calculation of water hydraulics, the whole domain is assumed to be flooded with water.

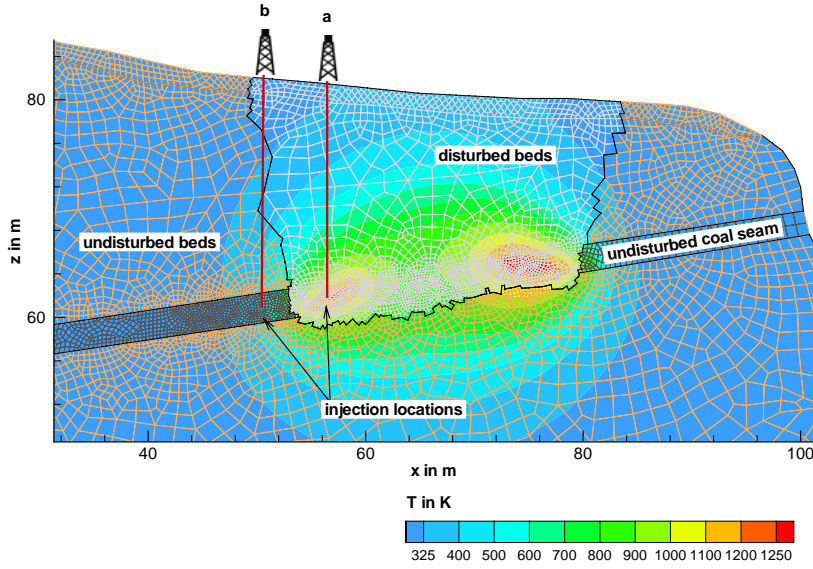


Figure 7.3 Setup for the simulation of a water injection scenario. Two injection locations are assumed, a and b. The domain of investigation is divided into undisturbed seam and beds, and disturbed beds due to mechanical failure.

- The fluid density is assumed to be constant, hence thermal buoyancy is not involved. Instead, the driving force for water flow results solely from injection. Injection is realized by an external source Q_V in $m^3 s^{-1}$ for the water phase, which can be considered as a volume production rate.
- Flow velocities of water are assumed sufficiently small, so that Darcy's law applies.

With the above assumptions, the physico-chemical setup is described by the hydraulics equation for constant density (Eq. 2.17 extended by the external source and assuming constant density)

$$S \frac{\partial P}{\partial t} + \nabla \cdot \mathbf{q} + V^{-1} Q_V = 0, \quad (7.2)$$

and Darcy's law without the buoyancy term (Eq. 2.20). The energy conservation equation for porous media (Eq. 2.28), omitting radiant heat transport, reads:

$$c^b \frac{\partial T}{\partial t} + \rho^f c_p^f \mathbf{q} \cdot \nabla T - \lambda_0 \nabla^2 T = 0. \quad (7.3)$$

In Eq. 7.2, V in m^3 is the volume occupied by the source. Although being a strongly simplified model, the development of the temperature field can roughly be investigated. Emphasis is put on cooling effects when sub-regions with different degree of disturbance exist. Thus, rather than trying to simulate extinction activities based on extinction-relevant processes, the presented scenario simulations will give a perspective for future developments and applications.

Parameters used for the scenario simulation are given in Tables 7.1 and 7.2. Numerically,

injection is realized by inserting a volume-production source of $Q_V = 6.7 \times 10^{-4} \text{ m}^3 \text{ s}^{-1} \text{ m}^{-1} = 40 \text{ l min}^{-1} \text{ m}^{-1}$ into the injection locations. The unit of Q_V in $\text{m}^3 \text{ s}^{-1} \text{ m}^{-1}$ stems from the two-dimensional setup with a lateral extension of one meter. The used injection rate is typical for fire safety tubes. Further parameter studies will help to investigate the influence of the injection rate to the extinction efficiency. A constant temperature of $T = 300 \text{ K}$ has been set as Dirichlet boundary condition at the injection point, to realize the injection of cold water.

Parameter	Value			Unit
	undisturbed bed	disturbed region	undisturbed seam	
c^b	2.4×10^5	2.4×10^5	3.06×10^5	$\text{J m}^{-3} \text{ K}^{-1}$
k	10^{-11}	10^{-9}	10^{-11}	m^2
S		10^{-11}		Pa^{-1}
λ_0	2.0	2.0	0.1	$\text{W m}^{-1} \text{ K}^{-1}$
Φ	0.2	0.4	0.4	–

Table 7.1 Parameters for the simulation of the water injection scenario. Single, centered values are assumed for the whole domain.

Parameter	Value	Unit
c_p^f	4200	$\text{J kg}^{-1} \text{ K}^{-1}$
Q_V	6.7×10^{-4}	$\text{m}^3 \text{ s}^{-1} \text{ m}^{-1}$
μ	2.5×10^{-4}	Pa s
ρ^f	1000	kg m^{-3}

Table 7.2 Water-specific parameters for the simulation of the injection scenario (see e.g. VDI-Wärmeatlas, 2002)

7.2.3 Simulation Results

The simulation results are presented in Fig. 7.4, where the temperature distribution is shown after an injection time of 40 hours, i.e. after a volume of $V = 9600 \text{ l} = 9.6 \text{ m}^3$ has been injected. The figure demonstrates the difference between water injection into and in front of the combustion center. After water injection into location 'a' (the disturbed region), the temperature in the undisturbed coal seam remains nearly untouched, because injected water mainly moves through the disturbed, highly-permeable region. In contrast, water injection

in front of the combustion center first propagates through the undisturbed seam, thereby removing heat in that region. Afterwards, injected water reaches the disturbed region, and therefore continues to extract energy from the combustion center.

Of course, the disturbed region is, after 40 hours, less cooled when water is injected into location 'b', but a longer injection time would likewise cool the disturbed region from the right of Fig. 7.4. In addition, the location with still high temperature (right of Fig. 7.4) is irrelevant for the estimation of re-ignition problems, as coal has already been consumed there.

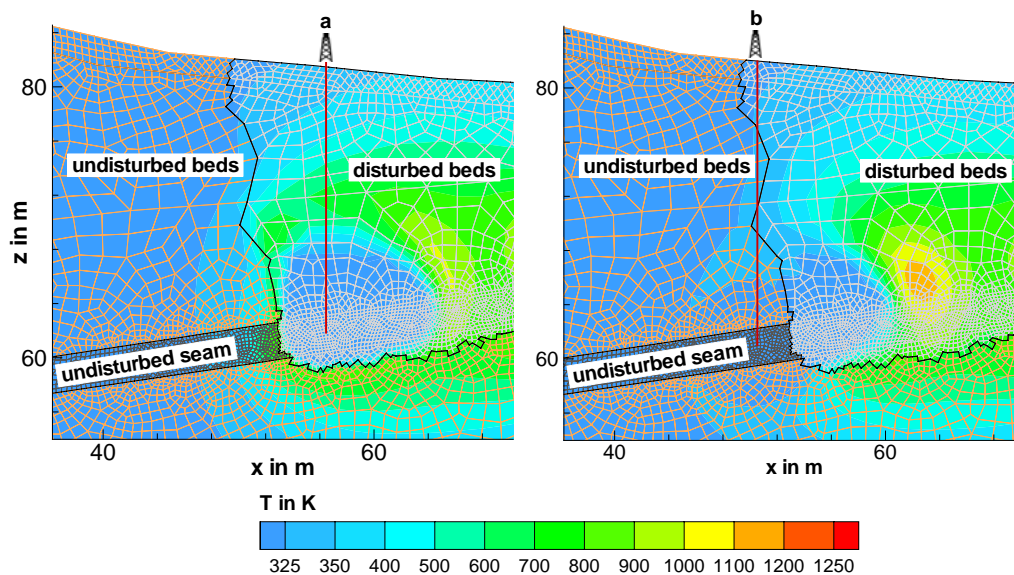


Figure 7.4 Simulation results after 40 hours of water injection into the heated system from Fig. 7.3. Left: Injection into the downward combustion center (location a, Fig. 7.3). Right: Injection in front of the downward combustion center (location b, Fig. 7.3).

7.2.4 Evolution of Temperature After Injection

Simulation results from Fig. 7.4 show that the injection of water into the disturbed region is insufficient to thoroughly cool the undisturbed material, because water does not penetrate into the undisturbed region. In contrast, injection in front of the combustion center first cools the undisturbed region, before reaching the combustion center.

It is further important how the temperature field after water injection behaves. Energy remaining in the rock material decays by thermal conduction (presuming interruption of convective fluid motions), hence previously cooled locations will heat up again. Consequently, reactive coal material may re-ignite.

Fig. 7.5 shows the temperature distribution which developed 30 days after water injection

stopped. The left figure shows that, 30 days after water injection, the undisturbed coal seam is still heated up, hence re-ignition may set in there. The right figure shows that the reactive coal seam is not re-heated due to the decay of the temperature field, at least not after 30 days.

Due to the assumed simplifications, conclusions about possible re-ignition are limited. The simulation over a time longer than 30 days is senseless, because additional processes need to be considered. The next section briefly describes extension possibilities to obtain a more realistic physico-chemical model for the simulation of extinction activities by water injection.

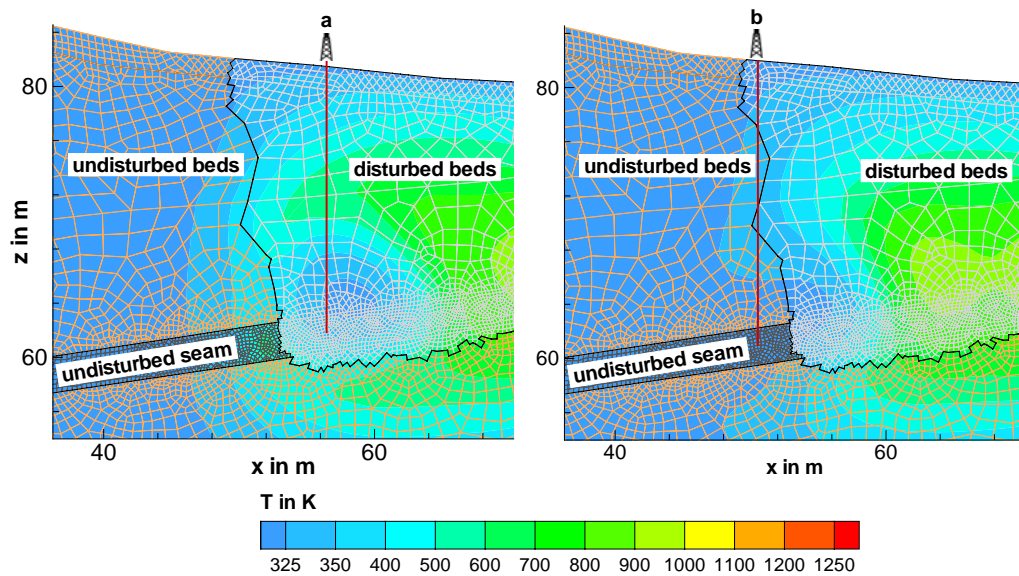


Figure 7.5 Temperature distribution 30 days after the end of water injection into (left) and in front of (right) the downward combustion center

7.2.5 Improvements of the Setup

Finally, proposals are given to improve the simulation of water injection scenarios and to investigate the long-term behavior of the coal fire system after injection. The proposals are sub-divided into two categories: one considering fluid-dynamic aspects and a second one considering rock-mechanical aspects. Fluid-dynamic aspects are:

- Due to the co-existence of water and gas during water injection, an approach considering two-phase flow seems more appropriate than the consideration of only one fluid phase.
- Consideration of water evaporation when exposed to high temperatures, as well as

condensation in sufficiently cool surrounding rocks will involve the consideration of energy transport processes by vapor flow.

- For the consideration of self- or re-heating effects, the release of heat of absorption can get relevant, so that this effect should be included into the conservation equation for thermal energy. Lohrer (2006) experimentally showed that the self-heating tendency may increase when coal accumulations are watered or exposed to rapidly increasing humidity. This fact results from the release of heat during the absorption of water molecules by the coal.

Rock-mechanical aspects to improve the simulation of extinction scenarios may be summarized as follows:

- Rock mechanical simulations may be performed to predict the extent of disturbed regions. Such simulations will help to show preferential path ways for fluid flow. Consequently, insufficiently cooled locations can be found out, and the importance of such locations to the danger of re-ignition can be investigated. Difficulties may arise when hydraulic parameters are extracted from rock-mechanical results.
- Once regions with different degree of disturbance are obtained from rock-mechanical calculations the simulation of heat extraction may be improved using a multi-continua approach for energy transport. Such an approach allows the investigation of energy removal on different scales in space and time, without explicitly modeling discontinuities. In particular, energy removal from the interior of large-scale blocks can be simulated.

7.3 Lessons Learned for Efficient and Sustainable Extinction Strategies

The scenario simulations for the investigation of extinction activities show some uncertainties or difficulties which should be involved in the planing of extinction strategies to obtain an efficient and sustainable result.

The extinction achievable by surface coverage is a long-term process. Scenario simulations show that the maximum temperature can be reduced by 200 Kelvin after a coal fire simulation time of 275 days. Thus, some years will likely elapse before an underground coal fire can be extinguished by pure surface coverage. In addition, an uncertainty in such operation is the unknown minimum area which needs to be covered to prevent oxygen supply efficiently. Especially, coverage of operationally difficult locations like outcrops may be problematic.

Concerning water injection one uncertainty is the removal of heat from mechanically less disturbed locations. Because large-scale cavities likely exist in and above burnt coal seam parts, injected water will take its preferential way through such cavities, whereas less permeable locations cannot be cooled. Consequently, energy still stored in the rocks may re-ignite the seam after injection.

Concluding from these observations, water injection should preferentially be performed to obtain a fast and efficient extinction success. Injection locations should be placed in undisturbed underground, from which the water can penetrate to the combustion centers. This aspect will reduce the danger of re-ignition. As an additional prevention strategy, the surface should be covered with fine-grained material to reduce the penetration of oxygen from the surface. Thereby, attention should be paid on the extent of the coverage area. Of course, the reduction of oxygen supply by surface coverage can only be efficient when other oxygen sources like underground mines are eliminated.

8 Summary, Conclusions and Outlook

Aim of this study was to bring forward the understanding of underground coal fires with respect to physico-chemical processes being relevant for a fire propagation. A numerical model has been presented for the simulation of underground coal fires, with thermal, hydraulic and chemical processes involved. Process formulation is based on a single-continuum approach to describe transport processes in discontinuous (porous) media. Macroscopic parameters are used to characterize these processes. Two attributes realized in the model are of particular relevance for underground coal fires: The consideration of chemical reactions in the underground coal seam and its coupling to transport processes in the surrounding rocks. The transport processes represent the link between the underground combustion and the atmosphere. Numerical simulations based on this model give insight into the temporal behavior of an underground coal fire.

Conservation equations formulating the physico-chemical model have numerically been solved with a finite-element simulator. Simulation of the reactive transport of oxygen has been realized by an operator-splitting approach, which separates very fast reaction kinetics from moderately fast oxygen transport. This allows the fire propagation to be controlled by oxygen transport instead of reaction kinetics. An additional extrapolation algorithm has been used to increase the calculation time step, based on the assumption that the oxygen consumption rate remains constant over long times compared to the oxygen transport time scale.

With this model, a sensitivity study has been performed. The permeability and the effective thermal conductivity have been varied to investigate their influence on the fire propagation rate and the development of the combustion temperature. An additionally introduced macroscopic variable, the Representative Length of oxygen drop within the combustion center, has also been varied.

The flow system around an underground coal fire has been investigated with respect to influences from the atmosphere. For that purpose, temporal pressure variations as monitored in a coal fire test site have been inserted as boundary conditions into the model. In addition, winds blowing towards an outcrop have been realized by increased pressure values at the boundary. A response of the system to these external influences has been studied based on the variations of the pressure, the temperature, and the oxygen concentration at selected observation points.

Model validation and calibration have been discussed based on a comparison between simulation results and *in-situ* measurements. Observations summarized in the literature have also been used for the comparison. *In-situ* investigations include CO/CO_2 ratio measurements, temperature measurements, measurements of the pressure difference between the atmosphere and the subsurface, measurements of the oxygen concentration and flow rate measurements.

Based on a simplified physical model, extinction scenarios have finally been simulated.

Two scenarios have been addressed: a surface coverage scenario and a water injection scenario.

The simulation results can be summarized as follows. The used physico-chemical model enables consideration of an underground coal fire which is linked to the atmosphere by macroscopic transport processes in adjacent rocks. Especially, the transportation of oxygen to the combustion center is involved, which is one precondition for fire maintenance.

A numerical model has been developed for the simulation in acceptable calculation times. Relevant processes controlling the overall fire propagation rate are involved. The processes are formulated for macroscopic considerations, hence an underground coal fire can be investigated with respect to macroscopic parameters of embedding discontinuous rocks.

The sensitivity study shows that the permeability of the rocks has the main influence on the fire propagation rate. Within the small range $5 \times 10^{-10} m^2 \leq k \leq 10^{-9} m^2$, the propagation rate varies between 3 and 50 meters per year. For higher permeabilities ($k = 10^{-8} m^2$), the propagation rate reaches 340 meters per year. However, it is dubious if the physico-chemical model is appropriate to consider transport processes at such high permeabilities. The effective thermal conductivity has minor influence on the fire propagation rate, but controls the combustion temperature. Once a fire has developed, a variation of the effective thermal conductivity results in a maximum combustion temperature between 900K and 1300K. The ignition of an underground coal fire proved to depend on the thermal conductivities of surrounding rocks and coal. A fire does not develop from an initial glowing nest in the underground coal seam for $\lambda_{0,rock} \geq 2.5 W m^{-1} K^{-1}$ and $\lambda_{0,coal} \geq 0.5 W m^{-1} K^{-1}$.

The flow behavior around an underground coal fire responds to influences from the atmosphere, which are atmospheric pressure variations and winds. The oxygen concentration responds to the daily pressure variations. Depending on the underground position, amplitude and phase shift of the oxygen concentration response differ. Convection is the dominant transport mechanism for oxygen transport. The temperature responds to atmospheric pressure variations only in the combustion center. In the surrounding rocks, the temperature does not respond to the pressure variations at the boundary. Hence, the dominant transport mechanism for heat is conduction or radiation at high temperatures.

The model could be validated by a comparison between simulation results and *in-situ* measurements, as simulated fire propagation rates and combustion temperatures are of reasonable magnitude. In addition, results obtained from *in-situ* measurements are reproduced by the numerical model with acceptable accuracy. Model calibration could not be performed due to the difference between the single-continuum approach, in which discontinuous media are treated as being regionally homogeneous, and the existing large-scale fractures in real coal fire test sites.

Although a strongly simplified physico-chemical model for water injection considerations is used, a simulation example for water injection gives insight into the cooling behavior of the system. It could be shown that water injection into mechanically disturbed regions does not sufficiently cool undisturbed parts. Hence, re-ignition after extinction may set in. In contrast, water injection in front of the combustion center shows to extract heat more efficiently. The simulation of surface coverage shows that the interruption of oxygen supply from the atmosphere mitigates the fire propagation.

Summarizing, the presented numerical model is applicable to simulate underground coal

fires on macroscopic scales in acceptable calculation times. Simulations can be performed to investigate the coupling between transport processes in embedding rocks and the combustion in the underground seam. The simulation tool can finally be used for practical purposes like the simulation of extinction scenarios.

Unresolved issues are still existent or came up during the study. Concerning the presented physico-chemical model, two aspects should be clarified by laboratory or *in-situ* experiments to prove the model's reliability. A Representative Length over which the oxygen concentration in the combustion center decreases from the initial value to zero should be determined. A similar parameter has not been introduced previously, at least not for large-scale coal fires. Additionally, radiation has been formulated with a semi-empirical formula. Although the formula is a linearized form of the expression for radiative energy flux, the magnitude of the introduced parameter β has been assumed. An experimental determination of the radiative energy flux around underground coal fires is desirable. For both issues, the consideration of phenomena on macroscopic scales should be realized. It is insufficient to restrict to small rock samples and not considering large-scale fractures, which exist in real coal fire sites.

Still unclear is the influence of mine activities on underground coal fires. Mine activities relevant for coal fires include the superposition of externally imposed pressure differences (by mine ventilation) to pressure differences resulting from thermal convection. In addition, abrupt changes in the rock permeability due to sudden mechanical failure have not yet been considered by the model.

Another unresolved issue is the influence of water (either bonded in coal or freely existing in the voids) on the dynamic behavior of underground coal fires. Influences may arise from the evaporation process, which has consequences for the energy balance.

Finally, the influence of developing cavities on the flow system has not been addressed in this study. Cavities result from the consumption of coal. In the present model, the soil parameters (permeability, porosity) have not been changed once cavities have been developed, i.e. once the coal concentration has remarkably decreased. Instead, locations where coal has been consumed are further on assumed as being porous and equally permeable as before. Additionally, the flow behavior in the cavities is likely different from the flow behavior in porous media.

Concluding, this work can be considered as a first step to bring forward the numerical simulation of underground coal fires on macroscopic scales. Reviewing this study, the model proved to be useful for principal investigations into the dynamic behavior of underground coal fires. Especially, macroscopic parameters of surrounding rocks like the permeability are included, so that the simulation and *in-situ* investigations can be combined to investigate coal fire sites more precisely. *In-situ* investigations at the surface above underground coal fires can be realized by boundary conditions.

The simulation model is especially useful to investigate the influence of phenomena in the surrounding rocks to the fire behavior. Sensitivity studies of macroscopic parameters can be performed. Also, the effects of complex geological formations on the fire can be estimated by the simulation approach.

Furthermore, the simulation model is applicable to investigate an influence of mine ventilation on the coal fire dynamics. Mine ventilation can be realized by the specification of

constant-pressure boundary conditions into the model. These boundary conditions represent externally imposed pressure differences and cause forced convection.

Finally, the simulation approach proved to be a useful tool to support extinction and prevention activities. Although simplifications have been assumed for the simulation of extinction scenarios, the model is able to predict effects of extinction activities on the coal fire behavior.

Nevertheless, an application to predict a specific coal fire test site is hardly possible with the presented model. Besides of the two-dimensionality, the single-continuum approach for process description is inappropriate to consider the heterogeneous nature of fire sites. However, also experimental methods need to be improved to obtain better insight into the quantification of underground coal fires from *in-situ* measurements.

Extensions of the numerical model will improve its applicability to predict the dynamic behavior of underground coal fires. Extensions include the representation of heterogeneous surrounding beds. Especially, the incorporation of fracture flow will give insight into the effects of large-scale fractures on the circulation system around coal fires.

Different approaches are possible to consider the high heterogeneity. These are a hybrid modeling approach in which large-scale fractures and the processes within them are discretized and embedded in a homogeneous continuum. Alternatively, Monte-Carlo simulations can be performed with statistically distributed macroscopic parameters, especially the permeability. Finally, the consideration of processes taking place on different spatial and temporal scales can be realized by a multi-continua approach, where processes taking place at a specific range of scales are considered by a continuum. The division of the model into some ranges of scales presumes the consideration of multiple continua. These continua are coupled to realize an exchange between processes taking place at the different scales.

The model also needs to be extended to properly consider the influence of developing cavities on the flow behavior. Thereby, one challenge is given by the difference in physical processes taking place in the porous matrix and the cavities, respectively. Whereas a formulation of flow through porous media is given by Darcy's law, flow within non-porous cavities require the solution of the Navier-Stokes equations. The simulation tool should be able to switch between porous-media flow and fluid flow in purely fluid-filled media once cavities have developed.

A further extension of the model is the consideration of multiple fluid phases. It is likely that water and gas coexist in an underground coal fire system. Except for natural humidity, high amounts of water can be bonded in coal.

Finally, an exchange between the circulation system around a coal fire and the atmosphere can be improved by the incorporation of extended boundary conditions. Extensions include the consideration of heat exchange between the atmosphere (including sunshine radiation) and the soil surface. Such an extension is especially important for better interpretation of remote sensing data and *in-situ* measurements at the surface.

Bibliography

- Ahlers, C. F., Finsterle, S., and Bodvarsson, G. S. (1999): *Characterization and prediction of subsurface pneumatic response at Yucca Mountain, Nevada*. J. Contam. Hydrol., 38, 47 – 68.
- Ahmed, N. and Sunada, D. K. (1969): *Nonlinear flow in porous media*. In *Journal of the Hydraulics Division*, volume 95 (HY 6, Proc. Paper 6883) of ASCE, p. 1847 – 1857.
- Annamalai, K. and Ryan, W. (1993): *Interactive processes in gasification and combustion - II. Isolated carbon, coal and porous char particles*. Prog. Energy Combust. Sci., 19, 383 – 446.
- Annamalai, K. and Ryan, W. (1994): *Interactive processes in gasification and combustion - III. Arrays, Streams and Clouds*. Prog. Energy Combust. Sci., 20, 487 – 618.
- Arenillas, A., Pevida, C., Rubiera, F., and Pis, J. J. (2003): *Comparison between the reactivity of coal and synthetic coal models*. Fuel, 82, 2001 – 2006.
- Bai, M., Elsworth, D., and Roegiers, J.-C. (1993): *Multiporosity/multipermeability approach to the simulation of naturally fractured reservoirs*. Water Resources Research, 29(6), 1621 – 1633.
- Banerjee, K., Cherimisinoff, N. P., and Cherim (1986): *Handbook of heat and mass transfer*, volume 1, chapter 42: Design Practices for Combustion and Incineration, p. 1351 – 1401. Gulf Publ. Comp., Houston, Texas.
- Barenblatt, G. I., Entov, V. M., and Ryzhik, V. M. (1990): *Theory of Fluid Flow Through Natural Rocks*, volume 3 of *Theory and Applications of Transport in Porous Media*. Kluwer Academic Publishers, Dordrecht.
- Barry, D. A., Miller, C. T., and Culligan-Hensley, P. J. (1996): *Temporal discretisation errors in non-iterative split-operator approaches to solving chemical reaction/groundwater transport models*. J. Contam. Hydrol., 22, 1 – 17.
- Barry, D. A., Miller, C. T., Culligan, P. J., and Bajracharya, K. (1997): *Analysis of split operator methods for nonlinear and multispecies groundwater chemical transport models*. Mathematics and Computers in Simulation, 43, 331 – 341.
- Bear, J. (1972): *Dynamics of Fluids in Porous Media*. American Elsevier, New York.
- Bear, J. and Bachmat, Y. (1990): *Introduction to Modeling of Transport Phenomena in Porous Media*, volume 4 of *Theory and Applications of Transport in Porous Media*. Kluwer Academic Publishers, Dordrecht.

- Beavers, G. S. and Sparrow, E. M. (1969): *Non-darcy flow through fibrous porous media*. Journal of Applied Mechanics, 36, p. 711 – 714.
- Beavers, G. S., Sparrow, E. M., and Rodenz, D. E. (1973): *Influence of bed size on the flow characteristics and porosity of randomly packed beds of spheres*. J. Fluid Mech., 40, 655 – 660.
- Bell, F. G., Bullock, S. E. T., Hälbig, T. F. J., and Lindsay, P. (2001): *Environmental impacts associated with an abandoned mine in the Witbank Coalfire, South Africa*. Int. J. Coal Geology, 45, 195 – 216.
- Berkowitz, B. (2002): *Characterizing flow and transport in fractured geological media: A review*. Adv. Water Resour., 25, 861 – 884.
- Bernsdorf, J., Brenner, G., and Durst, F. (2000): *Numerical analysis of the pressure drop in porous media flow with lattice Boltzmann (BGK) automata*. Computer Physics Communications, 129, 247 – 255.
- Bethge, P. (1999): *Feuer unter China*. Der Spiegel, 44, 238 – 242.
- Bews, I. M., Hayhurst, A. N., Richardson, S. M., and Taylor, S. G. (2001): *The order, Arrhenius parameters, and mechanisms of the reaction between gaseous oxygen and solid carbon*. Combustion and Flame, 124, 231 – 245.
- Bhati, S. K. and Perlmutter, D. D. (1980): *A random pore model for fluid-solid reaction: I. Isothermal, kinetic control*. AIChE J., 26, 379 – 385.
- Bin, L. E. and Yi, F. T. (1999): *Atlas of China*. China Cartograph. Publ. House, Beijing, 2nd edition.
- Bökemeier, R. and Elleringmann, S. (2002): *Höllenfahrt durch China*. Geo, 9, 21 – 29.
- Blasi, C. D. (1993): *Modeling and simulation of combustion processes of charring and non-charring solid fuels*. Prog. Energy Combust. Sci., 19, 71 – 104.
- Bradshaw, S., Glasser, D., and Brooks, K. (1991): *Self-ignition and convection patterns in an infinite coal layer*. Chem. Eng. Comm., 105, 255 – 278.
- Brenner, G., Pickenäcker, K., Pickenäcker, O., Trimis, D., Wawrzinek, K., and Weber, T. (2000): *Numerical and experimental investigation of matrix-stabilized methane/air combustion in porous inert media*. Combustion and Flame, 123, 201 – 213.
- Breuer, M., Wessling, S., Schmalzl, J., and Hansen, U. (2004): *Effect of inertia in Rayleigh-Bénard convection*. Physical Review E, 69, 026302.
- Brooks, K. and Glasser, D. (1986): *A simplified model of spontaneous combustion in coal stockpiles*. Fuel, 65, 1035 – 1041.
- Brooks, K., Balakotaiah, V., and Luss, D. (1988a): *Effect of natural convection on spontaneous combustion of coal stockpiles*. AIChE J., 34(3), 353 – 365.

- Brooks, K., Bradshan, S., and Glasser, D. (1988b): *Spontaneous combustion of coal stockpiles - an unusual reaction engineering problem*. Chemical Engineering Science, 43(8), 2139 – 2145.
- Buhrow, C., Lippmann, G., and Stöttner, M. T. (2004a): *Kohlebrände in der Volksrepublik China*. Glückauf, 140(10), 488 – 494.
- Buhrow, C., Stöttner, M. T., and Bandelow, K.-F. (2004b): *Summer Field Campaign 2004: Field Report Bergwerk "Su Hai Tu", Preliminary Version*. Unpublished project report as a contribution to the Sino-German Research Initiative "Innovative Technologies for Exploration, Extinction and Monitoring of Coal Fires in North China", TU Bergakademie Freiberg, Germany.
- Cardellini, C., Chiodini, G., Frondini, F., Granieri, D., Lewicki, J., and Peruzzi, L. (2003): *Accumulation chamber measurements of methane fluxes: application to volcanic-geothermal areas and landfills*. Applied Geochemistry, 18, 45 – 54.
- Carlsaw, H. S. and Jaeger, J. C. (1959): *Conduction of Heat in Solids*. Clarendon Press, Oxford, 2nd edition.
- Carrayrou, J., Mosé, R., and Behra, P. (2004): *Operator-splitting procedures for reactive transport and comparison of mass balance errors*. J. Contam. Hydrol., 68, 239 – 268.
- Cassells, C. J. S. and van Genderen, J. L. (1995): *Thermal modeling of underground coal fires in northern China: Remote sensing in action*. In *Proceedings of the 21st Annual Conference of the Remote Sensing Society*, p. 544 – 551. University of Southampton, England.
- Cermak, V. and Rybach, L. (1982): *Thermal Conductivity and Specific Heat of Minerals and Rocks*. In G. Angenheister (Ed), *Landolt-Börnstein - Numerical Data and Functional Relationships in Science and Technology, New Series, Group V: Geophysics and Space Research, Vol. 1: Physical Properties of Rocks, Subvolume B*, p. 302 - 343. Springer-Verlag, Heidelberg, Berlin.
- Chen, S. and Doolen, G. D. (1998): *Lattice Boltzmann method for fluid flow*. Annu. Rev. Fluid Mech., 30, 329 – 364.
- Clauser, C. (2006): *Geothermal Energy*. In K. Heinloth (Ed), *Landolt-Börnstein - Group VIII: Advanced Materials and Technologies, Vol. 3: Energy Technologies, Subvol. C: Renewable Energies*, p. 493-604. Springer-Verlag, Heidelberg, Berlin.
- Clauser, C. and Huenges, E. (1995): *Thermal Conductivity of Rocks and Minerals*. In T. J. Ahrens (Ed), *Rock Physics and Phase Relations - A Handbook of Physical Constants*, p. 105 – 126. American Geophysical Union, Washington, DC.
- Couland, O., Morel, P., and Caltagirone, J. P. (1988): *Numerical modelling of nonlinear effects in laminar flow through a porous medium*. J. Fluid Mech., 190, 393 – 407.

- Dagan, G. (1989): *Flow and Transport in Porous Media*. Springer-Verlag, Berlin.
- Dai, S., Ren, D., Tang, Y., Shao, L., and Li, S. (2002): *Distribution, isotropic variation and origin of sulfur in coals in the Wuda coalfield, Inner Mongolia, China*. *Int. J. Coal Geology*, 51, 237 – 250.
- De Ville, A. (1996): *On the properties of compressible gas flow in a porous media*. *Transport in Porous Media*, 22(3), 287 – 306.
- Dirsch, H.-J. G. (1998): *FEFLOW Reference Manual*. Wasy Institute for Water Resources Planning and Systems Research Ltd., Berlin, Germany.
- Dullien, F. A. L. and Azzam, M. I. S. (1973): *Flow rate-pressure gradient measurements in periodically nonuniform capillary tubes*. *AIChE J.*, 19(2), 222 – 229.
- Engeln-Muellges, G. and Reutter, F. (1996): *Numerik-Algorithmen - Entscheidungshilfe zur Auswahl und Nutzung*. VDI Verlag, Düsseldorf, 8th edition.
- Ergun, S. (1952): *Fluid flow through packed columns*. *Chemical Engineering Progress*, 48(2), 89 – 94.
- Evans, D. G. and Raffensperger, J. P. (1992): *On the stream function of variable-density groundwater flow*. *Water Resources Research*, 28(8), 2141 – 2145.
- Ferziger, J. H. and Peric, M. (1999): *Computational Methods for Fluid Dynamics*. Springer-Verlag, Berlin, Heidelberg, 2nd edition.
- Fierro, V., Miranda, J. L., Romero, C., Andrés, J. M., Arriaga, A., and Schmal, D. (2001): *Model predictions and experimental results on self-heating prevention of stockpiled coals*. *Fuel*, 80, 125 – 134.
- Filippova, L. and Hänel, D. (1998): *Lattice-BGK model for low Mach number combustion*. *International Journal of Modern Physics C*, 9(8), 1439 – 1445.
- Finkelmann, R. B. (2004): *Potential health impacts of burning coal beds and waste banks*. *Int. J. Coal Geology*, 59, 19 – 24.
- Forchheimer, P. (1901): *Wasserbewegung durch Boden*. *Z. Ver. Deutsch. Ing.*, 45, 1782 – 1788.
- Fujitsu, M., Hasatani, M., and Sugiyama, S. (1977): *Effective thermal conductivity of insulating-refractory material*. *Journal of Chemical Engineering of Japan*, 10(3), 242 – 244.
- Gavalas, G. R. (1980): *A random capillary model with application to char gasification and chemically controlled rates*. *AIChE J.*, 26, 557 – 585.
- Geissinger, J. (1990): *Managing underground mine fires: The case of Centralia, Pennsylvania*. *Pa. Geogr.*, 28(2), 22 – 26.

- Ghetti, P., Robertis, U. d., D'Antone, S., Villani, M., and Chiellini, E. (1985): *Coal combustion - correlation between surface area and thermogravimetric analysis data*. Fuel, 64, 950 – 955.
- Ghosh, R. (1986): *Spontaneous combustion of certain Indian coals - some physico-chemical considerations*. Fuel, 65, 1042 – 1046.
- Gielisch, H. and Barth, U. (2003): *Work Package 2380 - Existing Extinction Strategies - Some Remarks to the Extinction Methods to Fight Against Coal Fires in Ninxia and Inner Mongolia/PR of China*. Unpublished project report as a contribution to the Sino-German Research Initiative "Innovative Technologies for Exploration, Extinction and Monitoring of Coal Fires in North China", DMT, Essen, University of Wuppertal, Germany.
- Gielisch, H. and Kahlen, E. (2003): *Work Package 2210 - General Geological Description of Helan Shan Mountain Area with Emphasis on Coal Fire Areas: Geology of the Helan Shan - Field Report*. Unpublished project report as a contribution to the Sino-German Research Initiative "Innovative Technologies for Exploration, Extinction and Monitoring of Coal Fires in North China", DMT, Essen, Germany.
- Gielisch, H. and Künzer, C. (2003): *Work Package 2220 - Structural Pattern of the Coal Deposits (Wuda, Gujigou, Gulaben); Analysis of Linear Pattern (Air Photos; Satellite Images): Cracks and Crack Systems of the Test Areas*. Unpublished project report as a contribution to the Sino-German Research Initiative "Innovative Technologies for Exploration, Extinction and Monitoring of Coal Fires in North China", DMT, Essen, DFD/DRL, Wessling, Germany.
- Glover, L. (1998): *Burning Beneath the Surface*. Tribune Review, May 3rd 1998, USA.
- Gong, R., Burnell, J. G., and Wake, G. C. (1999): *Modelling spontaneous combustion in wet lignite*. Combust. Theory Modelling, 3, 215 – 232.
- Guéguen, Y. and Palciauskas, V. (1994): *Introduction to the Physics of Rocks*. Princeton University Press, Princeton, New Jersey.
- Guin, J. A., Kessler, D. P., and Greenkorn, R. A. (1971): *The permeability tensor for anisotropic nonuniform porous media*. Chem. Eng. Sci., 26, 1475 – 1478.
- Guntermann, K. (1988): *Grundlagen- und Laborarbeiten zur Untertagevergasung*. In *Seminar zur Untertageumwandlung von Kohle - Ein Beitrag zur Energieversorgung der Zukunft?*, p. 16 – 32. Studiengesellschaft Kohlegewinnung Zweite Generation e.V., Saalbau - Essen.
- Guo, Z. and Zhao, T. S. (2003): *Explicit finite-difference lattice Boltzmann method for curvilinear coordinates*. Physical Review E, 67, 066709.
- Habbar, A. (2001): *Direkte und inverse Modellierung reaktiver Transportprozesse in klüftig-porösen Medien*. Ph.D. thesis, ISEB, University of Hannover, Germany.

- Harju, J. B. (1980): *Coal Combustion Chemistry*. Pollution Engineering, May 1980, p. 54 – 60.
- Hattwick, M. and Steen, H. (2004): *Handbook of Explosion Prevention and Protection*. Wiley-VCH Verlag GmbH, Weinheim.
- He, X. and Luo, L.-S. (1997): *Theory of the lattice Boltzmann method: From the Boltzmann equation to the lattice Boltzmann equation*. Physical Review E, 56(6), 6811 – 6817.
- Heek, K. H. v. and Mühlen, H.-J. (1984): *Heterogene Reaktionen bei der Verbrennung von Kohle*. BWK, 37(1 - 2), 20 – 28.
- Hjertager, B. H. (1986): *Three-Dimensional Modeling of Flow, Heat Transfer, and Combustion*. In N. P. Cheremisinoff (Ed), *Handbook of Heat and Mass Transfer, volume 1 of Heat Transfer Operations*, p. 1303 – 1350. Gulf Publishing Company, Houston, Texas.
- Hobbs, M. L., Radulovic, P. T., and Smoot, L. D. (1993): *Combustion and gasification of coals in fixed-beds*. Prog. Energy Combust. Sci, 19, 505 – 586.
- Hofmann, J. (1993): *Geomorphologische Untersuchungen zur jungquartären Klimaentwicklung des Helan Shan und seines westlichen Vorlandes (Autonomes Gebiet Innere Mongolei/VR China)*. Ph.D. thesis, Institut für geographische Wissenschaften, Freie University of Berlin, Germany.
- Holzbecher, E. O. (1998): *Modeling Density-Driven Flow in Porous Media*. Springer-Verlag, Berlin.
- Huang, J., Bruining, J., and Wolf, K. H. A. A. (2001): *Modeling of gas flow and temperature fields in underground coal fires*. Fire Safety Journal, 36, 477 – 489.
- Hull, A. S. and Agarwal, P. K. (1998): *Estimation of kinetic rate parameters for coal combustion from measurements of the ignition temperature*. Fuel, 77(9/10), 1051 – 1058.
- Ihle, W. and Kroll, D. M. (2000): *Thermal Lattice-Boltzmann method for non-ideal gases with potential energy*. Computer Physics Communications, 129, 1 – 12.
- Jia, Y. (2004): *Personal communication during the field trip in June 2004 into the Shenhua Coal Mining Area of Wuda (Inner Mongolia, PR China)*. Y. Jia is the chief engineer of the Wuda coal mining area.
- Jing, L. and Hudson, J. A. (2002): *Numerical methods in rock mechanics*. Int. J. Rock Mech. Min. Sci., 39, 409 – 427.
- Jones, J. C., Henderson, K. P., Littlefair, J., and Rennie, S. (1998): *Kinetic parameters of oxidation of coals by heat-release measurement and their relevance to self-heating tests*. Fuel, 77(1/2), 19 – 22.
- Kaiser, R. (2001): *Gitteradaption für die Finite-Elemente-Modellierung gekoppelter Prozesse in geklüftet-porösen Medien*. Ph.D. thesis, ISEB, University of Hannover, Germany.

- Kandhai, D., Soll, W., Chen, S., Hoekstra, A., and Sloom, P. (2000): *Finite-difference Lattice-BGK methods on nested grids*. Computer Physics Communications, 129, 100 – 109.
- Kang, Q., Zhang, D., and Chen, S. (2002): *Unified lattice Boltzmann method for flow in multiscale porous media*. Physical Review E, 66, 056307.
- Kang, Q., Zhang, D., and Chen, S. (2003): *Simulation of dissolution and precipitation in porous media*. Journal of Geophysical Research, 108(B10), 2505, doi:10.1029/2003JB002504.
- Kanney, J. F., Miller, C. T., and Kelley, C. T. (2003): *Convergence of iterative split-operator approaches for approximating nonlinear reactive transport problems*. Adv. Water Resour., 26, 247 – 261.
- Kappelmeyer, O. and Haenel, R. (1974): *Geothermics with Special Reference to Applications*, volume 1 of *Geoexploration Monographs*. Gebrüder Borntraeger, Berlin.
- Keehm, Y., Mukerji, T., and Nur, A. (2004): *Permeability prediction from thin sections: 3D reconstruction and Lattice-Boltzmann flow simulation*. Geophysical Research Letter, 31, L04606.
- Kessels, W. (1980): *Die Bestimmung des stationären Temperaturgradienten und des geothermischen Wärmeflusses aus Flachbohrungen*. Ph.D. thesis, Naturwissenschaftliche Fakultät der Technischen Universität Carolo-Wilhelmina zu Braunschweig, Germany.
- Kessels, W., Wessling, S., Li, X., and Wuttke, M. W. (2006a): *Numerical element distinction for reactive transport modeling regarding reaction rate*. In *Proceedings of MODFLOW2006, Colorado, USA, May 2006*.
- Kessels, W., Wuttke, M. W., Wessling, S., and Li, X. (2006b): *Coal Fire Development from Self-Ignition to Fire Fighting: Numerical Modeling and Measurements for Basic Investigations*. Accepted in *ERSEC Ecological Book Series - 4 on Coal Fire Research*. UNESCO, Beijing, PR China.
- King, A. (1987): *Cindered coal detection using transient electromagnetic methods*. Geoexploration, 24, 367 – 379.
- Kinzelbach, W. (1992): *Numerische Methoden zur Modellierung des Transports von Schadstoffen im Grundwasser*. Oldenbourg Verlag, 2nd edition.
- Klika, Z., Kozubek, T., Martinec, P., Kliková, C., and Dostál, Z. (2004): *Mathematical modeling of bituminous coal seams burning contemporaneously with the formation of a variegated beds body*. Int. J. Coal Geology, 59, 137 – 151.
- Kohl, T., Evans, K. F., Hopkirk, R. J., Jung, R., and Rybach, L. (1997): *Observation and simulation of non-Darcian flow transients in fractured rock*. Water Resources Research, 33(3), 407 – 418.

- Kolditz, O. (1996): *Stoff- und Wärmetransport im Kluftgestein*. Postdoctoral lecture qualification (habilitation), ISEB, University of Hannover, Germany.
- Kolditz, O., Ratke, R., Diersch, H.-J. G., and Zielke, W. (1998): *Coupled groundwater flow and transport: 1. Verification of variable density flow and transport models*. *Adv. Water Resour.*, 21(1), 27 – 46.
- Konikow, L. F. and Bredehoeft, J. D. (1992): *Ground-water models cannot be validated*. *Adv. Water Resour.*, 15, 75 – 83.
- Krause, U. and Schmidt, M. (2001): *The influence of initial conditions on the propagation of smouldering fires in dust accumulations*. *Journal of Loss Prevention in the Process Industries*, 14, 527 – 532.
- Kröhn, K. P. (1991): *Simulation von Transportvorgängen im klüftigen Gestein mit der Methode der Finiten Elemente*. Ph.D. thesis, ISEB, University of Hannover, Germany.
- Krishnaswamy, S., Gunn, R. D., and Agarwal, P. K. (1996a): *Low-temperature oxidation of coal 1: A single-particle reaction-diffusion model*. *Fuel*, 75(3), 333 – 343.
- Krishnaswamy, S., Gunn, R. D., and Agarwal, P. K. (1996b): *Low-temperature oxidation of coal 2: An experimental and modelling investigation using a fixed-bed isothermal flow reactor*. *Fuel*, 75(3), 344 – 352.
- Krishnaswamy, S., Gunn, R. D., and Agarwal, P. K. (1996c): *Low-temperature oxidation of coal 3: Modelling spontaneous combustion in coal stockpiles*. *Fuel*, 75(3), 353 – 362.
- Kuenzer, C. (2005): *Demarcating Coal Fire Risk Areas Based on Spectral Test Sequences and Partial Unmixing Using Multi Sensor Remote Sensing Data*. Ph.D. thesis, Technical University of Vienna, Austria.
- Kuenzer, C., Zhang, J., Tetzlaff, A., van Dijk, P., Voigt, S., Mehl, H., and Wagner, W. (2007): *Uncontrolled coal fires and their environmental impacts: Investigating two arid mining regions in north-central China*. *Applied Geography*, 27, 42 – 62.
- Kunz, H. (2005): *GINA*. Uncommercial Grid Generator, BGR, Hannover, Germany.
- Kus, J., Hiltmann, W., and Balke, A. (2006): *In-Situ gasification of coal, a natural example: micropetrography of coal oxidation, carbonisation and combustion*. Accepted in *ERSEC Ecological Book Series - 4 on Coal Fire Research*. UNESCO, Beijing, PR China.
- Landmeyer, J. E. (1996): *Aquifer response to record low barometric pressures in the south-eastern United States*. *Ground Water*, 34(5), 917 – 924.
- Lichtner, P. C. (1996): *Continuum formulation of multicomponent-multiphase reactive transport*. In P. C. Lichtner, C. I. Steefel, and E. H. Oelkers (Eds), *Reactive Transport in Porous Media*, volume 34 of *Reviews in Mineralogy*, p. 1 – 81. Mineralogical Society of America.

- Lichtner, P. C. (2000): *Critique of Dual Continuum Formulations of Multicomponent Reactive Transport in Fractured Porous Media*. In B. Faybishenko, P. A. Witherspoon, and S. M. Benson (Eds), *Dynamics of Fluids in Fractured Rock*, Geophysical Monograph 122, p. 281 – 298. American Geophysical Union, Washington, DC.
- Litschke, T. (2005): *Innovative Technologies for Exploration, Extinction and Monitoring of Coal Fires in North China - Detailed Mapping of Coal Fire Sites in Combination with in-situ Flux Measurements of Combustion-Gases to Estimate Gas Flow Balance and Fire Development (Wuda Coal Field, Inner Mongolia Autonomous Region)*. Master's thesis, Institute of Geography, Department of Geology, University of Duisburg-Essen, Germany.
- Litschke, T., Wiegand, J., Schlömer, S., Gielisch, H., and Bandelow, F.-K. (2006): *Detailed mapping of coal fire sites in combination with in-situ flux measurements of combustion-gases to estimate gas flow balance and fire development (Wuda coalfield, Inner Mongolia, PR China)*. Accepted in *ERSEC Ecological Book Series - 4 on Coal Fire Research*. UNESCO, Beijing, PR China.
- Liu, G.-S. (1999): *Mathematical Modelling of Coal Char Reactivity in a Pressurised Entrained Flow Gasifier*. Ph.D. thesis, School of Chemical Engineering, University of Newcastle, Australia.
- Liu, G., Benyon, P., Benfell, K. E., Bryant, G. W., Tate, A. G., Boyd, R. K., Harris, D. J., and Wall, T. F. (2000): *The porous structure of bituminous coal chars and its influence on combustion and gasification under chemically controlled conditions*. *Fuel*, 79, 617 – 626.
- Lohrer, C. (2006): *Einflussgrößen auf die Selbstentzündung von Schüttgütern und Stäuben - experimentelle Untersuchungen und numerische Simulationen*. Volume 13, BAM-Dissertationsreihe, Wirtschaftsverlag NW, Bremerhafen.
- Lohrer, C., Schmidt, M., and Krause, U. (2004): *Ein Modell zur Berechnung des gekoppelten Wärme- und Stofftransportes in porösen, reaktionsfähigen Medien*. Unpublished project report as a contribution to the Sino-German Research Initiative "Innovative Technologies for Exploration, Extinction and Monitoring of Coal Fires in North China", BAM - Div. II.22, Berlin, Germany.
- Lohrer, C., Schmidt, M., and Krause, U. (2005): *A study on the influence of liquid water and water vapour on the self-ignition of lignite coal-experiments and numerical simulations*. *Journal of Loss Prevention in the Process Industries*, 18, 167 – 177.
- Louis, C. (1967): *Strömungsvorgänge in Klüftigen Medien und ihre Wirkung auf die Stand-sicherheit von Bauwerken und Böschungen im Fels*. Ph.D. thesis, Inst. f. Bodenmechanik u. Felsmechanik, University of Karlsruhe, Germany.
- Malow, M. and Krause, U. (2004): *The overall activation energy of the exothermic reactions of thermally unstable materials*. *Journal of Loss Prevention in the Process Industries*, 17, 51 – 58.

- Massmann, J. and Farrier, D. F. (1992): *Effects of atmospheric pressures on gas transport in the vadose zone*. Water Resources Research, 28(3), 777 – 791.
- McPherson, M. J. (1993): *Subsurface Ventilation and Environmental Engineering*. Chapman & Hall, London.
- Mei, C. C. and Auriault, J.-L. (1991): *The effect of weak inertia on flow through a porous medium*. J. Fluid Mech., 222, 647 – 663.
- Michalski, S. R. (2004): *The Jharia fire control technical assistance project: an analysis*. Int. J. Coal Geology, 59, 83 – 90.
- Milch, I. (2001): *Kohle in China*. Energie Perspektiven - Forschung for die Energieversorgung von Morgen, Max-Planck-Institut für Plasmaphysik, Garching, Germany, 01/2001.
- Mrasek, V. (2005): *Die glühenden Berge der Kohle*. Spiegel Online, Mar 22nd, 2005.
- Muskat, M. (1937): *The Flow of Homogeneous Fluids Through Porous Media*. McGraw-Hill Book Company, Inc., New York, London.
- Nickel, U. (1995): *Lehrbuch der Thermodynamik, eine verständliche Einführung*. Carl Hanser Verlag, München.
- Nield, D. A. and Bejan, A. (1999): *Convection in Porous Media*. Springer-Verlag, New York, 2nd edition.
- Nolter, M. A. and Vice, D. H. (2004): *Looking back at the Centralia coal fire: a synopsis of its present status*. Int. J. Coal Geology, 59, 99 – 106.
- Nordon, P., Young, B. C., and Bainbridge, N. W. (1979): *The rate of oxidation of char and coal in relation to their tendency to self-heating*. Fuel, 58, 443 – 449.
- Näser, K.-H. (1968): *Physikalische Chemie*. VEB Deutscher Verlag für Grundstoffindustrie, Leipzig.
- Oran, E. S. and Boris, J. P. (2001): *Numerical Simulation of Reactive Flow*. Cambridge University Press, 2nd edition.
- Perkins, G., Saghafi, A., and Sahajwalla, V. (2001): *Numerical Modeling of Underground Coal Gasification and its Application to Australian Coal Seam Conditions*. In *18th Ann. Pittsburgh Coal Conference*. Newcastle, Great Britain.
- Perkins, G. and Sahajwalla, V. (2005): *A mathematical model for the chemical reaction of a semi-infinite block of coal in underground coal gasification*. Energy & Fuels, 19, 1679 – 1692.
- Prakash, A., Gens, R., and Vekerdy, Z. (1999): *Monitoring coal fires using multi-temporal night-time thermal images in a coalfield in north-west China*. Int. J. Remote Sensing, 20(14), 2883 – 2888.

- Prakash, A., Fielding, E. J., Gens, R., Genderen, J. L. v., and Evans, D. L. (2001): *Data fusion for investigating land subsidence and coal fire hazards in a coal mining area*. Int. J. Remote Sensing, 22(6), 921 – 932.
- Prakash, A. and Vekerdy, Z. (2004): *Design and implementation of a dedicated prototype GIS for coal fire investigations in North China*. Int. J. Coal Geology, 59, 107 – 119.
- Press, W. H., Teukolsky, S. A., Vetterling, W. T., and Flannery, B. P. (1992): *Numerical Recipes in C*. Cambridge University Press, New York.
- Qian, Y. H., d’Humieres, D., and Lallemand, P. (1992): *Lattice BGK models for Navier-Stokes equation*. Europhysical Letters, 17, 479 – 484.
- Radlinski, A. P., Mastalerz, M., Hilde, A. L., Hainbuchner, M., Rauch, H., Baron, M., Lin, J. S., Fan, L., and Thiyagarajan, P. (2004): *Application of SAXS and SANS in evaluation of porosity, pore size distribution and surface area of coal*. Int. J. Coal Geology, 59, 245 – 271.
- Rosema, A., Guan, H., and Veld, H. (2001): *Simulation of spontaneous combustion, to study the causes of coal fires in the Rujigou Basin*. Fuel, 80, 7 – 16.
- Ruth, D. and Ma, H. (1992): *On the derivation of the Forchheimer equation by means of the averaging theorem*. Transport in Porous Media, 7, 255 – 264.
- Saegusa, T., Kamata, K., Iida, Y., and Wakao, N. (1974): *Thermal conductivities of porous solids*. International Chemical Engineering, 14(1), 169 – 173.
- Sauer, H. D. (2002): *Verbrennung am falschen Ort*. NZZ Online, May 2002.
- Sauter, M., Kovács, A., Geyer, T., and Teutsch, G. (2006): *Modellierung der Hydraulik von Karstgrundwasserleitern - Eine Übersicht*. Grundwasser – Zeitschrift der Fachsektion Hydrogeologie, 3, 143 – 156.
- Schaumann, G., Simon, B., and Chun, Y. C. (2006): *Geophysical Investigation of the Coal Fire Area of Wuda, Inner Mongolia, with Electromagnetic and Magnetic Methods*. Accepted in *ERSEC Ecological Book Series - 4 on Coal Fire Research*. UNESCO, Beijing, PR China.
- Scheidegger, A. E. (1961): *General theory of dispersion in porous media*. Journal of Geophysical Research, 66(10), 3273 – 3278.
- Schlömer, S. (2005): *Intermediate Report WP 3410 & 3420 (Gas Geochemistry of Combustion Gases)*. Unpublished project report as a contribution to the Sino-German Research Initiative "Innovative Technologies for Exploration, Extinction and Monitoring of Coal Fires in North China", BGR, Hannover, Germany.
- Schlömer, S., Teschner, M., Poggenborg, J., and Seeger, C. (2006): *Gas and Temperature Monitoring of a Natural Coal Fire in Wuda (Inner Mongolia Autonomous Region, PRC)*.

- Accepted in *ERSEC Ecological Book Series - 4 on Coal Fire Research*. UNESCO, Beijing, PR China.
- Schmal, D. (1987): *A Model for the Spontaneous Heating of Stored Coal*. Ph.D. thesis, Technische Universiteit, Delft, The Netherlands.
- Schmal, D., Duyzer, J. H., and Heuven, J. W. (1985): *A model for the spontaneous heating of coal*. *Fuel*, 64, 963 – 972.
- Schmidt, L. D. and Elder, J. L. (1940): *Atmospheric oxidation of coal at moderate temperatures*. *Industrial and Engineering Chemistry*, 32(2), 249 – 256.
- Schmidt, M., Lohrer, C., and Krause, U. (2003): *Self-ignition of dust at reduced volume fractions of ambient oxygen*. *Journal of Loss Prevention in the Process Industries*, 16, 141 – 147.
- Schmidt, M., Lohrer, C., and Krause, U. (2005): *Results of Laboratory Investigations: Self-Ignition and Burning Behaviour of Coal Samples*. Unpublished project report as a contribution to the Sino-German Research Initiative "Innovative Technologies for Exploration, Extinction and Monitoring of Coal Fires in North China", BAM - Div. II.22, Berlin, Germany.
- Schoofs, S. (1999): *Thermochemical Convection in Porous Media*. Ph.D. thesis, Earth Science Institute, Vening Meinesz Research School of Geodynamics, Utrecht University, The Netherlands.
- Shadman, F. and Cavendish, J. C. (1980): *An analytical model for the combustion of coal particles*. *The Canadian Journal of Chemical Engineering*, 58, 470 – 475.
- Skjetne, E., Hansen, A., and Gudmundsson, J. S. (1999): *High-velocity flow in a rough fracture*. *J. Fluid Mech.*, 383, 1 – 28.
- Sternberg, R. and Lippincott, C. (2004): *Magnetic surveys over clinkers and coal seam fires in Western North Dakota*. In *2004 Denver Annual Meeting*, paper 15 – 9. Denver, Colorado.
- Stockman, H. W., Li, C., and Wilson, J. L. (1997): *A lattice-gas and lattice-Boltzmann study of mixing at continuous fracture junctions: importance of boundary conditions*. *Geophysical Research Letter*, 24(12), 1515 – 1518.
- Stracher, G. B. and Taylor, T. P. (2004): *Coal fires burning out of control around the world: Thermodynamic recipe for environmental catastrophe*. *Int. J. Coal Geology*, 59, 7 – 17.
- Sukop, M. C. and Thorne Jr., D. T. (2006): *Lattice Boltzmann Modeling - An Introduction for Geoscientists and Engineers*. Springer-Verlag, Heidelberg, Berlin.
- Tetzlaff, A. (2004): *Coal fire quantification using Aster, ETM and Bird satellite instrument data*. Ph.D. thesis, Ludwig Maximilians University Munich, Germany.

- Thomas, L. (2002): *Coal Geology*. John Wiley & Sons, LTD, Chichester.
- Thorenz, C. (2001): *Model Adaptive Simulation of Multiphase and Density Driven Flow in Fractured and Porous Media*. Ph.D. thesis, ISEB, University of Hannover, Germany.
- Tritton, D. J. (1970): *Physical Fluid Dynamics*. Oxford Science Publication, Oxford.
- Tsang, C.-F. and Doughty, C. (2003): *A particle-tracking approach to simulating transport in a complex fracture*. *Water Resources Research*, 39(7), TNN 1–1.
- VDI-Wärmeatlas (2002): *VDI-Wärmeatlas: Berechnungsblätter für den Wärmeübergang*. Springer-Verlag, Berlin, Heidelberg, 9th edition.
- Vogel, H. (1997): *Gerthsen Physik*. Springer-Verlag, Berlin, Heidelberg, New York, 19th edition.
- Vortmeyer, D. (1980): *Radiation in packed solids*. *Ger. Chem. Eng.*, 3, 124 – 138.
- Walter, A. L., Find, E. O., Blowes, D. W., Ptacek, C. J., and Molson, J. W. (1994): *Modeling of multicomponent reactive transport in groundwater 1. Model development and evaluation*. *Water Resources Research*, 30(11), 3137 – 3148.
- Ward, J. C. (1964): *Turbulent Flow in Porous Media*. In *Journal of the Hydraulics Division*, volume 90 of ASCE, p. 1 – 12.
- Wessling, S. and Kessels, W. (2005a): *Thermal Parameters for Dry Rocks with Respect to High Temperature Variations*. Unpublished project report as a contribution to the Sino-German Research Initiative "Innovative Technologies for Exploration, Extinction and Monitoring of Coal Fires in North China", archive no. 012 3542, GGA Institute, Hannover, Germany.
- Wessling, S. and Kessels, W. (2005b): *WP 3600 Dynamic Modelling: Investigation of the Influence of Hydraulic Parameter Variations*. Unpublished project report as a contribution to the Sino-German Research Initiative "Innovative Technologies for Exploration, Extinction and Monitoring of Coal Fires in North China", GGA Institute, Hannover, Germany.
- Wessling, S., Litschke, T., Wiegand, J., Schloemer, S., and Kessels, W. (2006): *Simulating Dynamic Subsurface Coal Fires and its Applications*. Accepted in *ERSEC Ecological Book Series - 4 on Coal Fire Research*. UNESCO, Beijing, PR China.
- Westbrook, C. K. and Dryer, F. L. (1981): *Simplified reaction mechanism of the oxidation of hydrocarbon fuels in flames*. *Combustion Science and Technology*, 27, 31 – 43.
- Whitaker, S. (1996): *The Forchheimer equation: a theoretical development*. *Transport in Porous Media*, 25, 27 – 61.
- Whitaker, S. (1999): *The Method of Volume Averaging*, volume 13 of *Theory and Applications of Transport in Porous Media*. Kluwer Academic Publishers, Dordrecht.

- Whitehouse, A. E. and Mulyana, A. A. S. (2004): *Coal fires in Indonesia*. *Int. J. Coal Geology*, 59, 91 – 97.
- Witherspoon, P. A., Amick, C. H., Gale, J. E., and Iwai, K. (1979): *Observations of a potential size effect in experimental determination of the hydraulic properties of fractures*. *Water Resources Research*, 15(5), 1142 – 1146.
- Witherspoon, P. A., Wang, J. S. Y., Iwai, K., and Gale, J. E. (1980): *Validity of cubic law for fluid flow in a deformable rock fracture*. *Water Resources Research*, 16(6), 1016 – 1024.
- Wright, D. E. (1968): *Nonlinear Flow Through Granular Media*. In *Journal of the Hydraulics Division*, volume 94 of ASCE, p. 851 – 872.
- Xu, T., Samper, J., Ayora, C., Manzano, M., and Custodio, E. (1999): *Modeling of non-isothermal multi-component reactive transport in field scale porous media flow systems*. *J. Hydrology*, 214, 144 – 164.
- Yang, L. (2004): *Study on the model experiment and numerical simulation for underground coal gasification*. *Fuel*, 83, 537 – 584.
- Yeh, G.-T. (2000): *Computational Subsurface Hydrology – Reactions, Transport, and Fate*. Kluwer Academic Publishers, Boston, Dordrecht, London.
- Young, T. R. and Boris, J. P. (1977): *A numerical technique for solving stiff ordinary differential equations associated with the chemical kinetics of reactive-flow problems*. *The Journal of Physical Chemistry*, 81(25).
- Zelkowsky, J. (1986): *Kohleverbrennung, Brennstoff, Physik und Theorie, Technik*. VGB-Kraftwerkstechnik GmbH, Essen.
- Zhang, D., Zhang, S., R. and Chen, and Soll, W. E. (2000): *Pore scale study of flow in porous media: Scale dependency, REV, and statistical REV*. *Geophysical Research Letter*, 27(8), 1195 – 1198.
- Zhang, J. (2004): *Spatial and Statistical Analysis of Thermal Satellite Imagery for Extraction of Coal Fire Related Anomalies*. Ph.D. thesis, Technical University of Vienna, Austria.
- Zhang, X., Kroonenberg, S. B., and Boer, C. B. d. (2004): *Dating of coal fires in north-west China*. *Terra Nove*, 16(2), 68 – 74.
- Zhou, J. G. (2004): *Lattice Boltzmann Methods for Shallow Water Flows*. Springer-Verlag, Berlin.
- Zou, Q. and He, X. (1997): *On pressure and velocity boundary conditions of the lattice Boltzmann BGK model*. *The Physics of Fluids*, 9(6), 1591 – 1598.
- Zysset, A., Stauffer, F., and Dracos, T. (1994): *Modeling of chemically reactive groundwater transport*. *Water Resources Research*, 30(7), 2217 – 2228.

Appendix

A	Estimations of Flow Magnitudes and the Relevance of Nonlinear Effects	138
B	Experimental Determination of Reaction Kinetic Parameters from Self-Heating Experiments	143
C	Pressure Considerations for Thermally Driven Systems	145

A Estimations of Flow Magnitudes and the Relevance of Nonlinear Effects

We here discuss the flow behavior within a macroscopic porous medium with respect to an estimation for underground coal fires.

The regime and proper description of fluid motions through discontinuous porous or fractured media obtained much attention by various researchers, including authors like Ward (1964); Wright (1968); Beavers and Sparrow (1969); Couland et al. (1988), and Ruth and Ma (1992) for experiments or numerical simulations, and Ergun (1952); Ahmed and Sunada (1969); Dullien and Azzam (1973); Mei and Auriault (1991), and Whitaker (1996) for theoretical considerations of flow phenomena in porous media. Fracture flow was investigated by Louis (1967); Witherspoon et al. (1979, 1980); Kohl et al. (1997), and Skjetne et al. (1999). The description of fluid motions is based on momentum conservation of the fluid, and becomes a difficult task when macroscopic scales are considered.

In common fluid mechanics where single-phase fluids are considered, the Navier-Stokes equations describes momentum conservation of the fluid. However, at least three reasons argue against the use of the Navier-Stokes equations in discontinuous media for the simulation of macroscopic flow phenomena:

1. Pores within a porous medium have small spatial scales, being as low as some millimeters for sandstones or even less. The grid size to resolve such scales needs to be sufficiently small, so that numerical simulations of phenomena on large scales become impractical. Especially, the simulation of turbulent flow regimes at larger flow rates would require a very fine grid resolution.
2. Solving the Navier-Stokes equations requires the formulation of appropriate boundary conditions for the bounds between voids and the solid matrix. This presumes the knowledge about the geometry of the discontinuous medium, at least approximately. Because this is also rarely known, the numerical treatment of the Navier-Stokes equations is inappropriate.
3. *In-situ* experiments (like well testing) observe macroscopic transport or flow phenomena on scales much larger than the scale of pores, thereby overlooking the explicit phenomena within the pores. Hence, at least for practical purposes, there is no need to know the flow behavior within single pores.

Due to these reasons a proper description of momentum conservation at large spatial scales turns out to be an empirical formulation, including macroscopic parameters. Knowledge about the order of magnitude of flow rates can be estimated for linear (Darcy) and non-

linear (Forchheimer) flow. Assuming isotropy, Darcy flow is described by (Eq. 2.20)

$$\mathbf{q} = -\frac{k}{\mu}(\nabla P - \rho^f \mathbf{g}). \quad (\text{A.1})$$

Herein, k is the permeability, μ is the fluid viscosity, \mathbf{g} is the gravitational acceleration, and ρ^f is the fluid density. Darcy's law expresses a linear relation between pressure gradients ∇P and the specific flow rate \mathbf{q} . This linear expression can be derived from the Navier-Stokes equation by neglecting inertia forces (see e.g. Whitaker, 1996). At higher flow rates, inertia forces cannot be neglected. In that case, the Forchheimer equation is frequently applied:

$$\nabla P - \rho^f \mathbf{g} = -\frac{\mu}{k} \mathbf{q} - \frac{c_F}{\sqrt{k}} \rho^f |\mathbf{q}| \mathbf{q}, \quad (\text{A.2})$$

where the form-drag coefficient c_F appears. The Forchheimer equation expresses a non-linear, quadratic relation between pressure gradients and the specific flow rate.

For both, the linear and the non-linear equation, the relation between the pressure gradient and the flow rate depends on the fluid viscosity and the permeability. The non-linear term in the Forchheimer equation also depends on the fluid density and on the form-drag coefficient. For gas, the fluid viscosity may vary by one order of magnitude with respect to temperature variations (see VDI-Wärmeatlas, 2002). The permeability is a macroscopic parameter, its magnitude is determined by the structure of the pores only (Nield and Bejan, 1999). k may vary by many orders of magnitude. E.g., clay exhibits permeabilities of about $10^{-18} m^2$, whereas the permeability of sandstones varies between $10^{-12} m^2$ and $10^{-16} m^2$ (Guéguen and Palciauskas, 1994). Coarse-grained gravels exhibit values around $10^{-7} m^2$ (Nield and Bejan, 1999).

Whereas the fluid viscosity can be taken from data collection books, the permeability of a macroscopic system is generally not known a-priori. k can be estimated from *in-situ* or laboratory experiments or be derived from theoretical estimations for simple pore structures. An estimation of the permeability of discontinuous beds around underground coal fires has not been addressed in previous studies. Hence, the permeability is an unknown macroscopic parameter, the magnitude of which may vary over several orders. Therefore, the relevance of non-linear effects is not known a-priori.

The relevance of non-linear effects for the flow behavior in underground coal fire systems is here discussed with respect to permeability variations. The estimation is based on the analytical solution of the one-dimensional Forchheimer equation. For the one-dimensional case (without thermal buoyancy), e.g. in x-direction ($q_x := q$), Eq. A.2 becomes

$$\frac{\Delta P}{\Delta x} + \frac{\mu}{k} q + \frac{c_F}{\sqrt{k}} \rho^f q^2 = 0, \quad (\text{A.3})$$

which yields, after re-arrangement,

$$q = -\frac{\mu}{2\sqrt{k}c_F\rho^f} \pm \sqrt{\left(\frac{1}{4k} \frac{\mu}{c_F\rho^f}\right)^2 - \frac{\sqrt{k}}{c_F\rho^f} \frac{\Delta P}{\Delta x}}. \quad (\text{A.4})$$

The last term in the root, $(\sqrt{k}/c_F\rho^f)(\Delta P/\Delta x)$, might cause problems due to its negative sign. If that term becomes larger than the first term, negative arguments arise. However, assuming $q > 0$ without loss of generality, $(\sqrt{k}/c_F\rho^f)(\Delta P/\Delta x) < 0$ holds, because pressure gradients are negative for $q > 0$, by convention for common fluid dynamics considerations. Thus, the analytical one-dimensional solution of Eq. 3.17 is given as

$$q = -\frac{\mu}{2\sqrt{k}c_F\rho^f} \pm \sqrt{\left(\frac{1}{4k} \frac{\mu}{c_F\rho^f}\right)^2 + \frac{\sqrt{k}}{c_F\rho^f} \left|\frac{\Delta P}{\Delta x}\right|}. \quad (\text{A.5})$$

A parameter affecting the strength of non-linear effects is the form-drag coefficient, q . Whereas early investigators assumed c_F to be a constant with an approximate value of $c_F = 0.55$, it was later found that c_F varies with the nature of the porous medium (Nield and Bejan, 1999). Beavers et al. (1973) showed that the bounding walls could have a substantial effect on the value of c_F , and found that their data correlated fairly well with the expression

$$c_F = 0.55 \left(1 - 5.5 \frac{d}{D_e}\right), \quad (\text{A.6})$$

where d is the diameter of particles in a porous medium and D_e is the equivalent diameter of the bed, defined in terms of the height h and width w of the bed by

$$D_e = \frac{2wh}{w+h}. \quad (\text{A.7})$$

Numerical calculations of Couland et al. (1988) on flow through circular cylinders suggest that c_F varies as the inverse porosity, Φ^{-1} for Φ less than 0.61.

An estimation of the order of magnitude of q is given in Figures A.1 and A.2 for the range of pressure differences arising due to thermal buoyancy (see e.g. Schmal, 1987). The fluid density and viscosity are $\rho^f = 1.29 \text{ kg m}^{-3}$ and $1.81 \times 10^{-5} \text{ Pa s}^{-1}$, respectively. Concluding from the estimations, nonlinear effects become important at permeability values $k \geq 10^{-8} \text{ m}^2$, although the nonlinearity remains weak for $k = 10^{-8} \text{ m}^2$. Discrepancies to the linear Darcy flow are only visible at large pressure gradients. Likewise, the small discrepancies are obtained for variations of the form-drag coefficient, when the permeability is smaller or equal 10^{-8} m^2 . For $k < 10^{-7} \text{ m}^2$, the form-drag coefficient has significant influence on the nonlinear flow behavior.

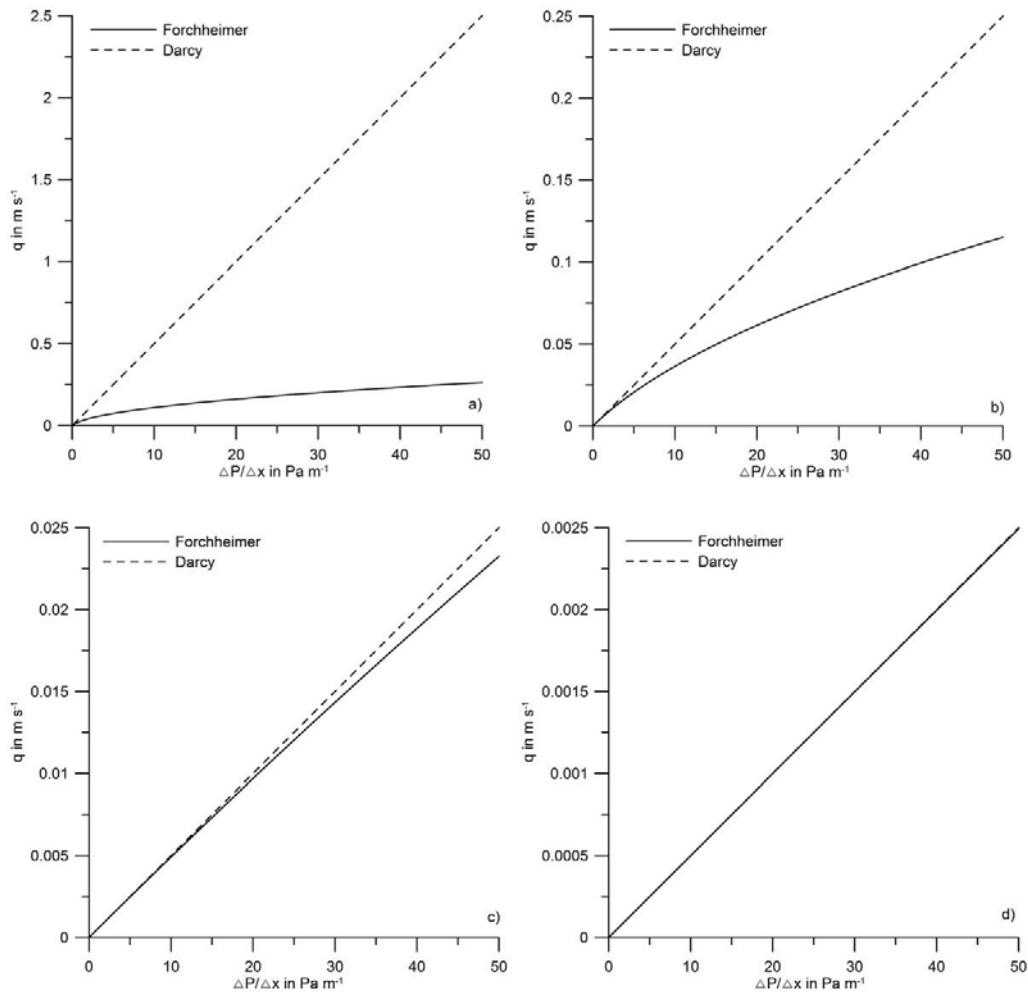


Figure A.1 Specific flow rate, q , versus pressure differences, $\Delta P/\Delta x$, for $c_F = 0.5$ and permeability values a) $k = 10^{-6} \text{ m}^2$; b) $k = 10^{-7} \text{ m}^2$; c) $k = 10^{-8} \text{ m}^2$; d) $k = 10^{-9} \text{ m}^2$, assuming linear Darcy flow (Eq. A.1) and non-linear Forchheimer flow (Eq. A.2), respectively.

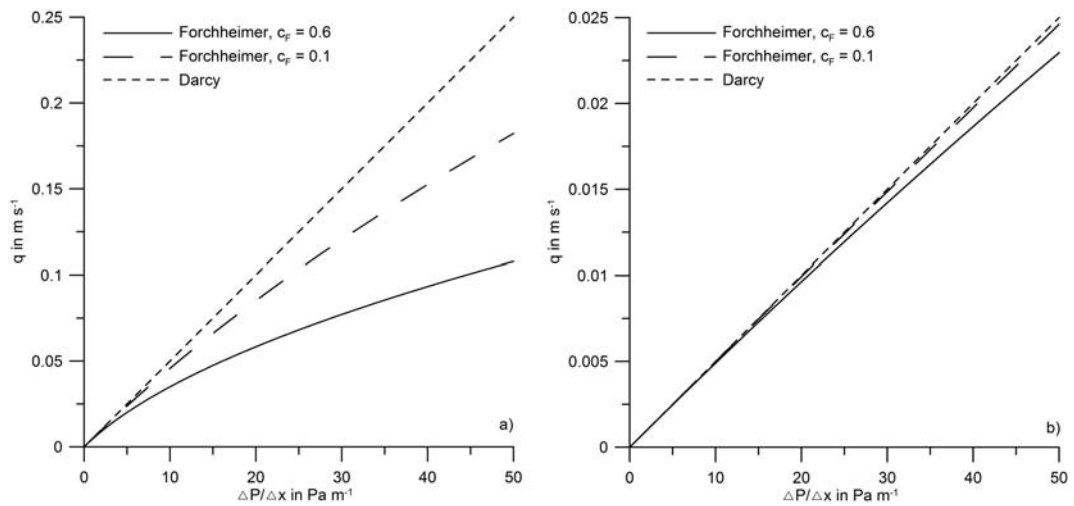


Figure A.2 Specific flow rate, q , for different form-drag constants, c_F , and for permeabilities a) $k = 10^{-7} \text{ m}^2$ and b) $k = 10^{-8} \text{ m}^2$, respectively.

B Experimental Determination of Reaction Kinetic Parameters from Self-Heating Experiments

A frequently used expression for the description of reaction kinetics is the Arrhenius formulation, which has been introduced in Sec. 2.2.2. Herein, two reaction kinetic parameters are involved: the pre-exponential factor k_0 , and the activation energy E . I here briefly describe how these parameters can be obtained experimentally.

Several self-heating methods to determine E of thermally unstable materials are described in Malow and Krause (2004). One such method is the Frank-Kamenetzki (F-K) analysis, which has been used to obtain the reaction kinetic parameters from Tab. 2.2. The self-ignition temperature (SIT) of the material is determined experimentally by so-called hot storage tests. The sample is filled in equidistant wire-mesh cylinders and placed in a pre-heated oven. A sufficient number of hot storage tests - with a fresh sample for each test - are performed to determine the highest oven temperature at which ignition does not occur. The difference of oven temperatures between tests with and without ignition is at most 4 K. At least the SIT of four volumes have to be determined. The experimental set-up is described in detail in Krause and Schmidt (2001).

Experimental results are obtained from analysis of the self-heating coal in thermal equilibrium. Thermal equilibrium in a dust deposit can be described by a second-order differential equation (Hattwick and Steen, 2004),

$$\frac{\partial^2 \Theta}{\partial z^2} + \frac{n}{z} \frac{\partial \Theta}{\partial z} = -\delta e^\Theta, \quad (\text{B.1})$$

where z is a normalized or reduced length and n is a geometry factor (0 for an infinite slab, 1 for an infinite cylinder, 2 for a sphere). Θ is a dimensionless temperature:

$$\Theta = \frac{E}{R} \frac{(T - T_a)}{T_a^2}, \quad (\text{B.2})$$

where T_a is the ambient temperature. The Frank-Kamenetzki parameter δ includes all characteristics of the geometry of the reactive system and is defined by

$$\delta = \frac{E r^2 \rho Q}{\lambda R T_a} k_0 e^{-\frac{E}{R T_a}}, \quad (\text{B.3})$$

where r is the characteristic length of the sample, ρ the bulk density, Q the heat of reaction per unit mass and k_0 is the pre-exponential factor of the Boltzmann term (e^{-E/RT_a}).

Solutions of equation B.1 were developed by Frank-Kamenetzki for simple geometries. A maximum value of δ , which still satisfies the conditions of equilibrium, characterizes the transition from steady state (no ignition) to transient behavior (ignition), depending on the

geometry. The maximum value of δ (where just no ignition occurs) is called critical F-K parameter δ_c . For Biot number (Bi) $\rightarrow \infty$ (temperature of the edge of the deposit is equal to the ambient temperature) values of δ_c are listed in Tab. B.1. Rearranging equation B.3 leads to the linear equation

$$\ln\left(\delta \frac{T_a^2}{r^2}\right) = \ln\left(\frac{EQ\rho k_0}{R\lambda} - \frac{E}{R} \frac{1}{T_a}\right). \quad (\text{B.4})$$

If δ_c is inserted for δ the ambient temperature T_a is equal to the self-ignition temperature (SIT). The activation energy E and the pre-exponential factor k_0 are obtained from a linear plot of $\ln(\delta_c \text{SIT}^2 / r^2)$ vs. SIT^{-1} .

If small dust samples are investigated (laboratory scale) the surface temperature depends on the inner temperature of the sample and differs from the ambient temperature. In this case the critical F-K parameter depends on the Biot number and the so-called Thomas model has to be applied (see Hattwick and Steen, 2004).

Geometry of bulk deposit	δ_c for $Bi \rightarrow \infty$
Sphere	3.32
Equidistant cylinder	2.76
Cube	2.52
Infinite cylinder	2.0
Infinite slab	0.88

Table B.1 Critical F-K parameters δ_c for different shapes of bulk deposits. Bi = Biot number.

C Pressure Considerations for Thermally Driven Systems

Various simulation results are presented in the literature concerning thermally driven flow systems, for single-phase fluids (see e.g. Breuer et al., 2004) or for porous media (Dirsch, 1998; Holzbecher, 1998; Kolditz et al., 1998; Schoofs, 1999). An investigation of the pressure distribution developing in thermally driven systems obtained little attention in previous studies. Especially, when the absolute pressure is considered in the model, the pressure differences giving rise to thermal convection are difficult to extract from the absolute pressure field, due to its composition of a dynamic and a hydrostatic part.

This appendix discusses a though experiment, based on the schematic illustration in Fig. C.1. The figure shows an u tube which is filled with incompressible fluid. The fluids in the vertical tubes are assumed to exhibit different temperatures. The vertical tubes exhibit hydraulic resistances R_v^h and R_v^c for fluid motions. If these tubes are not filled with porous material, the hydraulic resistances are very small, but exist due to the friction at the tube walls. The vertical tubes are also connected by a horizontal tube that represents a hydraulic resistance R_h for the fluid. For simplicity, the pressure is assumed to be kept constant at a value of P_0 at the top of the vertical tubes. Such a situation is given for flow systems that are connected to the atmosphere.

First, assume the hydraulic resistance R_h to be infinite, hence the fluid does not flow. Due to the different temperatures of the fluids in the vertical tubes, the hydraulic pressure distributions are observed as P_{hyd}^s for the cold (right) tube and P_{abs}^s for the hot (left) tube (the dashed colored lines). The slope of P_{abs}^s is less steep than the slope of P_{hyd}^s , because the fluid in the cold tube is denser than the fluid in the hot tube. Consequently, a horizontal pressure difference, ΔP_h^s , exists between the two vertical tubes.

If the hydraulic resistance R_h is decreased to a finite value, fluid flow sets in due to the pressure difference along the horizontal tube, which in turn is a result of different hydrostatic pressure distributions in the vertical tubes. Due to the fluid motions, the pressure distribution within the vertical columns changes from P_{abs}^s and P_{hyd}^s to P_{abs} and P_{hyd} (from the dashed lines to the solid lines). The driving pressure difference for the fluid motions through the u tube is ΔP_h , which is lower than the horizontal pressure difference at stagnation state, ΔP_h^s . The value of ΔP_h depends on the hydraulic resistances of the tubes. If only the horizontal tube is filled with porous material, ΔP_h depends primarily on R_h , the hydraulic resistance of the horizontal tube. A high resistance produces a high value of ΔP_h . In contrast, if all tubes are assumed to be not filled with permeable material, ΔP_h will become very small and only depends on the friction resistance of the tubes.

In Sec. 6.3.1, ΔP_h has been calculated from the simulated absolute pressure distribution by subtracting the hydrostatic pressure for the cold gas from the simulated absolute pressure. As illustrated in Fig. C.1, ΔP_h increases with decreasing Δz . According to this

pressure distribution, one might think that fluid flow would take place downwards in the left (hot) tube. However, the opposite is the case, i.e. fluid flow takes place upwards.

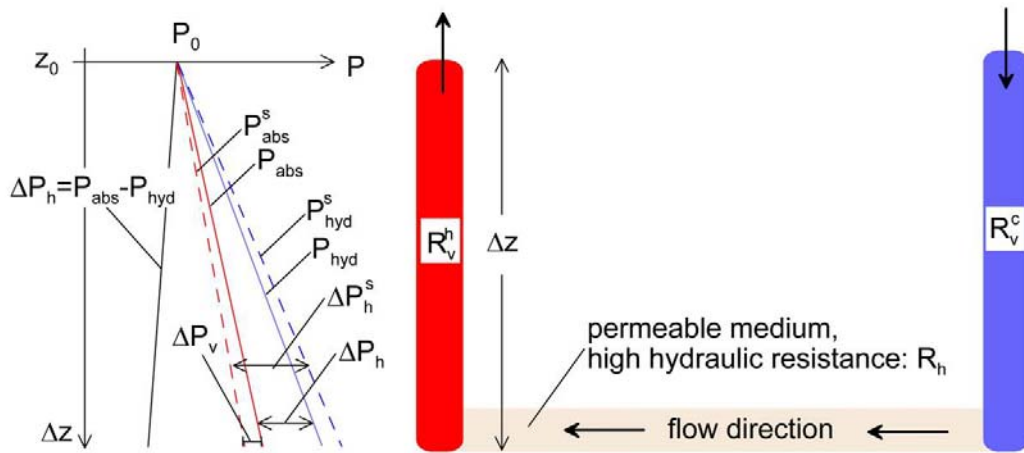


Figure C.1 Schematic illustration of the pressure distribution due to thermal buoyancy (see the description of variables below)

Description of variables included in Fig. C.1:

P_0 Reference pressure at z_0

P_{hyd}^s Hydrostatic pressure at stagnation state

P_{abs}^s Absolute pressure of the hot tube at stagnation state

P_{hyd} Hydrostatic pressure when fluid flows

P_{abs}^s Absolute pressure of the hot tube when fluid flows

ΔP_v Dynamic pressure difference as observed in the left (hot) tube

ΔP_h^s Dynamic pressure difference at stagnation state in the horizontal, cause by pressure differences between the left and the right tube

ΔP_h Dynamic pressure difference in the horizontal, cause by pressure differences between the left and the right tube

R_v^h Hydraulic resistance in the vertical tube filled with hot fluid

R_v^c Hydraulic resistance in the vertical tube filled with cold fluid

R_h Hydraulic resistance in the horizontal tube

Symbols

Symbol	Unit	Description
c^b	$J m^{-3} K^{-1}$	Bulk heat capacity
c_{bulk}	$kg m^{-3}$	Bulk concentration
c_F	—	Form-drag constant
c_{fl}	$kg m^{-3}$	Fluid concentration
c_j	$kg m^{-3}$	Concentration of chemical species j ($j = f, O_2, eg, sp$)
$c_{j,0}$	$kg m^{-3}$	Initial concentration of chemical species j ($j = f, O_2, eg, sp$)
c_m	$kg m^{-3}$	Mineral concentration
c_p^f	$J kg^{-1} K^{-1}$	Specific heat capacity of fluid
D	$m^2 s^{-1}$	Dispersion tensor
D_{mol}	$m^2 s^{-1}$	Molecular diffusion coefficient
E	$J mol^{-1}$	Activation energy
g	$m s^{-2}$	Gravitational acceleration
ΔH	$J kg^{-1}$	Calorific value
j_c	$J m^{-2} s^{-1}$	Convective heat flux
j_F	$J m^{-2} s^{-1}$	Conductive heat flux
j_h	$J m^{-2} s^{-1}$	Overall heat flux
j_m	$kg m^{-2} s^{-1}$	Fluid mass flux
j_r	$J m^{-2} s^{-1}$	Radiative heat flux
k	m^2	Permeability
k_{ij}	m^2	Permeability tensor
k_0	$m^3 kg^{-1} s^{-1}$	Pre-exponential factor
ℓ	m	Representative Length of oxygen drop
M_{air}	$g mol^{-1}$	Molar mass of air
M_j	$g mol^{-1}$	Molar mass of component j
n	mol	Mole number

P	Pa	Pressure
P_{abs}	Pa	Absolute pressure
P_{dyn}	Pa	Dynamic pressure
P_{hyd}	Pa	Hydrostatic pressure
P_0	Pa	Reference pressure
Q_H	$J m^{-3} s^{-1}$	Source term for heat production
Q_j	$kg m^{-3} s^{-1}$	Source term for chemical species ($j = f, O_2, eg, sp$)
Q_m	$kg m^{-3} s^{-1}$	Fluid mass source term
Q_V	$m^3 s^{-1}$	Fluid volume source term
\mathbf{q}	ms^{-1}	Specific flow rate
R	$J mol^{-1} K^{-1}$	Unified gas constant
r_h	$kg m^{-2} s^{-2}$	Hydraulic resistivity
S	Pa^{-1}	Storativity
T	K	Temperature
T_{max}	K	Maximum combustion temperature
T_0	K	Reference temperature
t	s	Time
Δt_{tr}	s	Time step for oxygen transport
Δt_{ch}	s	Time step for chemical reaction
Δt_f	s	Time step for fuel consumption
V	m^3	Volume
\mathbf{v}	ms^{-1}	Interstitial fluid velocity
v_{pr}	ma^{-1}	Propagation rate of underground coal fire
α_l, α_t	m	Longitudinal, transversal dispersion lengths
β	$W m^{-1} K^{-4}$	Constant for radiant heat transport
λ_{eff}	$W m^{-1} K^{-1}$	Effective thermal conductivity
λ_r	$W m^{-1} K^{-1}$	Radiative thermal conductivity
λ_0	$W m^{-1} K^{-1}$	Thermal conductivity at room temperature
μ	$Pa s$	Fluid viscosity
ν_j	–	Stoichiometric coefficient for component j
Φ	–	Porosity
ρ^f	$kg m^{-3}$	Fluid density

ρ_0^f	$kg\,m^{-3}$	Reference fluid density
τ_j^r	s	Time scale for reaction kinetics (component j)
$\tau_{O_2}^t$	s	Time scale for oxygen transport
τ_{th}	s	Thermal relaxation time

List of Figures

2.1	Simplified schematic illustration of phenomena appearing in underground coal fires	9
2.2	Illustration of the definition of a representative elementary volume	12
2.3	Representation of assumed physico-chemical processes and the coupling mechanisms between them	16
2.4	Density variations with respect to temperature and pressure changes within a range $\Delta T = 900 K$ and $\Delta P = 2000 Pa = 20 mbar$	22
2.5	Temperature dependent thermal conductivity $\lambda_{eff}(T) = \lambda_0 + \beta(T - T_0)^3$	28
2.6	Schematic illustration of a macroscopic combustion front	30
2.7	Illustration of the temperature dependent time scales, τ^c for oxygen consumption and τ^t for oxygen transport	34
3.1	Illustration of the operator-splitting approach for two temperature values	39
3.2	Temporal development of the time step size, Δt_r	40
3.3	Maximum and average difference in oxygen concentration	43
3.4	Comparison between analytic and numerical solution of the Forchheimer equation	47
3.5	Comparison of the temperature development and the coal consumption between analytic and numerical solutions	48
3.6	Verification of the mass balance including thermal buoyancy	50
3.7	Comparison of the pressure drop between Rockflow and COMSOL Multiphysics simulations without thermal buoyancy	51
3.8	Setup for example simulations	52
3.9	Distribution of the exhaust gas and the oxygen concentration after 242 days of simulation time	54
3.10	Temperature distribution due to the underground coal fire at three different times	55
3.11	Dynamic development of the maximum combustion temperature	56
3.12	Distribution of the specific flow rate after a simulation time of 591 days	56
3.13	Temperature distribution and energy flux after a simulation time of 585 days	58
3.14	Cumulative energy release, coal consumption and energy flux through the surface	59
3.15	Illustration for the definition of the propagation rate	60
4.1	Development of the maximum temperature for different permeabilities	64
4.2	Temporal development of the maximum temperature with respect to variations of λ_0 for coal and rock	65

4.3	Temperature dependent thermal conductivities for different values of β . . .	66
4.4	Temperature distribution and distribution of coal after 484 days obtained for different effective thermal conductivities	67
4.5	Temporal development of the maximum temperature for different temperature dependent thermal conductivities and permeabilities	67
4.6	Temporal development of the maximum combustion temperature for different Representative Lengths	68
4.7	Fire propagation rate in dependence of the effective thermal conductivity and the permeability	70
5.1	Pressure and ambient temperature variations used as boundary conditions for the simulation to investigate external natural influences	75
5.2	Time dependent modified storativity S' in Pa^{-1} as a function of monitored barometric pressure variations	77
5.3	Temperature and observation points for the system response investigations .	79
5.4	Concentration of oxygen and observation points for the system response investigations	79
5.5	Response at observation point 1 of the absolute value of the specific flow rate to Dirichlét boundary conditions for the pressure as a function with constant positive slope	80
5.6	Pressure response at observation points 1 and 2 to the externally imposed pressure variations at the boundary	81
5.7	Illustration of the varying distribution of the oxygen concentration with time	81
5.8	Response of temperature, oxygen concentration and pressure to atmospheric pressure variations at different observation points	83
5.9	Setup for the investigation of wind blowing against the outcrop	84
5.10	Distribution of the oxygen concentration, without and with wind-induced pressure rise at the outcrop	85
6.1	General stratigraphy of the Wuda coal mining area	88
6.2	Location of coal fires in Fire Zone 3.2 (Wuda)	89
6.3	Mapped thermally active and inactive crack systems in Fire Zone 3.2	91
6.4	Illustration of pressure measurements	94
6.5	Measured pressure differences between the atmosphere and the dynamic pressure prevailing approximately 20 meters below the surface	95
6.6	Environment for the installation of the temperature sensors in Fire Zone 3.2	96
6.7	Monitored temperatures in the opening and in the covered location	97
6.8	Spatial distribution of the near-surface temperature in Fire Zone 3.2	98
6.9	Observations of CO/CO_2 ratios in Fire Zone 3.2	100
6.10	Observation of oxygen concentrations above burning coal seam no. 10 in Fire Zone 3.2	100
6.11	Temperature distribution and specific flow rate after 246 days of simulation time	103
6.12	Distribution of the dynamic pressure after 246 and 585 days	105

6.13	Simulation of the changes in oxygen concentration from 246 to 586 days . .	106
7.1	Comparison of the temperature and the coal distribution after surface coverage	110
7.2	Extinction activities performed in Fire Zone 3.2 of the Wuda coal mining area	111
7.3	Setup for the simulation of a water injection scenario	113
7.4	Simulation results after 40 hours of water injection into the heated system from Fig. 7.3	115
7.5	Temperature distribution 30 days after the end of water injection into and in front of the downward combustion center	116
A.1	Specific flow rate versus pressure differences for $c_F = 0.5$ and different permeability values	141
A.2	Specific flow rate for different form-drag constants and permeabilities . . .	142
C.1	Schematic illustration of the pressure distribution due to thermal buoyancy .	146

List of Tables

2.1	Stoichiometric coefficients and calorific value	20
2.2	Reaction kinetic parameters after as obtained from the F-K Analysis method for samples from Wuda coal	27
3.1	Sequence of solving the non-linear set of equations	36
3.2	Sequence of solving the set of equations over the time steps $t^i \rightarrow t^i + \Delta t_{tr} +$ $\Delta t_f \rightarrow t^{i+1}$	42
3.3	Simulation results to investigate the difference in maximum temperature . .	43
3.4	Results for the investigation of the Newton-Raphson algorithm	46
3.5	Thermal and hydraulic parameters for the example simulation	53
3.6	Total energy flux integrated along the profiles as presented in Fig. 3.13 . . .	58
3.7	Fire propagation rates without distinction between up- and downward mov- ing fires	61
3.8	Fire propagation rates with distinction between the up- and downward mov- ing fires	61
4.1	Fire propagation rates for varying Representative Lengths	68
4.2	Range of specific flow rates for different permeabilities	71
6.1	Results of ventilation measurements	93
6.2	Comparison between simulated flow rates and ventilation measurements . .	104
7.1	Parameters for the simulation of the water injection scenario	114
7.2	Water-specific parameters for the simulation of the injection scenario	114
B.1	Critical F-K parameters for different shapes of bulk deposits	144

Acknowledgements

This thesis has been performed in the context of the Sino-German Research Initiative "Innovative Technologies for Exploration, Extinction and Monitoring of Coal Fires in North China". That project lasted for the time period May 2003 until June 2006. During these years, the project offered me the possibility to visit the People's Republic of China. I could perform measurements on coal fire test sites and, also, get to know and enjoy the Chinese mentality.

I acknowledge financial support by the Federal Ministry of Education and Research (BMBF, Berlin), grant no. 0330490B, which enabled me to do research on coal fires. Especially, I thank Dr. Fitting (PT Jülich) for supporting the project.

I also gratefully thank Prof. Dr. U. Hansen (University of Münster) and Prof. Dr. H.-J. Kümpel (GGA Institute, Hannover) for the revision of the thesis, as well as helpful suggestions during its realization.

Likewise, I am grateful to Dr. W. Kessels (GGA Institute, Hannover), who initiated the project part for the GGA Institute, employed me and finally guided me to successfully work on coal fire simulation. His supervising activities were performed with much engagement. Many ideas and fruitful discussions helped me to permanently improve the thesis' progress.

The Research Initiative has been managed and coordinated by Dr. S. Voigt (DLR/DFD, Wessling) and Prof. Dr. H. Rüter (Harbourdom, Dortmund), for which I would also like to deeply pronounce my thanks.

I also sincerely thank Dr. M. Breuer (University of Münster), W. Rühaak (GGA Institute, Hannover), Dr. S. Schlömer (BGR, Hannover), Dr. K. Schwalenberg (BGR, Hannover) and Dr. M. W. Wuttke (GGA Institute, Hannover) to correct the thesis and for being up for discussions concerning scientific problems.

For experimental support, especially concerning reaction kinetic issues, I'd like to thank Dr. U. Krause, Dr. C. Lohrer and Dr. M. Schmidt (BAM, Berlin). Without their investigations, my numerical simulations could not be realized.

Other data which I could use during the study were offered by Dr. H. Gielisch (DMT, Essen), T. Litschke (University of Essen-Duisburg), Dr. S. Schlömer (BGR), for which I deeply thank.

Of course, coal fire research to this extent would not be possible without cooperative work between participating project partners. I am thus, among others, grateful to Dr. F. Bandelow (DMT, Essen), Prof. Dr. C. Buhrow (TU-Bergakademie Freiberg), Dr. C. Künzer (Technical University of Vienna), Dr. U. Meyer (BGR, Hannover), and Dr. G. Schaumann (BGR, Hannover)

In-situ investigations could not be realized without support by our Chinese colleagues, so that I also thank Y. Jia (Shenhua Group Coal Mining Company), K. Bing (Beijing Normal University), and Prof. L. Gudong (BOST, Beijing), and all other partners from China whose names I could not keep in mind.

Finally, my very special thanks to my parents and family, especially my wife Anna and my children Jonas and Julia for the great time outside the GGA Institute.

Curriculum Vitae

Name: Stefan Wessling
 Date of Birth: June 15th, 1976
 Place of Birth: Thuine, Germany
 Marital Status: Married, two children
 Nationality: German

Professional Record

since 11/2005 Research assistant at GGA Institute, Hannover, Germany. Employed for innovative initiatives to improve geothermal energy production.
 Activities: Simulation of hydro-mechanical processes in geothermal reservoirs, software development, interpretation of hydraulic test data

05/2003–11/2005 Research assistant at GGA Institute. Contribution to the Sino-German Research Initiative "Innovative Technologies for Exploration, Extinction and Monitoring of Coal Fires in North China".
 Activities: Hydraulic-chemical-thermal process simulation of underground coal fires, *in-situ* gas flow and temperature measurements in coal fire test sites (China)

01/2003–03/2003 Internship at Co. Preussag GmbH, Lingen, Germany.
 Activities: Processing and interpretation of seismic data

10/2000–12/2002 Undergraduate research assistant at the Institute for Geoinformatics, Westfälische Wilhelms- University of Münster, Germany. Participation to projects:
 "Semantic Interoperability of Geoservices"
 "3D-Interaction Techniques for Geoscientific Applications"

Education

since 01/2003 Ph.D. student at Westfälische Wilhelms- University of Münster

12/2002 Diploma (M.Sc.) in Geophysics at Westfälische Wilhelms- University of Münster. Topic:
 "Numerical Study about the Dependence of the Prandtl Number on the Dynamics of Thermally Driven Flows"

10/1997–12/2002 Studies in Geophysics at Westfälische Wilhelms- University of Münster
 Subsidiary subjects: Geology, Geoinformatics, Science of Metals and Alloys

1989–1996 Secondary School "Gymnasium Johanneum", Lingen. "Abitur" in 1996

